Dissertation

submitted to the

Combined Faculties for the Natural Sciences and for Mathematics
of the Ruperto-Carola University of Heidelberg, Germany

for the degree of

Doctor of Natural Sciences

Put forward by

Anja Butter

born in Mayen, Germany

Oral examination: November 02, 2017

Global Fits for New Physics at the LHC and Beyond

Referees: Prof. Dr. Tilman Plehn
Prof. Dr. Björn Malte Schäfer

Abstract in deutscher Übersetzung

Physik jenseits des Standardmodells kann durch verschiedene Ansätze untersucht werden, die von UV-vollständigen Modellen wie Supersymmetrie bis hin zu den allgemeineren effektiven Feldtheorien (EFT) reichen.

Der von Fermi–LAT gemessene Exzess von γ–Strahlen aus dem galaktischen Zentrum (GC) kann als ein Signal dunkler Materie im minimalen supersymmetrischen Modell (MSSM) interpretiert werden. Mit SFitter identifizieren wir verschiedene Annihilationskanäle mit einer Dunkle–Materie–Masse von bis zu 300 GeV, die das gemessene Spektrum reproduzieren. Unter Berücksichtigung der vollständigen Abschätzung für statistische, systematische und theoretische Unsicherheiten durch Fermi–LAT finden wir nur eine milde Spannung zwischen der notwendigen Annihilationsrate und der beobachteten Dichte dunkler Materie. Starke Einschränkungen aus direkten Detektionsexperimenten und der beobachteten Dichte dunkler Materie schließen große Bereiche des Parameterraums aus und favorisieren einen pseudoskalaren Mediator. Die Erweiterung des MSSM um ein zusätzliches Singlet ermöglicht eine effiziente Annihilation von Dunkle–Materie–Teilchen unter 60 GeV über einen leichten Pseudoskalar. Wir können die resultierenden Lösungen für den GC-Exzess mit einem großen Higgs-Verzweigungsverhältnis in unsichtbare Endzustände verbinden, die in Reichweite von LHC Messungen liegen.

Schließlich nutzen wir das EFT-Framework, um höherdimensionale Operatoren vom Higgs- und dem elektroschwachen Sektor zu beschränken. Unsere Grenzen auf Kopplungen von drei Eichbosonen aus LHC Di–Boson–Kanälen sind um ein Vielfaches stärker als all diejenigen, die aus LEP–Daten bestimmt wurde. Die Kombination von Higgs-Messungen und Eichboson–Vertizes führt zu einer deutlichen Verbesserung der Limits auf die gesamten Operatoren.

Abstract

We study physics beyond the Standard Model with state–of–the–art global fits of both UV-complete models like supersymmetry and the more general effective field theories (EFTs).

The γ-ray excess from the galactic center measured by Fermi–LAT can be interpreted as a dark matter signature in the minimal supersymmetric model. Using the SFitter framework we identify different annihilation channels with a dark matter mass up to 300 GeV yielding the measured spectrum. Strong constraints from direct detection experiments and relic density rule out large regions of the parameter space, favoring a pseudoscalar mediator. In the next–to–minimal supersymmetric model the additional singlet allows efficient annihilation of dark matter particles below 60 GeV via a light pseudoscalar. We connect the resulting solutions to the GC excess with a large invisible Higgs branching ratio in reach of the LHC.

Finally we use the EFT framework to constrain higher-dimensional operators from the Higgs and the electroweak gauge sector. Our bounds on triple gauge–boson couplings from LHC di–boson channels are several times stronger than those obtained from LEP data. The combination of Higgs measurements and triple gauge vertices leads to a significant improvement in the entire set of operators.

Contents

Preface

This thesis is based on research conducted between 2014 and 2017 at the Institute for Theoretical Physics at Heidelberg University. The presented results were achieved in collaboration with other researchers and have been published as:

[1] A. Butter, S. Murgia, T. Plehn and T. M. P. Tait:
Harmonizing the MSSM with the Galactic Center Excess.
Phys. Rev. D96, p. 035036, 2017. arXiv:1612.07115.

[2] A. Butter, T. Plehn, M. Rauch, D. Zerwas, S. Henrot-Versillé and R. Lafaye:
Invisible Higgs Decays to Hooperons in the NMSSM.
Phys. Rev. D93, p. 015011, 2016. arXiv:1507.02288.

[3] A. Butter, O. J. P. Éboli, J. Gonzalez-Fraile, M. C. Gonzalez-Garcia, T. Plehn and M. Rauch:
The Gauge-Higgs Legacy of the LHC Run I.
JHEP 1607, p. 152, 2016. arXiv:1604.03105.

Chapter 2 and Chapter 3 are partially based on the three-part lecture the author gave within the framework of the research training group:

[4] A. Butter:
Fitting Dark Matter.
Student lecture, research training group 'Particle Physics Beyond the Standard Model'.

During her PhD studies the author also contributed to the following publications that are not incorporated in this thesis:

[5] M. Bauer, A. Butter, J. Gonzalez-Fraile, T. Plehn and M. Rauch:
Learning from a Higgs-like scalar resonance
Phys. Rev. D95 (5), p. 055011, 2017. arXiv:1607.04562.

[6] M. Bauer, A. Butter, N. Desai, J. Gonzalez-Fraile and T. Plehn:
Validity of dark matter effective theory
Phys. Rev. D95 (7), p. 075036, 2017. arXiv:1611.09908.

[7] A. Butter, G. Kasieczka, T. Plehn and M. Russell:
Deep-learned Top Tagging using Lorentz Invariance and Nothing Else
arXiv:1707.08966.

Finally, the author is involved in ongoing projects that have not been ready for publication at the time of writing this thesis.

Chapter 1

Moving beyond the Standard Model

Since the formulation of the electroweak theory by Sheldon Lee Glashow [8], Abdus Salam [9] and Steven Weinberg [10] in 1961 and 1967, the Standard Model of particle physics (SM) has been an amazing story of success. The discovery of the Higgs boson [11–13] in 2012 at the Large Hadron Collider (LHC) by ATLAS [14] and CMS [15] confirmed the mechanism of electroweak symmetry breaking and provided particle physics with a rather complete model in agreement with nearly all observations at modern colliders.

In the following we introduce the basic concepts of the SM and the challenges, that motivate theorists and experimentalists alike to search for answers beyond the SM. Searches for new physics cover a wide range of experiments and concepts. The work presented in this thesis has been carried out in two distinct areas of BSM physics: Supersymmetry and effective field theory.

In the framework of supersymmetry we examine solutions to the dark matter problem related to the potential dark–matter signals from the galactic center (GC) excess, a γ–ray excess in the few GeV range observed by Fermi–LAT [16]. Using global fits we give an answer to the question of how solutions to the GC excess can be linked to LHC analyses of the Higgs sector.

In the second part of this thesis we use the largely model–independent EFT framework to analyze di–boson channels and set limits on the operators contributing to triple gauge vertices (TGVs). The driving questions are how a combination of the latest LHC analyses of TGVs performs in comparison to previous LEP results and to quantify the additional constraining power obtained from a combined Higgs–Gauge fit.

While all presented projects are linked on the technical site via SFitter [17–19], a complex multipurpose fitting program described in Chapter 2, they belong to two very different approaches with individual aims and challenges. We will motivate the use of SUSY and EFT and highlight their respective features.

The Standard Model is a quantum field theory that is based on the action, the space-time integral over a Lagrangian $\mathcal{L}_{SM}$, that is invariant under global proper orthochronous Poincaré transformations (translations, rotations, and boosts) and the local $SU(3)_C \times SU(2)_L \times U(1)_Y$

gauge group,

$$S = \int d^4x \, \mathcal{L}_{SM} \ . \tag{1.1}$$

The SM Lagrangian is

$$\begin{aligned}\mathcal{L}_{SM} = &-\frac{1}{4} G^a_{\mu\nu} G^{a\,\mu\nu} - \frac{1}{4} W^a_{\mu\nu} W^{a\,\mu\nu} - \frac{1}{4} B_{\mu\nu} B^{\mu\nu} + \sum_f i \bar{f} \not{D} f \\ &+ (D_\mu \phi)^\dagger (D^\mu \phi) - \mu^2 \phi^\dagger \phi - \lambda (\phi^\dagger \phi)^2 \\ &- \sum_{\text{generations}} \left(y_u \begin{pmatrix} \bar{u} \\ \bar{d} \end{pmatrix}_L \tilde{\phi}\, u_R + y_d \begin{pmatrix} \bar{u} \\ \bar{d} \end{pmatrix}_L \phi\, d_R + y_\ell \begin{pmatrix} \bar{\nu} \\ \bar{\ell} \end{pmatrix}_L \phi\, \ell_R + \text{h. c.} \right) .\end{aligned} \tag{1.2}$$

The fields appearing in this Lagrangian are the gauge bosons G^a_μ, W^a_μ, and B_μ, the scalar field ϕ, that transforms as a doublet under $SU(2)_L$, and the fermionic fields f. Suppressing the generation indices we can distinguish the fermionic fields as up–type quarks u, down–type quarks d, charged leptons ℓ and neutrinos ν. From the gauge bosons we built the field strength tensors,

$$G^a_{\mu\nu} = \partial_\nu G^a_\mu - \partial_\mu G^a_\nu + g_s f^{abc} G^b_\mu G^c_\nu \tag{1.3}$$

$$W^a_{\mu\nu} = \partial_\nu W^a_\mu - \partial_\mu W^a_\nu + g \epsilon^{abc} W^b_\mu W^c_\nu \tag{1.4}$$

$$B_{\mu\nu} = \partial_\nu B_\mu - \partial_\mu B_\nu \ , \tag{1.5}$$

for the kinetic terms of the bosons. The coupling of the strong and weak interaction are given by g_s and g. The structure constants f^{abc} and ϵ^{abc} of the $SU(3)_C$ and $SU(2)_L$ gauge groups determine their non–Abelian behavior.

The kinetic terms of the fermions and the scalar field include the covariant derivative

$$D_\mu = \partial_\mu - ig \frac{\sigma^a}{2} W^a_\mu - ig \frac{1}{2} B_\mu - ig_s \frac{\lambda^a}{2} G^a_\mu \ , \tag{1.6}$$

where σ denotes the Pauli matrices and λ^a the Gell–Mann matrices. The contribution from the gluon field only appears when the covariant derivative is applied to quarks, since leptons and the scalar field are singlets under the $SU(3)$ transformation. The remaining terms of the Lagrangian are the Higgs potential and the Yukawa terms that couple the fermions to the Higgs boson proportional to the coupling y_i. The Higgs potential contains the only dimensionful parameter μ. For $\mu^2 < 0$ the scalar field acquires a non-vanishing vacuum expectation value $v \equiv \sqrt{2}\,|\langle\phi\rangle|$ determined by the structure of the scalar potential,

$$v^2 = -\frac{\mu^2}{\lambda} \ . \tag{1.7}$$

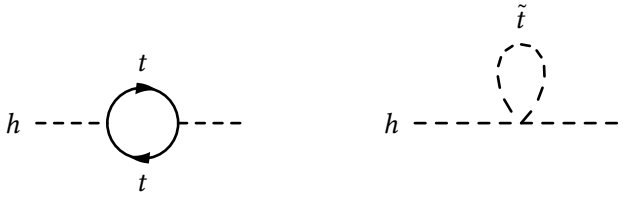

Figure 1.1: Feynman diagrams illustrating loop contributions from top (left) and stop (right) to the Higgs mass.

and we can write the Higgs doublet as

$$\phi = \frac{1}{\sqrt{2}} \begin{pmatrix} -w^2 - iw^1 \\ v + h + iw^3 \end{pmatrix} . \tag{1.8}$$

The scalar field h denotes the Higgs particle. As a consequence the electroweak gauge symmetry is broken $SU(2)_L \times U(1)_Y \to U(1)_Q$ and the resulting Goldstone bosons w^i become the longitudinal degrees of freedom of the gauge bosons $W^\pm$ and Z, combinations of the gauge eigenstates W^a and B, thereby allowing them to acquire mass. The fermions likewise become massive with masses proportional to their Yukawa couplings leading to a consistent description of high energy physics.

However, the special role of the Higgs boson as the only fundamental scalar in the SM leads to a fine tuning problem known as the hierarchy problem. The fermionic couplings of the Higgs induce loop corrections to the Higgs mass as illustrated in Fig. 1.1 of the form

$$\Delta m_h = -\frac{N_c \left|y_f\right|^2}{8\pi^2} \left[\Lambda^2 - 2m_f^2 \ln\left(\frac{\Lambda}{m_f}\right) + \dots\right] , \tag{1.9}$$

where Λ is the cutoff scale at which new physics is expected to enter. If we assume that the SM is valid up to the Planck scale, these loop corrections become very large, about 30 orders of magnitude larger than the measured Higgs mass. The cancellation of the loop corrections with the counterterms then requires an immense fine tuning.

One possible solution to the hierarchy problem is a systematic cancellation of loop corrections. This can be achieved by introducing an additional symmetry transformation Q, that relates fermions and bosons with identical couplings,

$$Q\,|\text{Boson}\rangle = |\text{Fermion}\rangle \qquad Q\,|\text{Fermion}\rangle = |\text{Boson}\rangle \ . \tag{1.10}$$

The underlying symmetry is called supersymmetry (SUSY) [20, 21] and is one of the most popular theories for physics beyond the Standard Model (BSM). Since the corrections from

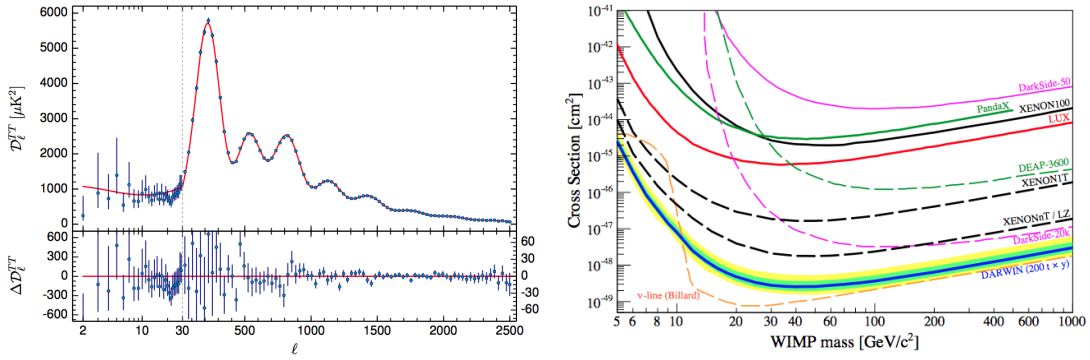

Figure 1.2: Left: Temperature power spectrum of the CMB, measured by Planck published in Reference [30]. Right: Measured and expected bounds on spin–independent WIMP nucleon cross–section from current and future direct detection experiments published in Reference [31].

scalar particles coupling to the Higgs enter with the opposite sign than those from fermions, the leading contributions from fermions and scalars with identical coupling would cancel each other. A complete cancellation would in addition require each pair of fermions and scalars to have the same mass. Since no such partner particles have been seen, we have to assume that the masses of the undiscovered particles exceed the mass spectrum of the SM, leaving us with logarithmic divergences, depending on the mass ratio of scalars and fermions. Note, that these divergences will still cancel each other partially for sufficiently small mass differences. The systematic cancellation of loop contributions occurs as well for the mass contributions of the gauge bosons when we introduce corresponding fermionic degrees of freedom. Of course SUSY is not the only theory offering a solution to the Hierarchy Problem. Other famous examples are for instance composite Higgs models [22–25] or extra dimensions [26–29].

From the theory point of view further unsolved questions remain, that cannot be explained with the SM in its current form. There is for instance the flavor puzzle, the strong hierarchy in the Yukawa couplings of the quarks and leptons, or the search for a grand unifying theory, connecting electroweak and strong interactions. In addition we are still missing out on conclusive explanations for the neutrino mass origin and hierarchy, Baryogenesis and the measured deviation of the anomalous magnetic moment of the muon from the SM prediction. Certainly one of the most pressing evidence for physics beyond the SM arises from astronomical observations. The Planck satellite estimated the mass/energy content of the Universe to be 68.3% of dark energy, 26.8% of dark matter and only 4.9% of ordinary matter [30] from the temperature spectrum of the cosmic microwave background (CMB) displayed in Fig. 1.2. Hence the SM describes only about 5% of the energy density of the Universe. A primary goal of physics beyond the Standard Model is thus to explain the nature of dark matter.

In principle three different experimental approaches are used to learn more about dark matter. Direct detection experiments like XENON1T [32] and LUX [33] try to detect dark matter via its interaction with nucleons. Relying on low backgrounds they can set strong limits on the spin-dependent and spin-independent cross section as a function of the mass of the dark matter particle. Fig. 1.2 shows attainable bounds from nobel liquid detectors. Collider experiments like the LHC try to produce new particles that can be detected e. g. as resonances [34] or missing transverse momentum in mono-jet searches [35]. Finally there are indirect detection experiments like FERMI–LAT [16]. They look for the products of dark matter annihilation into SM particles. Photons are very promising candidates, as they are easy to detect and can travel very long distances without interaction.

Since the discovery of the first evidence of dark matter, the precision of astrophysical experiments has increased enormously. Recent measurements by PLANCK are able to determine the dark matter relic density from a global fit of the Λ–CDM model including further input parameters with a precision of better than 2%.

Many different models have been developed that offer explanations for one or more of the mentioned problems, in particular dark matter. From previous measurements we expect a potential dark matter candidate to fulfill certain criteria: It should be massive, dark i.e. not charged under the electromagnetic interaction, stable on cosmological scales, sufficiently cold to form structures and reproduce the relic abundance measured by PLANCK. One of the most promising candidates for dark matter are weakly interacting massive particles, WIMPs, which by definition fulfill the first two criteria. In Chapter 3 we will start by reviewing the evidence for dark matter, the WIMP model as a solution to the dark matter problem, and the associated calculation of the relic density. It will turn out that WIMP dark matter yields automatically a relic density in the range of the measured value.

Supersymmetric models provide such a WIMP candidate for dark matter, in the form of the lightest supersymmetric particle (LSP). Protected by a symmetry, it can not decay into SM particles and is hence stable. If the LSP is a neutralino, then it interacts only weakly, fulfilling all WIMP criteria. We will discuss the resulting phenomenology for supersymmetric models in the second part of Chapter 3.

In addition to the PLANCK measurement of the relic density, FERMI–LAT has measured a gamma-ray excess in the few GeV range from the GC. If this signal originates from the annihilation of DM, it would provide a complementary constraint on SUSY DM models. This interpretation is motivated by the remarkable fact, that the necessary annihilation cross section to fit the GC excess is of the same order of magnitude as the cross section for the relic density.

In Chapter 4 we explore SUSY dark matter annihilating via various channels like the SM-Higgs h, a pseudoscalar, A, and the Z boson into $b\bar{b}, W^+W^-$ and $t\bar{t}$ to model the GC excess. Using SFITTER, we include the latest result from the Fermi collaboration itself to perform a fit within the minimal supersymmetric extension of the SM (MSSM) including all spectral information.

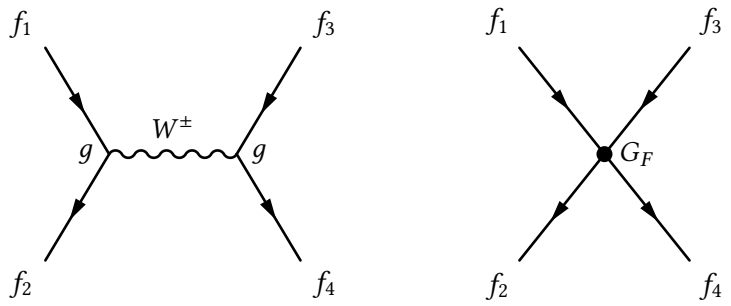

Figure 1.3: Feynman diagrams illustrating the full matrix element for the W mediated s–channel and the effective Fermi theory.

The large theoretical and statistical uncertainties allow a combination of the GC excess with the relic density, taking into account the difference in velocity distributions between the early Universe and today. We find that in particular the annihilation via a pseudoscalar shows a good agreement with data and avoids constraints from direct detection.

In Chapter 5 we establish a connection between the astrophysical observations and Higgs measurements at the LHC. Therefore we focus on light dark matter solutions to the GC excess which allow for an enhanced invisible branching ratio of the SM like Higgs. For this setup we rely on an efficient annihilation channel for dark matter masses in the range of 30 to 60 GeV. The framework of the next to minimal supersymmetric extension of the SM (NMSSM), which adds an additional singlet to the MSSM, provides a sufficiently light pseudoscalar to create a large enough annihilation cross section while avoiding a light charged Higgs that is excluded by LHC searches. SFitter allows us to link the dark matter fit to LHC Higgs observables like the invisible branching ratio, while controlling the mixing between SUSY and SM like Higgs. We find that it is possible to see an enhanced invisible branching ratio in agreement with all Higgs observables while simultaneously fitting the dark matter observables. The results of the global NMSSM fits of the GC excess including the relic density, limits from direct detection and collider searches are discussed in Chapter 5.

The NMSSM analysis illustrates how BSM models defined at a high scale often lead to small deviations from SM predictions at low scales, e.g. in the Higgs sector. As a complimentary approach to a specific high scale model, EFTs are used to parametrize deviations from the SM in a rather model independent way. They extend the SM Lagrangian with additional operators build from SM particles and their derivatives.

A well known example in the history of particle physics is Fermi theory as an effective theory of the SM. Before the discovery of the W boson the beta decay was described by a four fermion interaction with the coupling $G_F[\text{GeV}^{-2}]$ displayed in Fig. 1.3. In the SM, the interaction is instead transmitted via a W boson. The full matrix element therefore includes the W-propagator,

yielding

$$\mathcal{M} \propto \frac{g^2}{p^2 - m_W^2} \ . \tag{1.11}$$

From the form of the propagator it can be seen that at low energies $p^2 \ll m_W^2$ the denominator is dominated by the W mass and Fermi theory is a valid approximation of the full matrix element. The Fermi constant can therefore be expressed in terms of the electroweak theory by

$$G_F = \frac{\sqrt{2}}{8} \frac{g^2}{m_W^2} \ . \tag{1.12}$$

This behavior nicely illustrates how in a low–scale limit one can map a specific perturbative model to an EFT, such that the low–scale impact of new particles is parametrized via higher dimensional operators. Only when approaching the pole condition we observe deviations from Fermi theory requiring the full SM description. For a detailed introduction to EFTs see Reference [36].

In Chapter 6 we introduce the relevant operators for a Higgs–EFT. We combine searches from ATLAS and CMS to constrain the dimension-6 operators of the Higgs sector in an effective extension of the Standard Model. LHC searches related to triple gauge vertices (TGV) provide a powerful additional constraint. We simulate the distributions for different channels including showering and detector simulation for ATLAS and CMS. The derived parametrization of the distribution is used to fit the EFT to the experimental data. Careful correlation of related uncertainties between distinct searches of each experiment are central in the last step of the combination when we compute the likelihood distribution. The combined limits on the anomalous TGV that we obtain from our analysis of LHC data, are about a factor of 2 to 5 stronger than the known limits from LEP. Adding this analysis to the SFitter Higgs EFT fit leads to even stronger constraints on correlated operators.

In Chapter 7 we summarize the content of the thesis, highlighting the most important results. We thereby give an answer to the driving questions formulated at the beginning of this introduction.

Chapter 2

SFitter

The central tool used for all fits in this thesis is SFitter [17, 18, 37, 38], a multipurpose fitting program that can be used to fit data from dark matter searches [39], Higgs observables [19, 40–42], electroweak precision measurements [3] and many other experiments [5]. The basic idea of every fit is very simple. Experiments provide data in the form of measured numbers of events, cross sections and exclusion limits. Theorists on the other hand construct models that predict the same observables. The fit compares data with predicted observables and assigns a likelihood value that characterizes the agreement. The aim is to find a list of best fit points and exclusion limits for the tested model. For this purpose we have to scan the parameter space and compute the likelihood of every tested parameter point. This general concept is illustrated in Fig. 2.1.

In order to build the full likelihood function from data, a crucial step is the correct treatment of theoretical and experimental uncertainties. Systematic, statistical and theory uncertainties are taken into account using Gaussian, Poisson or box shaped uncertainty distributions according to their interpretation. The full likelihood including all uncertainties is determined by consistently profiling over the corresponding nuisance parameters. In Sec. 2.1 we discuss in detail how the likelihood function is built from data, including the correlation of identical sources of uncertainties in different observables.

Having determined the likelihood of a single parameter point, we need to efficiently scan the parameter space of the model to build a likelihood map. SFitter uses several minimization algorithms to search the model parameter space for best fit points, including Markov chains, a stochastic process for which the choice of the next parameter point exclusively depends on the current state. Sec. 2.2 illustrates the most important algorithms and techniques to improve the performance of the fit.

For the computation of the model predictions, SFitter relies on a large number of tools like SUSY spectrum calculators and dedicated dark matter programs to compute observables e.g. the relic density. The last section focuses on the technical aspects of SFitter and its interfaces with external programs.

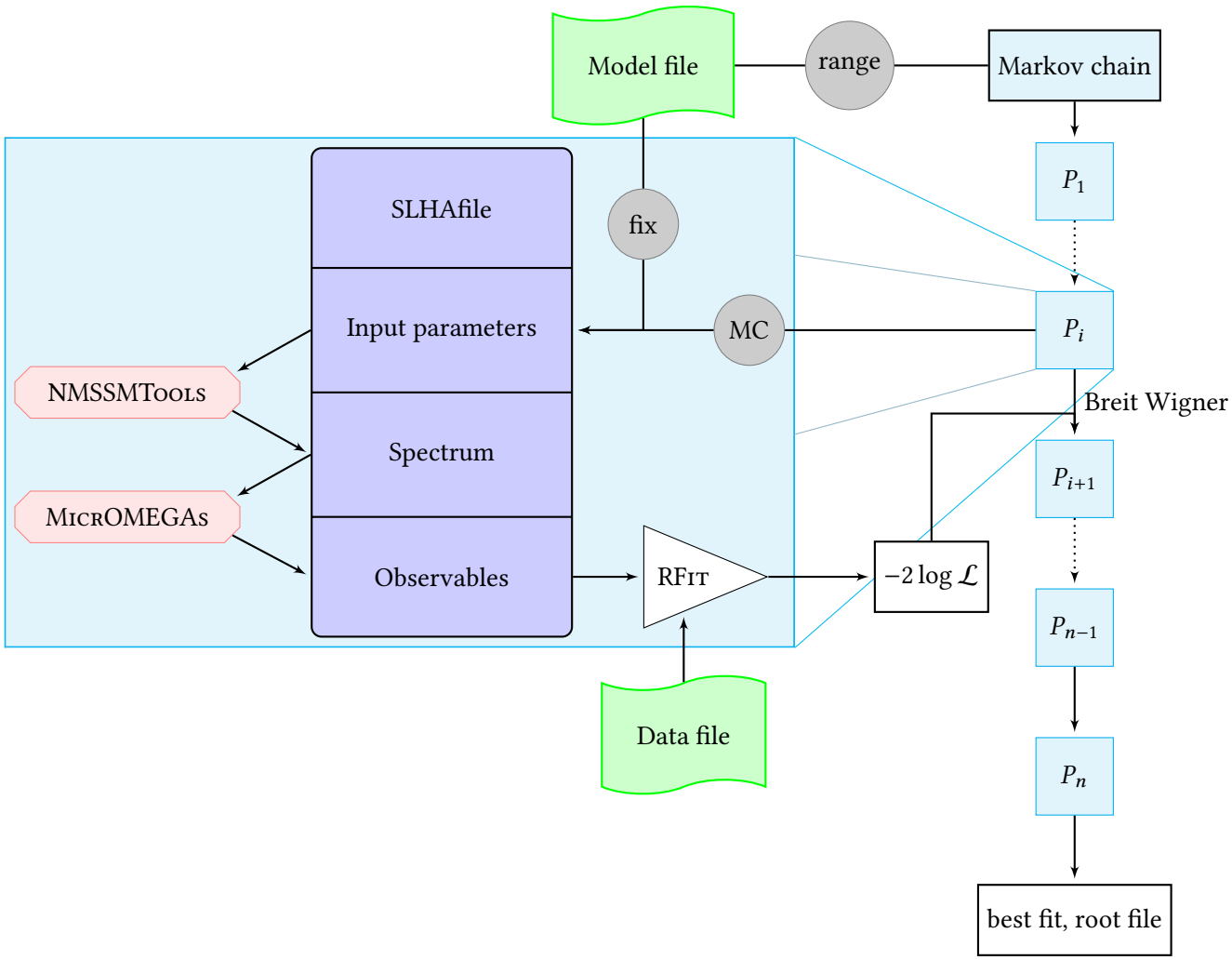

Figure 2.1: SFitter flow diagram. A detailed description of the architecture of the program is given in Sec. 2.3

2.1 The likelihood function

The likelihood is the central function to describe the agreement between model and data. In order to introduce the concept of a likelihood function we start with the definition of probability as a frequentist concept [43]. Let us assume we perform an experiment to measure the observable x. Repeating the experiment many times will result in different values of x. The resulting distribution generates the probability density function of x, $f(x)$. Using this distribution we can determine the probability p to measure x within the interval $[x_{min}, x_{max}]$,

$$\int_{x_{min}}^{x_{max}} f(x)dx = p \ . \tag{2.1}$$

This concept of probability is well defined within the frequentist framework. In order to include a specific model we insert the dependence on a model parameter α and consider $f(x|\alpha)$. For each value of alpha the probability density function is normalized to 1,

$$\int_{-\infty}^{+\infty} f(x|\alpha)dx = 1 \ . \tag{2.2}$$

Starting from a given measurement, the situation is inverted. Instead of the well–defined probability to measure a certain value given a fixed parameter, we now want to know the likelihood that a parameter choice α is a valid hypothesis given a measured observable. Fixing x to an observed value, we define the likelihood function $\mathcal{L}(\alpha|x) = f(x|\alpha)$, which is no longer normalized to 1. Using the likelihood function, one can determine the best–fit value α_{best} for which the likelihood is maximal. For practical purposes one often minimizes the log-likelihood $-2\log\mathcal{L}(\alpha)$ instead of maximizing the likelihood as the product of likelihood functions becomes a simple sum of log-likelihood functions. In the final analysis, we will consider the likelihood ratio function, that divides the likelihood of a given parameter point that we want to test - the null hypothesis θ_0 - by the supremum of the likelihood of the full parameter space Θ, i.e. the best fit point,

$$\lambda = -2\log\frac{\mathcal{L}(\theta_0|x)}{\sup_{\theta\in\Theta}\mathcal{L}(\theta|x)} \tag{2.3}$$

$$= -2\log\frac{\mathcal{L}(\alpha)}{\mathcal{L}(\alpha_{best})} \ . \tag{2.4}$$

This approach is motivated by the Neyman–Pearson lemma that states that the likelihood ratio is the most powerful test statistics to discriminate between two hypotheses [44]. According to Wilks' theorem, under certain conditions like a large sample size, this likelihood ratio function follows a χ^2 distribution with Δn degrees of freedom [45]. Here, Δn corresponds to the difference in the number of degrees of freedom of the null hypothesis and the full parameter space. In the two dimensional projections of the likelihood maps that we discuss in this thesis, we profile over all but the displayed degrees of freedom so that $\Delta n = 2$. Wilks' theorem finally

allows us to interpret the displayed likelihoods in a meaningful way, perform actual hypothesis testing, and exclude regions of the parameter space.

In the following we will discuss how to build a likelihood function from experimental results. The most crucial part when including data into a fit is the treatment of uncertainties. In order to build a correct likelihood function we have to assign appropriate distributions - *Gaussian, Poisson, or flat* - to the different types of uncertainties - *systematic, statistic, theoretical* - and correlate them within different channels of the same experiment. In the following we will discuss the different classes of uncertainties one by one.

2.1.1 Poisson distribution

Statistical uncertainty is inherent to every measurement. Poisson distributions are used to describe statistic uncertainties when we consider a large number of independent tries N, a small probability p to observe an event and when their product results in a finite number of events $N \cdot p$. These conditions are exactly fulfilled at the LHC, as well as for the observation of γ-rays from the Galactic Center. The probability to observe d events when you expect $\tilde{d}$ events is then given by

$$P(d|\tilde{d}) = \frac{e^{-\tilde{d}}\tilde{d}^d}{d!} \; . \tag{2.5}$$

This distribution is maximal for both $d = \tilde{d} - 1$ and $d = \tilde{d}$ and is normalized to 1,

$$\sum_{d=0}^{d=\infty} P(d|\tilde{d}) = e^{-\tilde{d}} \sum_{d=0}^{d=\infty} \frac{\tilde{d}^d}{d!} = e^{-\tilde{d}} e^{\tilde{d}} = 1 \; . \tag{2.6}$$

For a standard LHC channel the total number of measured events will be the sum of the signal we are interested in and some indistinguishable background. Thus we have to consider the sum of two numbers s and b that follow Poisson distributions. If we assume that we know the mean of the background distribution $\tilde{b}$ very precisely, we can compute the probability to measure d events assuming a mean $\tilde{s}$ of the signal,

$$\begin{aligned} P(d|\tilde{s},\tilde{b}) &= \sum_{s,b=0}^{d} \frac{e^{-\tilde{s}}\tilde{s}^s}{s!} \frac{e^{-\tilde{b}}\tilde{b}^b}{b!} \delta(d-s-b) \\ &= \frac{e^{-(\tilde{s}+\tilde{b})}}{d!} \sum_{s=0}^{d} \binom{s}{d} \tilde{s}^s \tilde{b}^{d-s} \\ &= \frac{e^{-(\tilde{s}+\tilde{b})}(\tilde{s}+\tilde{b})^d}{d!} \; . \end{aligned} \tag{2.7}$$

We simply recover the Poisson distribution for $\tilde{d} = \tilde{s} + \tilde{b}$ events which is expected. Assuming d has been measured we can now define the likelihood for the parameter $\tilde{s}$ to be

$$\mathcal{L}_{Poiss}(\tilde{s}|d,\tilde{b}) = \frac{e^{-(\tilde{s}+\tilde{b})}(\tilde{s}+\tilde{b})^d}{d!}. \tag{2.8}$$

While this is well defined, the precise value of $\tilde{b}$ is usually unknown. Instead, a measurement has been carried out in a control region resulting in the measured value of b. The result of this measurement is then extrapolated into the signal region using for example the ABCD method [46]. The key observation we have to make here, is that the background expectation is subject to a measurement and consequently to statistical fluctuations in this measurement. This second measurement has to be taken into account to evaluate $\tilde{b}$ in the signal region. The combined probability to measure b and d is given by

$$P(b,d|\tilde{s},\tilde{b}) = \frac{e^{-(\tilde{s}+\tilde{b})}(\tilde{s}+\tilde{b})^d}{d!}\frac{e^{-\tilde{b}}\tilde{b}^b}{b!}. \tag{2.9}$$

For simplicity we assume throughout this argument that the expected number of background events in the signal and the control region agree. In general this assumption is not justified and often the control region benefits from larger event numbers. We take this effect into account in the SFitter framework by inserting a scale factor into the background distribution. Using a frequentist approach we profile over all possible values of $\tilde{b}$ to find the likelihood function of $\tilde{s}$.

$$\mathcal{L}_{Poiss}(\tilde{s}|d,b) = \max_{\tilde{b}} \frac{e^{-(\tilde{s}+\tilde{b})}(\tilde{s}+\tilde{b})^d}{d!}\frac{e^{-\tilde{b}}\tilde{b}^b}{b!}. \tag{2.10}$$

In the limit of a large number of events, we can approximate the Poisson distributions with a Gaussian function. In this case the limit can be computed analytically,

$$\begin{aligned}\mathcal{L}_{Gauss}(\tilde{s}|d,b) &= \max_{\tilde{b}} \frac{1}{\sqrt{2\pi d}} e^{-\frac{(d-\tilde{b}-\tilde{s})^2}{2d}} \frac{1}{\sqrt{2\pi b}} e^{-\frac{(b-\tilde{b})^2}{2b}} \\ &= \frac{1}{2\pi\sqrt{db}} e^{-\frac{(d-b-\tilde{s})^2}{2(d+b)}}.\end{aligned} \tag{2.11}$$

The profiled likelihood is again described by a Gaussian distribution. Its width is given by the widths of the individual data and background distributions added in quadrature.

However, for small numbers of events the approximation does not hold and we have to solve the problem numerically. It is therefore convenient to consider instead the logarithm of the likelihood, turning products of likelihoods into sums of log–likelihoods. Following Wilks' theorem we redefine the likelihood as a generalized χ^2 that vanishes when the prediction

reproduces the observed number of events,

$$\begin{aligned} -2\log\mathcal{L}_{Poiss}(\tilde{s}|d,b) &\equiv \chi^2 \\ &= -2\log\left(\frac{P(b,d|\tilde{s},\tilde{b})}{P(\tilde{b},\tilde{d}|\tilde{s},\tilde{b})}\right) \\ &= -2\max_{\tilde{b}}\left[(d-\tilde{s}-\tilde{b})\log(\tilde{s}+\tilde{b})+(b-\tilde{b})\log(\tilde{b})+\log\left(\frac{(\tilde{s}+\tilde{b})!}{d!}\frac{\tilde{b}!}{b!}\right)\right]. \end{aligned} \tag{2.12}$$

This is the final form of the likelihood measure that we would like to implement. However, in favor of a computing time efficient analysis we cannot perform a maximization for each data point of each point of the Markov chain. Instead we use an approximation of Eq. (2.12). We split the Poisson likelihood into two contributions, originating from data and background measurements:

$$-2\log\mathcal{L}_{Poiss,d}(\tilde{s}|d,b) = -2\left[(d-(\tilde{s}+b))\log(\tilde{s}+b)+\log\left(\frac{(\tilde{s}+b)!}{d!}\right)\right] \tag{2.13}$$

$$-2\log\mathcal{L}_{Poiss,b}(\tilde{s}|d,b) = -2\left[(b-(d-\tilde{s}))\log(d-\tilde{s})+\log\left(\frac{(d-\tilde{s})!}{b!}\right)\right] \tag{2.14}$$

The likelihood contribution from the data measurement uses $\tilde{d} = \tilde{s} + b$ as a prediction for the total number of events, the second contribution approximates the predicted number of background events by $\tilde{b} = d - \tilde{s}$ using the measured number of events. This reflects that a deviation of predicted signal and measured signal can be caused by a fluctuation of the data as well as a fluctuation of the background.

The two contributions are then combined via the approximate formula

$$\frac{1}{\log\mathcal{L}_{Poiss}} \approx \frac{1}{\log\mathcal{L}_{Poiss,d}} + \frac{1}{\log\mathcal{L}_{Poiss,b}} \tag{2.15}$$

which becomes exact in the Gaussian limit in Eq. (2.11).

In Fig. 2.2 we illustrate the validity of this approximation. We show the full Poisson treatment using the maximization over the predicted number of background events, the usual Gaussian approximation that is valid for large number of events and the approximate treatment carried out by SFitter. The green line represents the profiled Poisson distribution, the red line the SFitter approximation and the blue line shows the Gaussian treatment. We see that for all cases, the approximation done by SFitter describes the Poisson distribution better than the Gaussian approximation. For large event numbers all three lines coincide, while for smaller numbers, the lines diverge for large deviations from the best fit point. Zooming into the left and the middle figure, we find a perfect agreement between the approximation and the Poisson

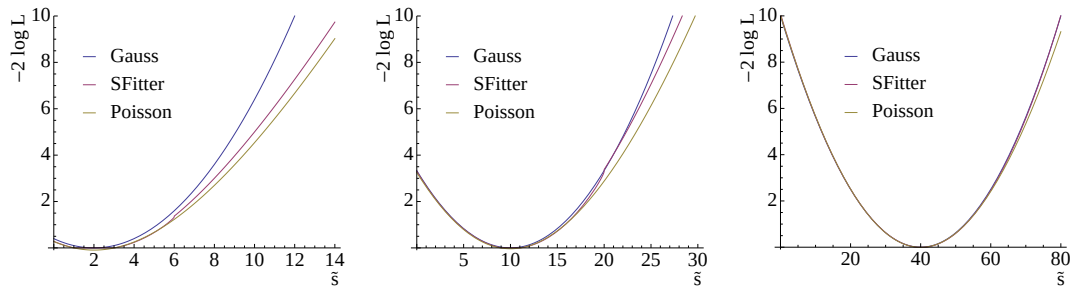

Figure 2.2: Illustration of the validity of Eq. (2.15) for different values of d and b. The displayed curves show the exact solution (green), the Gaussian approximation (blue), and the approximation done by SFitter (red). From left to right the values for (d, b) are $(6, 4)$, $(20, 10)$, $(100, 60)$.

distribution for $\tilde{s} < 5.5$ and $\tilde{d} < 17$, where we need a high precision. For $\tilde{s} = d$ the background contribution of the approximation diverges and we see some deviation with respect to the Poisson distribution. However for larger values of $\tilde{s}$ the shape of the approximation follows again the Poisson distribution, keeping only a small relative offset. The overall agreement of the approximation and the exact distribution is very good, especially around the best fit point, making Eq. (2.15) a valid approximation.

2.1.2 Gaussian distributions

In reality probability density functions describing the number of events are not known exactly, but depend on some unknown nuisance parameters. Typical examples are the uncertainty on the luminosity of a collider or the photon reconstruction efficiency of a calorimeter for instance at Fermi-LAT or at an LHC experiment. The knowledge about these nuisance parameters can be described by an additional contribution to the likelihood. Since these parameters are usually determined with large data samples this contribution typically follows a Gaussian distribution. The corresponding likelihood is then given by

$$\mathcal{L}_{Gauss}(\tilde{d}|d) = \frac{1}{\sqrt{2\pi}\sigma_{sys}} \exp -\frac{(d - \tilde{s} - b)^2}{2\sigma_{sys}^2} \ . \tag{2.16}$$

where d stands for the measured data and $\tilde{d}$ for the predicted number of events. Moving from likelihood to log-likelihood, the prefactor becomes a constant offset. Again, we want to normalize the likelihood such, that $\mathcal{L}(d = \tilde{d}) = 1$.

$$-2 \log \mathcal{L}_{Gauss}(\tilde{d}|d) = \frac{\left(d - \tilde{d}\right)^2}{\sigma_{sys}^2} = \chi^2 \ . \tag{2.17}$$

When we are looking for BSM physics we consider the Standard Model as a background and the data as the sum of signal and background: $d = s + b$. What we are actually looking for is therefore the likelihood of the BSM signal $\tilde{s}$ given the data point $s = d - b$. The resulting uncertainty on s depends on the correlation of data and background:

$$\sigma_s^2 = \left(\frac{\partial s}{\partial d}\sigma_d\right)^2 + \left(\frac{\partial s}{\partial b}\sigma_b\right)^2 + 2\rho\frac{\partial s}{\partial d}\frac{\partial s}{\partial b}\sigma_d\sigma_b \tag{2.18}$$

$$= \begin{cases} \sigma_d^2 + \sigma_b^2 & \text{for } \rho = 0 \text{ (uncorrelated)} \\ (\sigma_d - \sigma_b)^2 & \text{for } \rho = 1 \text{ (fully correlated)} \end{cases} \tag{2.19}$$

ρ is the correlation coefficient that can vary between -1 and 1. As the events originating from the signal process are subject to the same systematic uncertainties (e.g. luminosity or lepton reconstruction efficiency) as the events from the background process, we assume full correlation between data and background. The likelihood contribution arising from the systematic uncertainties are therefore calculated using

$$\begin{aligned} -2\log\mathcal{L}_{Gauss}(\tilde{d}|d) &= \frac{(d-b-\tilde{s})^2}{\sigma_{s,syst}^2} \\ &= \frac{(d-b-\tilde{s})^2}{\sum_{syst}(\sigma_{d,i}-\sigma_{b,i})^2} \end{aligned} \tag{2.20}$$

In the last line we generalize the formula for different sources of systematic uncertainties. Given their Gaussian nature, they are combined in quadrature.

2.1.3 Flat distributions

The third class of uncertainties are described by flat distributions,

$$\mathcal{L}_{\text{Flat},s} = \Theta((\tilde{s}+\sigma_s)-s)\Theta(s-(\tilde{s}-\sigma_s)) \quad \Longleftrightarrow \quad \tilde{s} \in [s-\sigma_s, s+\sigma_s] \,, \tag{2.21}$$

where Θ is the Heaviside function. In this case the prediction of the signal has to be within a certain range of the data s, otherwise its likelihood vanishes. Within the allowed range there is no discrimination between different values. A typical situation in which we apply these kind of uncertainties are scale dependencies in higher order calculations. A common way to determine σ_s is for example to vary the scale that is used in the calculation of the observables by a factor of 2 in both directions. In this case this treatment has no statistical significance and the values of σ_s do NOT correspond to a well defined statistical interpretation.

Another example is the γ–ray spectrum from Fermi–LAT where we use a flat uncertainty to cover the differences between the different background models. As we have no means to determine which model is closer to a "true" model, we have to assume that the likelihood

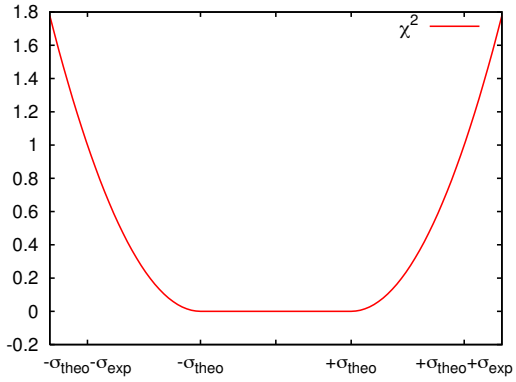

Figure 2.3: Illustration of the RFit scheme for the combination of flat and Gaussian uncertainty. The x–axis indicates the difference between predicted number of events and data. The y–axis shows the corresponding log–likelihood. This figure is taken from Reference [48].

distribution is flat between the minimal and maximal value predicted by the set of models.

For LHC measurements, typically more than one theoretical uncertainty enters the calculation. For instance a measurement of a Higgs channel has to take into account theory uncertainties arising from parton distribution functions (PDF), α_s and higher order corrections. Using the frequentist approach we start by varying the prediction within the allowed range of the first uncertainty to maximize the likelihood. The resulting prediction is once again varied within each of the remaining theory uncertainties to maximize the likelihood. This is equivalent to combining the theoretical uncertainties linearly into one flat uncertainty:

$$\sigma_{theo,\tilde{s}} = \sum_{theo} \sigma_{theo} \tag{2.22}$$

2.1.4 Combining different uncertainties

Having determined the forms of all uncertainties, we proceed to combine them into one likelihood function. Due to the theory uncertainty the predicted signal is fixed up to a nuisance parameter s^*. We have to profile over this nuisance in order to combine theory and systematic uncertainty into a meaningful likelihood function. This procedure is called the RFit scheme [47].

$$\begin{aligned}\mathcal{L} &= \max_{s^*} \Theta\left[s^* - (\tilde{s} - \sigma_{theo})\right] \Theta\left[(\tilde{s} + \sigma_{theo}) - s^*\right] \exp - \frac{(d-b-s^*)^2}{2\sigma_{sys,s}^2} \\ &= \max_{s^* \in [\tilde{s}-\sigma_{theo}, \tilde{s}+\sigma_{theo}]} \exp - \frac{(d-b-s^*)^2}{2\sigma_{sys,s}^2}.\end{aligned} \tag{2.23}$$

Maximizing the likelihood results in a shift of the predicted signal towards the actual data. The log-likelihood can therefore be expressed by

$$\sqrt{-2\log\mathcal{L}} = \chi = \begin{cases} \dfrac{s-(\tilde{s}+\sigma_{theo})}{\sigma_{sys,s}} & \text{for } \sigma_{theo} < s-\tilde{s} \\ 0 & \text{for } \sigma_{theo} > |s-\tilde{s}| \\ \dfrac{s-(\tilde{s}-\sigma_{theo})}{\sigma_{sys,s}} & \text{for } \sigma_{theo} < \tilde{s}-s \end{cases} \tag{2.24}$$

The resulting log-likelihood function, a parabola that is cut open at its minimum, is shown in Fig. 2.3.

For the Gaussian case the treatment of data and prediction is symmetric. Therefore it makes no difference whether we shift the data towards the prediction or vice versa. However for the Poisson distribution the two treatments would yield different results. Following the formalism above it becomes clear that, to take into account the theory uncertainty, we have to shift the prediction by the theory uncertainty towards the data. If data and prediction differ by less than the theory uncertainty, the likelihood is set to one. Otherwise the log-likelihood contributions in Eq. (2.14) are modified to

$$-2\log\mathcal{L}_{Poiss,d}(\tilde{s}|d,b) = -2\left[(d-(\tilde{d}\pm\sigma_{theo}))\log(\tilde{d}\pm\sigma_{theo}) + \log\left(\frac{(\tilde{d}\pm\sigma_{theo})!}{d!}\right)\right], \tag{2.25}$$

with $\tilde{d} = \tilde{s} + b$.

Finally, we have to combine the Poisson and Gaussian distributions to one likelihood function. As for the combination of Poisson uncertainties for data and background, this would require a numerical treatment to profile over the nuisance parameters. However, we found that the approximate formula

$$\frac{1}{\log\mathcal{L}} = \frac{1}{\log\mathcal{L}_{Gauss}} + \frac{1}{\log\mathcal{L}_{Poiss,d}} + \frac{1}{\log\mathcal{L}_{Poiss,b}} \tag{2.26}$$

results as well in a very good agreement for small number of events, reducing the computing time. In the limit of large event numbers when the Poisson distribution can be replaced by a Gaussian with $\sigma_{Gauss} = \sigma_{Poiss} = \sqrt{d}$ the approximate formula actually becomes exact. The expression illustrates that the combined likelihood is dominated by the largest likelihood, which corresponds to the largest uncertainty.

2.1.5 Correlations

We already mentioned the necessity of including correlations between the data and the background. Indeed when combining the likelihood contributions of different bins of one distribution

and even of different channels at the same experiment we have to take into account the correlation of systematic uncertainties of the same type, such as those associated with luminosity or lepton reconstruction efficiency. This is quantified by the correlation matrix C

$$C = \text{corr}(X_i, X_j) = \frac{E[(X_i - \overline{X}_i)(X_j - \overline{X}_j)]}{\sigma_i \sigma_j} , \tag{2.27}$$

where E denotes the expectation value and $\bar{X}$ the mean value of X. By construction the correlation matrix is symmetric and the diagonal entries are equal to 1. For the off-diagonal entries we find

$$C_{ij} = \frac{\sum_{syst} \sigma_{i,syst} \sigma_{j,syst} \cdot \rho_{i,j,syst}}{\sigma_{i,exp} \sigma_{j,exp}}, \tag{2.28}$$

for two channels i and j. The systematic uncertainties of each channel are calculated again following Eq. (2.20). The numerator is a sum over all sources of systematic uncertainties weighted with a correlation coefficient ρ. This coefficient is defined as the covariance matrix normalized with respect to the standard deviation and can range from -1 to 1. For uncertainties representing detector and collider parameters, we assume a full correlation for the individual categories and set $\rho_{i,j,syst}$ to 1. In the denominator $\sigma^2_{i,exp}$ is the sum of all experimental - i.e. non–theoretical - uncertainties added in quadrature.

$$\sigma^2_{i,exp} = \sum_{syst} \sigma^2_{syst} + \sum_{poiss} \sigma^2_{poiss} \tag{2.29}$$

The Poisson contribution in the denominator consists of two contributions, $\sqrt{d}$ and $\sqrt{b}$, for each channel. The full log-likelihood is finally computed using:

$$\chi^2 = \vec{\chi}_i{}^T C^{-1} \vec{\chi}_i \tag{2.30}$$

Theoretical uncertainties are not included in the above calculation of the correlation matrix. In the case of Fermi–LAT we assume that they are uncorrelated, as all models use a legitimate approach and the correlations would depend on the specific models. Correlated theory uncertainties can be modeled using nuisance parameters that can vary within a certain interval corresponding to σ_{theo}. The profiling over these nuisance parameters is only done after the global fit when we project the multi-dimensional likelihood function onto a two dimensional plane by profiling over all non-displayed parameters.

2.2 Fitting strategies

Having built the likelihood function, the main objective of SFitter is to calculate which part of the available parameter space is allowed or excluded. Depending on the problem we can be

interested in best fit points and regions as well as exclusion limits. In this process we encounter two major challenges: large number of input parameters and complex dependencies of the likelihood on these parameters for instance from annihilation channels of dark matter particles, both leading to long computing times. Hence we rely on various algorithms to search the parameter space efficiently.

Potentially the most intuitive way to scan a parameter space is to use a grid. This method makes sure that one calculates a point in every region of the considered space. However, this method is not only very inefficient in mapping out special valleys of the likelihood map, but also suffers from a very bad scaling behavior. The number of points necessary to cover the parameter space scales exponentially with the number of fitted parameters.

A better possibility to analyze the likelihood distribution are Markov chains. Applied to our scenario, a Markov chain is a sequence of points in parameter space for which the conditional probability distribution for the next point depends only on the present point and not on any previous part of the chain. In practice we use the likelihood to construct the probability distribution. First we choose a random point x_i in parameter space. If its likelihood is larger than the likelihood of the current state, the point is accepted as the next element of the chain. Otherwise we test if the likelihood of the point fulfills the condition

$$\frac{\mathcal{L}(x)}{\mathcal{L}(current)} \geq r \tag{2.31}$$

with r being a random number in the range [0,1]. This algorithm forces the Markov chain to search for increasingly better points. In the ideal case this approach scales only linearly with the number of input parameters, which allows for fits of a multidimensional parameter space as required for SUSY or global EFT fits.

We can further improve the performance of the Markov chain by replacing the flat random distribution that chooses the point x by a Breit–Wigner distribution that will search with a larger probability closer to the current point. This is motivated by the continuous shape of the likelihood map. If the current point has a high likelihood, it is likely that nearby points have a similar high likelihood. A Gaussian distribution is often not a suitable choice for this purpose as the tails are exponentially suppressed and prevent a complete coverage of the parameter space.

Another possibility is to introduce so–called cooling Markov chains by modifying Eq. (2.31). We can divide the Markov chain in 100 segments numbered with $j = 1 \ldots 100$. We then replace the condition in Eq. (2.31) by

$$\frac{\mathcal{L}(x)}{\mathcal{L}(current)} \geq r^{\frac{100}{j \cdot c}}, \tag{2.32}$$

where the factor c denotes the cooling factor. For small values of j the right hand side is close to zero and almost all points are accepted. Increasing values of j lead to larger numbers on the

right hand side of the equation and thereby to a harder acceptance criterion. Previous SFitter studies found that $c \sim 10$ gives well-converging results [19].

While Markov chains are very useful to scan the parameter space and find multiple minima, other algorithms are better suited to find actual best fit points. For this purpose the MINUIT program [49] is included in SFitter. It includes several methods of which we will list those most frequently used.

The Nelder–Mead method (downhill simplex method)

Let the $n+1$ points $u_0, u_1, \ldots, u_n \in \mathbb{R}^n$ be affinely independent.* A simplex is given by the set of points

$$\Delta = \left\{ x \in \mathbb{R}^n : x = \sum_{i=0}^{k} t_i u_i \text{ with } 0 \leq t_i \leq 1 \text{ and } \sum_{i=0}^{k} t_i = 1 \right\}. \tag{2.33}$$

For low–dimensional cases a simplex corresponds to a point ($n = 0$), a line ($n = 1$), a triangle ($n = 2$) and a tetrahedron ($n = 3$). Starting from a random simplex, the Nelder–Mead method [50] orders the vertices by their values and constructs the centroid of the n best points. Using reflection, expansion and contraction with respect to the centroid, the algorithm tries to find a point with a lower value than x_n. If the algorithm is successful, x_n is replaced by the new point and starts over. Otherwise all points but the best (x_0) are replaced by pushing them closer to the best point. Then the algorithm goes back to the first step. Since the Nelder–Mead method does not rely on the derivative, it is used when its computation becomes unstable. In any other case derivative–based algorithms like MIGRAD are faster and more reliable.

MIGRAD

The simplest minimization algorithm based on a gradient is gradient descent. This algorithm moves along the gradient of the function $f(x)$ that we want to minimize using a predefined step size α_k. Starting from one point x_k, the next point is then given by

$$x_{k+1} = x_k - \alpha_k \nabla f(x). \tag{2.34}$$

Following the gradient will lead eventually to a local minimum of the function $f(x)$. Due to the smaller values of the derivative close to the minimum, the effective step size $x_{k+1} - x_k$ will become smaller and the evaluation more detailed. A more advanced method replaces α_k by the inverse of the Hessian matrix

$$x_{k+1} = x_k - H_f(x)^{-1} \nabla f(x) = x_k - \left(\frac{\partial f(x)}{\partial x_i \partial x_j} \right)^{-1} \nabla f(x). \tag{2.35}$$

*$u_1 - u_0, \ldots, u_n - u_0$ are linearly independent.

This method is called Newton method. The basic idea is to find the value x_{min} for which the gradient vanishes in all directions via a linear approximation. While the convergence of the algorithm is very efficient, the evaluation of the Hessian matrix at each point of the chain is very computing time intensive. Instead, MIGRAD uses a modified version of the Davidson-Fletcher-Powel algorithm [51, 52]. Instead of explicitly computing the Hessian matrix, one starts with a symmetric and positive definite Matrix H_0 and a point x_0 .

The algorithm consist of two parts. First one updates x_k via

$$x_{k+1} = x_k - \alpha_k H_k \nabla f(x_k), \tag{2.36}$$

where α_k is chosen such that it minimizes $f(x_{k+1})$ along the line $x_{k+1}(\alpha)$. In a second step H_k is updated via

$$H_{k+1} = H_k + \frac{p_k p_k^T}{p_k^T q_k} - \frac{H_k q_k q_k^T H_k}{q_k^T H_k q_k} \tag{2.37}$$

with $p_k = x_{k+1} - x_k$ and $q_k = \nabla f(x_{k+1}) - \nabla f(x_k)$. The modification to the matrix H_k keeps the matrix symmetric and positive definite. For $k \to \infty$ the matrix H_k approaches the Hessian matrix. Details on the derivation can be found in [51, 52]. In addition to finding the minimum, the Hessian matrix also provides an estimate of the error matrix as the algorithm converges to the minimum. The interpretation of the Hessian matrix as an error estimate is only valid in the limit of a parabolically shaped likelihood function.

MINOS
MINOS is an alternative algorithm to determine the error matrix around the minimum. It is applied after the minimum has been determined for instance by MIGRAD. For each parameter p the algorithm finds the values for which the log-likelihood function has a fixed offset from the minimal value while profiling over the remaining parameters. This approach also allows for asymmetric error intervals and is therefore needed for very complex likelihood functions.

2.3 SFitter architecture

The constructed likelihood function as well as the minimization algorithms need to be embedded into the context of the full SFitter setup. Therefore, we will briefly describe the architecture of SFitter to highlight the most important features that need to be taken into account in global fits.

Fig. 2.1 illustrates the structure of the program. As input SFitter requires a model and a data file. The model file selects the model and the corresponding parameter space. Each parameter is either fixed or can vary in an individual range. The data file stores the relevant measurements including their uncertainties and determines which uncertainties need to be correlated.

In order to determine the likelihood for a given point in parameter space we have to compute the necessary observables. Therefore external programs like SuSpect [53, 54] are interfaced with SFitter via an SLHA file, the core of the following computations.

For all MSSM analyses [18, 37, 38] we calculate the MSSM spectrum and corresponding B-physics observables with SuSpect3 [53, 54], while the Higgs branching ratios are computed using SUSY-HIT and HDecay [55–57]. For the electroweak precision observables we rely on SusyPope [58]. For constraints specifically for the NMSSM we rely on NMSSMTools [59–62] to calculate the supersymmetric mass spectrum, the Higgs branching ratios, the B observables, $(g-2)_\mu$, and electroweak precision observables. The relic density, the direct detection cross sections and the indirect annihilation rate are calculated with MicrOMEGAs [63] for both supersymmetric models.

The number of events in the Higgs production channels at the LHC for the SM-like Higgs are computed using the standard SFitter-Higgs setup [19, 40, 41].

In Fig. 2.1, the input parameters are handed over to NMSSMTools. SFitter then directly calls the methods implemented in the external program. The computed spectrum, including decay widths and branching ratios, is then stored again in the SLHA file so that MicrOMEGAs can access the mass spectrum and mixing matrices to compute for instance the relic density or direct detection cross sections.

One challenge in this procedure is the compatibility of the different programs. While NMSSMTools is written in fortran, MicrOMEGAs is mainly written in C and SuSpect 3 has a C++ interface with some core functions in fortran. Therefore the interfacing is handled in dedicated parts of SFitter, the so-called SLHAtools. The individual interfaces can cope with the specific properties of the tools. A SuSpect calculation can be accessed via the class definition in SuSpect 3. We have interfaced the spectrum calculation in NMSSMTools as an external fortran routine and for the MicrOMEGAs interface we have implemented the loading of the libraries in a dynamic way due to incompatibilities of MSSM and NMSSM.

After each tool has been executed, all relevant observables are computed. Following Sec. 2.1, measured and predicted data are combined using the RFit scheme to obtain the log-likelihood that measures how well the parameter point describes the data. Finally the log-likelihood is used as feedback in combination with a Breit Wigner to choose the next point of the Markov chain. When the Markov chain has terminated the additional minimization algorithms described in Sec. 2.2 can be applied to map out the region around the minima and refine the best fit point.

Eventually SFitter outputs a list of best fit points, two dimensional likelihood maps, and a ROOT [64] file that contains all relevant information for all tested points. From this file, we can finally infer the exclusion limits and create the likelihood maps displayed in this thesis.

Chapter 3

SUSY Dark Matter

Searches for physics beyond the Standard Model are motivated by a large number of theoretical and experimental observations. One of the strongest arguments, if not the most compelling, is the observation of dark matter in astrophysical measurements. In this chapter, we will first review the evidence for the existence of dark matter and its properties, and discuss how we can relate the measurement of the dark matter relic density by Planck and the γ-ray spectrum by Fermi–LAT to dark matter models. In Sec. 3.2, we introduce the supersymmetric models MSSM and NMSSM as models for dark matter. In the last section we discuss the corresponding dark matter annihilation channels.

Note that Sec. 3.1 is partly extracted from Reference [4]. Parts of all sections have been published previously in References [1, 2].

3.1 Dark Matter

3.1.1 Evidence for dark matter

The first evidence for dark matter were observed and pointed out by Jan Hendrik Oort and Fritz Zwicky in 1932 and 1933. While Oort used the local galactic neighborhood for his measurements - that were later found to be incorrect - Zwicky's observations were determined from the Coma galaxy cluster [65]. Using the virial theorem, he estimated the mass of the cluster from the movement of galaxies at the outer part of the cluster. From comparing the brightness and number of galaxies he deduced a factor of 400 between the visible and the total matter. This factor was later corrected to be smaller by an order of magnitude, e.g. due to updated values of the Hubble constant, but the general claim remained valid.

In the following years many other observations have supported the hypothesis of dark matter. Among the most famous examples we find:

- **Galaxy rotation curves**
  In spiral galaxies the density of luminous matter decreases towards the outer end of the spiral arms. As a consequence the rotation velocity should decrease with increasing

distance from the galactic center. Measurements using the Doppler shift of the Hydrogen line reveal instead a constant distribution of the velocity for large radii.

- **Gravitational lensing**
  General relativity predicts that light follows the geodesics of curved space–time. One side effect is that massive objects or distributions of matter act as a lens by bending light traveling from a distant source towards the observer. Depending on how sizable the effect is, the process is called strong lensing, weak lensing or microlensing. Strong lensing leads to multiple images or lensing arcs, while weak lensing only leads to mild distortions of galaxies turning circular sources into ellipses. Microlensing leads to an apparent change of brightness of the background light source when a massive object is passing through the line of sight and therefore relies on a series of images.
- **Collisions of galaxy clusters**
  A galaxy cluster consists of stars that can be observed via telescopes; hot gas, observed by X-ray measurements; and dark matter, that is located using gravitational lensing. The collision of two galaxy clusters leads to a displacement of the constituents due to different interactions. While the stars are only slowed down by gravitational interaction, the gas interacts electromagnetically causing it to slow down significantly. Observations of collisions have determined that the lensing effect is strongest between the stars and the gas hinting at weakly interacting dark matter that interacts stronger than the stars but much weaker than the gas during the collision [66].
- **Cosmic microwave background (CMB)**
  Photons emitted at the end of recombination in the early Universe are observed today as the cosmic microwave background. The dominant signal is a black body spectrum at a temperature of 2.7 K. However, small anisotropies of the spectrum of the order of 10^{-5} K have been observed. The experiments COBE (1989-1993) [67], WMAP (2001-2010) [68] and Planck (2009 - 2013) [30] have measured the resulting map of the Universe with ever-increasing precision. The CMB angular power spectrum can be explained by acoustic oscillations at the time when photons were emitted. Small density fluctuations led to matter overdensities due to the gravitational potential of dark matter and baryonic matter. Photon pressure resisted the formation of these overdensities, leading to acoustic oscillations of the photon–baryon fluid. The resulting power spectrum, shown in Fig. 1.2, can be fit by the Λ-CDM model consisting of six parameters, amongst others the baryonic and dark matter density, the Hubble constant and the age of the Universe. The latest results of Planck thereby determine the relic density with very high precision.
- **Structure Formation**
  Simulations like the Millennium simulation [69] try to model the formation of stars, galaxies and clusters starting from the CMB. Comparisons of the simulated matter distributions assuming dark matter show a very good agreement with galaxy survey data at large scales. If the Universe was to consist only of ordinary matter, the interaction with photons would have led to a wash-out of the density fluctuations, making it impossible to

form condensed structures. Dark matter, which does not couple to photons, is therefore a crucial ingredient to structure formation. Some tension between simulations and observations arise at smaller scales. For example the number and mass of small satellites in the Milky Way predicted by simulations is larger than what has been observed. Advanced studies that include baryonic physics seem to ameliorate the tension.

- **Supernovae distance measurements**
  Astronomers use so–called type 1a supernovae to determine how fast the Universe is expanding. Measuring luminosity and redshift, they can determine the distances and relative speeds of supernovae to determine the acceleration of the expansion, from which in turn one can determine the ratio of dark energy to matter. Since this information is orthogonal to the measurement of the CMB or the assumption of a flat Universe, this measurement allows one to determine the combined energy density of baryonic and dark matter. After subtracting the visible matter, one therefore obtains a precise estimate of the dark matter content of the Universe.

All this evidence makes a very convincing case for dark matter. Alternative theories like modified Newtonian dynamics [70] try to explain the behavior of galaxy rotation curves and gravitational lensing without a new form of matter by modifying the Einstein equations. However, those theories usually fail to explain the full set of observations that serve as evidence for dark matter. Assuming the existence of dark matter, we know from the listed evidence that its constituents need to be massive, effectively neutral under the electromagnetic force, stable and cold enough to form structures. All criteria are fulfilled by weakly interacting massive particles (WIMPs) [71–75]. By definition they are massive and interact only weakly. WIMPs are by no means the only solution to the dark matter problem. Alternative models like sterile neutrinos [76], axions [77, 78], gravitinos [79], wimpzillas [80], Q-balls [81, 82], SIMPs [83, 84] and many others provide viable solutions.

Recent measurements of the CMB by Planck have determined the dark matter relic density with high precision which adds another constraint to our models. While the correct relic density can in principle be obtained from the mentioned models, the WIMP hypothesis predicts its value naturally (without fine tuning) within the measured value. In the following section we will illustrate this statement, also known as the WIMP miracle, by calculating the relic density from the WIMP annihilation cross section. Since the computation is rather complex we will not be able to cover all details but instead highlight the most important steps. For a more detailed derivation we refer to Reference [85].

3.1.2 The WIMP relic density

Following modern models of the Big Bang, the main steps for creation of matter in the early Universe happen within the first few minutes. The first epoch is inflation at about 10^{-34} s after the Big Bang, followed closely by baryogenesis and electroweak phase transition at $2 \cdot 10^{-11}$ s. As the temperature continues to drop the QCD phase transition takes place after $2 \cdot 10^{-5}$ s. This is roughly the same time when we expect the dark matter to freeze out due to the expansion of

the Universe. In the following couple of minutes we can see the neutrinos decouple (around 1 s), electrons and positrons annihilate (6 s), and finally the formation of light elements via nucleosynthesis. The following processes of recombination will take several thousands of years ending with the decoupling of photons that we can observe today as the cosmic microwave background.

In order to compute the relic density, we have to go back to the first microseconds after the Big Bang when freeze out took place. In the time after inflation, dark matter was in thermal equilibrium, leading to constant number of dark matter particles N_χ,

$$\frac{dN_\chi}{dt} = 0 \ . \tag{3.1}$$

The equilibrium is described by the Boltzmann equation, where any change in the number of dark matter particles comes from annihilation of dark matter into SM particles and vice versa.

$$\frac{dN_\chi}{dt} = \Gamma(f\bar{f} \to \chi\chi) - \Gamma(\chi\chi \to f\bar{f}) + \Gamma_{\text{other}} \tag{3.2}$$

In principle the last term allows for additional interactions since the dark matter candidate could annihilate into different SM particles. However to keep the derivation clear we will limit ourselves to a single $2 \to 2$ process.

We can directly see that when the temperature drops below the mass of the dark matter particle, only SM particles at the tail of the velocity distribution can produce dark matter particles, while the dark matter particles can annihilate into SM particles and thereby decrease N_χ. When the number density of dark matter has dropped sufficiently due to the expansion of the Universe such that the probability of one DM particle to find another is small, the annihilation rate will approach zero and N_χ will become constant again. This process is termed the freeze–out mechanism.

Starting with the left hand side of Eq. (3.2) we have to take into account the expansion of the Universe. A change of the number of dark matter particles can either be related to a change in the number density n_χ or in the volume.

$$\frac{dN_\chi}{dt} = \frac{d(n_\chi V)}{dt} = V\frac{dn_\chi}{dt} + 3n_\chi HV \quad \text{with} \quad H(t) = \frac{\dot{a}(t)}{a(t)} \tag{3.3}$$

The scale factor $a(t)$ origins from the Friedmann-Lemaître-Robertson-Walker (FLRW) metric in general relativity and relates the distance between to objects at a time t to their distance at a reference time t_0. From the time derivative of $a(t)$ one defines the Hubble constant H to quantify the expansion of the Universe.

The transition rates on the right hand side of the Boltzmann equation can be calculated via

$$\Gamma(\chi_1\chi_2 \to f_1\bar{f}_2) = V \int d\Pi(p_1)d\Pi(p_2)d\Pi(k_1)d\Pi(k_2)\phi_{\chi_1}\phi_{\chi_2}(1 \pm \phi_{f_1})(1 \pm \phi_{f_2}) \\ (2\pi)^4\delta^{(4)}(p_1 + p_2 - k_1 - k_2)\overline{|\mathcal{M}_{\chi_{k_1}\chi_{k_2}\to f_{p_1}\bar{f}_{p_2}}|}^2 \tag{3.4}$$

where $d\Pi(p)$ is the phase space integral measure given by

$$d\Pi(p) = \frac{d^3p}{(2\pi)^3 2E(p)}\,. \tag{3.5}$$

ϕ denotes the phase space density of the involved particles. The plus corresponds to bosonic final states and the minus to fermionic final states. $\overline{|\mathcal{M}|}$ is the spin averaged matrix element. Assuming CP invariance we can the fact use that

$$|\mathcal{M}_{\chi_{k_1}\chi_{k_2}\to f_{p_1}\bar{f}_{p_2}}|^2 = |\mathcal{M}_{f_{p_1}\bar{f}_{p_2}\to\chi_{k_1}\chi_{k_2}}|^2 = |\mathcal{M}|^2. \tag{3.6}$$

Moreover we use Maxwell-Boltzmann statistics for all involved particles leading to $\phi_i(k_i) = \exp[-(E_i - \mu_i)/T]$ in equilibrium with a negligible chemical potential μ_i and $1 \pm \phi_i \approx 1$. The full Boltzmann equation then simplifies to

$$\frac{dn_\chi}{dt} + 3n_\chi H = \int d\Pi(p_1)d\Pi(p_2)d\Pi(k_1)d\Pi(k_2)(\phi_{f_1}\phi_{\bar{f}_2} - \phi_{\chi_1}\phi_{\chi_2}) \\ (2\pi)^4\delta^{(4)}(p_1 + p_2 - k_1 - k_2)\overline{|\mathcal{M}|}^2. \tag{3.7}$$

The δ distribution enforces $E_{\chi_1} + E_{\chi_2} = E_{f_1} + E_{\bar{f}_2}$ and we can express the phase space density of the SM particle via

$$\phi_{f_1}\phi_{\bar{f}_2} = \phi_{f_1,eq}\phi_{f_2,eq} = \exp[-(E_{f_1} + E_{\bar{f}_2})/T] \\ = \exp[-(E_{\chi_1} + E_{\chi_2})/T] = \phi_{\chi_1,eq}\phi_{\chi_2,eq}. \tag{3.8}$$

The first equality arises because the SM particle will remain in thermal equilibrium with the rest of the SM sector during the dark matter freeze out. The next step is to connect the decay rate with the annihilation cross section. The thermal average of the cross section times the relative velocity of the annihilating particles is

$$\langle\sigma_{\text{ann}}v_{\text{rel}}\rangle = \frac{1}{n_\chi}\int d\Pi(p_1)d\Pi(p_2)d\Pi(k_1)d\Pi(k_2)(\phi_{f_1}\phi_{f_2} - \phi_{\chi_1}\phi_{\chi_2}) \\ (2\pi)^4\delta^{(4)}(p_1 + p_2 - k_1 - k_2)\overline{|\mathcal{M}|}^2. \tag{3.9}$$

Inserting this expression into the Boltzmann equation we obtain

$$\frac{dn_\chi}{dt} + 3n_\chi H = -\langle\sigma_{\text{ann}}v_{\text{rel}}\rangle(n_\chi^2 - n_{\chi,eq}^2). \tag{3.10}$$

Before we can solve the differential equation we will use two useful replacements. First we define

$$Y = \frac{n}{s} \qquad \text{with } \frac{dY}{dt} = \frac{1}{s}\frac{dn}{dt} + \frac{3}{R}\frac{dR}{dt}Y. \tag{3.11}$$

Here s is the entropy density. We use the fact that the expansion is adiabatic, so that the entropy within a comoving volume element R^3 is conserved $sR^3 = const$. This leads to the first simplification

$$\frac{dY}{dt} = -\langle\sigma_{\text{ann}}v_{\text{rel}}\rangle\, s\,(Y^2 - Y_{eq}^2). \tag{3.12}$$

The second simplification is to replace the time derivative by a derivative with respect to x, a dimensionless quantity related to the temperature. We define

$$x = \frac{m_\chi}{T} \qquad \text{with} \quad \frac{dY}{dt} = \frac{dY}{dx}m_\chi\frac{dT^{-1}}{dt} = \frac{dY}{dx}x\frac{\dot{R}}{R} = \frac{dY}{dx}\frac{H(m)}{x} \tag{3.13}$$

where we use that $T \propto R^{-1}$. For details on the computation of the derivative we refer to Reference [85]. Inserting Eq. (3.13) into Eq. (3.12) yields the final form of the differential equation.

$$\frac{dY}{dx} = -\langle\sigma_{\text{ann}}v_{\text{rel}}\rangle\frac{xs}{H(m)}(Y^2 - Y_{eq}^2). \tag{3.14}$$

We know that around the freeze out temperature the equilibrium density drops exponentially and can therefore be neglected. We can now solve the differential equation by integration.

$$\int_{Y(x_f)}^{Y(\infty)} \frac{1}{Y^2}dY = -\langle\sigma_{\text{ann}}v_{\text{rel}}\rangle\frac{1}{H(m)}\int xs\,dx \tag{3.15}$$

$$-\frac{1}{Y(\infty)} + \frac{1}{Y(x_f)} = -\langle\sigma_{\text{ann}}v_{\text{rel}}\rangle\,\text{const} \tag{3.16}$$

Since the density of dark matter particles is much larger during freeze out than today we can neglect the inverse of $Y(x_f)$. In order to evaluate the integral on the right hand side, we have to consider some arguments on proportionality. We know that sR^3 is constant and R is inversely proportional to the temperature. From Eq. (3.13) then follows that xs must be proportional to m_χ^3/x^2. Integrating over x and further using that $H(m)$ is proportional to m_χ^{-2} yields:

$$Y(\infty) = \frac{\text{const}}{m_\chi\langle\sigma_{\text{ann}}v_{\text{rel}}\rangle} \tag{3.17}$$

Finally we can insert the result for the abundance of the dark matter particle in the relic density [85].

$$\Omega h^2 \equiv \frac{\rho}{\rho_{crit}}h^2 = \frac{m_\chi Y(\infty)s}{\rho_{crit}}h^2 = \frac{\text{const}}{\langle\sigma_{\text{ann}}v_{\text{rel}}\rangle} \approx \frac{2.5\ 10^{-27}\frac{cm^3}{sec}}{\langle\sigma_{\text{ann}}v_{\text{rel}}\rangle} \tag{3.18}$$

We find that the final result is independent from the mass of the dark matter particle and depends only on the annihilation cross section. The Planck collaboration has measured the relic density with high precision to be $\Omega h^2 = 0.120 \pm 0.003$. The observed value can be obtained with a dark matter particle around 100 GeV and a weak coupling of about 0.01. While this coincidence does not constitute evidence that dark matter actually exists at the electroweak scale, it is nevertheless remarkable and often referred to as the WIMP miracle.

3.1.3 The γ-ray excess measured by Fermi–LAT

While the existence of an unknown dark matter as the primary matter component of today's Universe is solidly established, its particle nature remains elusive. A broad experimental program seeks to shed light on this question by searching for dark matter indirectly through the products of its annihilation, directly via scattering with terrestrial targets, or being produced at colliders. Among indirect searches, γ-rays with GeV-range energies are a particularly effective messenger because they propagate unhindered on galactic scales, and thus can be effectively traced back along the direction of their origin. In recent years, the *Fermi* Large Area Telescope (Fermi–LAT) has mapped out the gamma-ray sky with unprecedented resolution, leading to the current best limits on the annihilation cross section for dark matter particles with masses around 100 GeV.

Remarkably, the Fermi–LAT data contain an indication of what appears to be an excess of γ-rays from the direction of the Galactic Center (GC) above the predictions from astrophysical models, with spatial morphology and spectrum consistent with expectations for the annihilation of a thermal relic [86–100].

The Fermi–LAT Collaboration has released its own analysis [16] of this excess based on specialized interstellar emission models (IEMs). These models allow for a determination of the γ-ray fore/background originating from cosmic rays interacting with the interstellar gas and radiation field, and for a separation from the contribution from within roughly 1 kpc along the line of sight of the GC. The GC excess persists in this analysis, and its spectral properties display a strong dependence on the assumed IEM, making it challenging to conclusively identify its origin.

It thus remains unclear whether this signal arises from dark matter annihilation rather than from other, astrophysical sources, such as a population of unresolved millisecond pulsars, cosmic-ray proton or electron outbursts, additional cosmic ray sources, and/or emission from a stellar over-density in the Galactic bulge [99, 101–106]. An interesting development is the use of statistical tools which indicate that the excess displays more clustering than would be expected from Poisson noise from smooth components [107–110]. However, it remains difficult with the current models to disentangle whether this feature represents a property of the excess itself, or un-modeled variation in the background components [111].

Before we can incorporate the results obtained by Fermi–LAT into our analysis we will discuss the details of the experiment.
The Fermi–LAT Collaboration determination of the GC excess is based on the first 62 months of data in a $15^\circ \times 15^\circ$ region in the direction of the GC in the energy range $E_\gamma = 1 \ldots 100$ GeV. In order

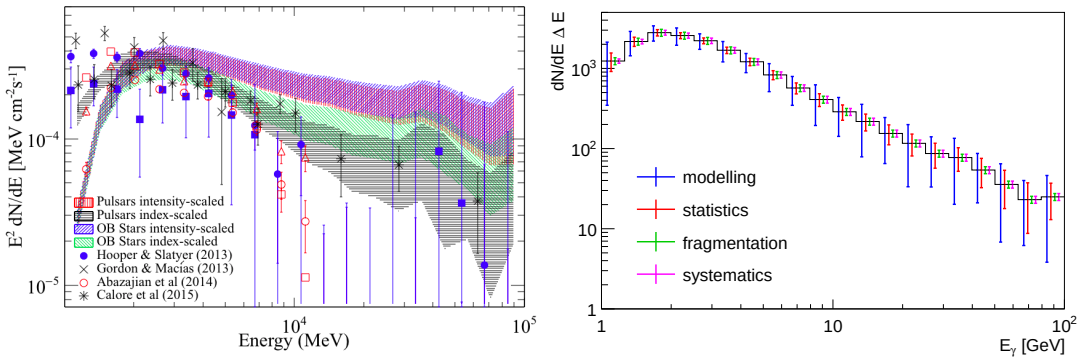

Figure 3.1: Left: Fermi spectrum of the excess after background subtraction as displayed in the publication by Fermi–LAT [16]. The colored bands correspond to different background models. Right: Spectrum averaged over the different backgrounds including uncertainties from the interstellar emission model and fragmentation, as well as instrumental systematics and statistical uncertainties.

to minimize the bias from the data toward the GC, the methodology developed in Reference [16] employs regions outside of the $15° \times 15°$ region for the determination of the fore/background emission. Furthermore, the point sources are determined self-consistently together with each IEM. This is a crucial improvement over previous analyses, as the determination of the point sources in this region is strongly dependent on the IEM. We refer the reader to Reference [16] for a more detailed description of these models and their associated point sources.

In our analysis, we adopt the Fermi–LAT GC excess spectrum for a spectral model assumed to be a power-law function in each of 10 energy bands, equally spaced in logarithmic energy over $E_\gamma = 1 \ldots 100$ GeV, shown in Fig. 3.1. The obtained spectral envelope spans the full set of IEMs and therefore encompasses the interstellar emission modeling uncertainty from Reference [16], uncorrelated bin-by-bin in the energy spectrum. Unlike a correlated global modification, this allows for a more sizable change in the shape of the photon spectrum. The exclusive log-likelihood is flat within the envelope, in harmony with the assumption of theoretical uncertainties in SFitter [18, 37, 38]. This is combined with a profile likelihood this is equivalent to using the RFit scheme [47]. In addition to the modeling uncertainty on the interstellar emission, which is the dominant source of uncertainty, we include the statistical error on the signal rate after background subtraction. The statistical uncertainty thus reflects the combined statistical uncertainty of both the signal and background [18, 37, 38], and it is uncorrelated between bins. Furthermore, we include a 10% uncertainty from the fragmentation function for photons [112, 113], treated as un-correlated between energy bins and Gaussian distributed. Finally, we include the systematic error on the Fermi–LAT effective area [114]. The effective area is the product of the cross-sectional geometrical collection area, the γ-ray

	SM Particle (R=+1)			SUSY Partner (R=-1)		
Names	Gauge ES	Mass ES	Spin	Gauge ES	Mass ES	Spin
squarks	$u_{L/R}, c_{L/R}, t_{L/R}$	u, c, t	1/2	$\tilde{u}_{L/R}, \tilde{c}_{L/R}, \tilde{t}_{L/R}$	$\tilde{u}_{1/2}, \tilde{c}_{1/2}, \tilde{t}_{1/2}$	0
	$d_{L/R}, s_{L/R}, b_{L/R}$	d, s, b	1/2	$\tilde{d}_{L/R}, \tilde{s}_{L/R}, \tilde{b}_{L/R}$	$\tilde{d}_{1/2}, \tilde{s}_{1/2}, \tilde{b}_{1/2}$	0
sleptons	$e_{L/R}, \mu_{L/R}, \tau_{L/R}$	e, μ, τ	1/2	$\tilde{e}_{L/R}, \tilde{\mu}_{L/R}, \tilde{\tau}_{L/R}$	$\tilde{e}_{1/2}, \tilde{\mu}_{1/2}, \tilde{\tau}_{1/2}$	0
	ν_e, ν_μ, ν_τ	ν_e, ν_μ, ν_τ	1/2	$\tilde{\nu}_e, \tilde{\nu}_\mu, \tilde{\nu}_\tau$	$\tilde{\nu}_e, \tilde{\nu}_\mu, \tilde{\nu}_\tau$	0
neutralinos	W^0, B^0	Z^0, γ	1	$\tilde{W}^0, \tilde{B}^0$	$\tilde{\chi}_1^0, \tilde{\chi}_2^0, \tilde{\chi}_3^0, \tilde{\chi}_4^0$	1/2
	H_u^0, H_d^0	h, H, A	0	$\tilde{H}_u^0, \tilde{H}_d^0$		
charginos	$W^\pm$	$W^\pm$	1	$\tilde{W}^\pm$	$\tilde{\chi}_1^\pm, \tilde{\chi}_2^\pm$	1/2
	H_u^+, H_d^-	$H^\pm$	0	$\tilde{H}_u^+, \tilde{H}_d^-$		
gluino	g	g	1	$\tilde{g}$	$\tilde{g}$	1/2

Table 3.1: Overview of SM particles and their supersymmetric partners in the MSSM.

conversion probability, and the efficiency for a γ-ray of a given event selection depending on its energy and direction in the LAT frame. Its uncertainty is treated as fully correlated between bins and also Gaussian distributed.

The primary observable for the GC excess is the annihilation cross section, which characterizes the overall brightness of the excess, and its spectral shape binned in energy. The annihilation cross section itself is fully degenerate with the J-factor, which quantifies the integral of the square of the dark matter density along the line of sight encompassed within the $15^\circ \times 15^\circ$ region employed to extract the signal in Reference [16]. In analogy to the Fermi–LAT analysis we employ a Navarro-Frenk-White (NFW) profile [115]

$$\rho(r) = \frac{\rho_0}{\frac{r}{R_s}^{\gamma} \left(1 + \frac{r}{R_s}\right)^{3-\gamma}} \tag{3.19}$$

for the dark matter density, setting $\gamma = 1.2$, $R_s = 8.5$ kpc, and $\rho_0 = 0.4$ GeV/cm^3. The best estimates for the uncertainty in the J-factor are that it can vary by roughly a factor of two in the region of interest [116].

3.2 SUSY - a model for dark matter

Having established the dark matter problem we will use the supersymmetric models MSSM and NMSSM for our analysis of the GC excess. For this short introduction of the MSSM and the NMSSM we follow the conventions in Reference [21] and [117].

Supersymmetry (SUSY) is one of the most popular models for physics beyond the SM, as it offers a solution to the hierarchy problem and a dark matter candidate. Being the unique

extension of the Poincaré algebra [118], SUSY adds a symmetry transformation Q to the SM that relates fermions and bosons with identical gauge charges.

$$Q\,|\text{Boson}\rangle = |\text{Fermion}\rangle \qquad Q\,|\text{Fermion}\rangle = |\text{Boson}\rangle \tag{3.20}$$

The particle spectrum of supersymmetric models is therefore extended by at least one supersymmetric partner per SM particle. A complete list of particles for the minimal supersymmetric extension of the SM is given in Tab. 3.1. The partners of the SM quarks and leptons are squarks and sleptons. The gauge bosons are associated to gauginos, so called binos, winos and gluinos. In addition to the SUSY partners of the known SM particles we have to introduce an additional Higgs doublet. In the SM, the quarks and leptons receive their masses from the Yukawa terms, requiring both ϕ and $\phi^\dagger$ to appear in the Lagrangian. However, supersymmetric models are defined by their superpotential that is required to be a holomorphic (complex differentiable) function and therefore cannot include a Hermitian conjugate parameter. A supersymmetric model therefore necessarily includes two Higgs doublets with weak hypercharge +/-1/2 to give mass to up-type quarks and down-type quarks and leptons. In comparison to the SM the additional doublet adds a scalar H, a pseudoscalar A and a charged Higgs $H^\pm$. The SUSY partners of the scalar Higgs particles are called Higgsinos. They mix with the gauginos into the neutralino and chargino mass eigenstates. Summing up, the full MSSM spectrum leads to 31 new particles.

3.2.1 The MSSM

In the SUSY formalism, an SM particle and its supersymmetric partner are conveniently combined into one supermultiplet. In order to match the necessary degrees of freedom, a chiral supermultiplet, representing quarks, leptons or Higgs particles, contains a two-component Weyl fermion and a complex scalar field, while a gauge supermultiplet combines a spin-1/2 gaugino and a spin-1 gauge boson. Using supermultiplets we can define the superpotential for the MSSM and NMSSM. The mass spectrum of the model is then derived from the resulting Lagrangian in combination with the corresponding SUSY breaking contributions.

The superpotential of the minimal supersymmetric extension of the Standard Model [21] is given by

$$W_{MSSM} = \mathbf{h_u}\hat{H}_u\hat{Q}\hat{U}_R^C - \mathbf{h_d}\hat{H}_d\hat{Q}\hat{D}_R^C - \mathbf{h_e}\hat{H}_d\hat{L}\hat{E}_R^C + \mu\hat{H}_u\hat{H}_d. \tag{3.21}$$

It contains the Yukawa terms including the mentioned Higgs-supermultiplets $\hat{H}_u$ and $\hat{H}_d$. $\hat{Q}, \hat{U}_R$ and $\hat{D}_R$ denote the chiral supermultiplets for the left and right handed quarks. $\hat{L}$ and $\hat{E}_R^C$ are the supermultiplets of the lepton sector. It is worth noticing that the Yukawa couplings in the MSSM superpotential are identical to the Yukawa couplings in the SM, making the theory at this point highly predictive. So far the μ term contains the only dimensionful parameter of the model. It determines the mass of the Higgsinos and contributes to the mass of the scalar Higgs sector.

The full MSSM Lagrangian contains several parts. From the superpotential we can derive the Yukawa interaction and the Higgsino mass terms by integrating out the superspace coordinates θ and $\bar{\theta}$,

$$\mathcal{L}_{int} = \int d^2\theta W(\Phi) + \int d^2\bar{\theta}\bar{W}(\bar{\Phi}) \ . \tag{3.22}$$

The kinetic terms follow in the same way from the Kähler potential, a polynomial of two superfields. Finally we insert the kinetic terms for gauge bosons and gauginos. Details on the derivation of the Lagrangian in supersymmetric theories can be found in Reference [21]. The resulting Lagrangian contains the full particle spectrum of the MSSM and is invariant under gauge transformations and supersymmetric transformations.

If supersymmetry was actually unbroken, we would expect to observe supersymmetric particles at the same masses as their SM partners. As these particles have not been observed, supersymmetry has to be broken. This forces us to introduce an additional soft SUSY breaking part to the Lagrangian that leaves the couplings unchanged but can push the masses of sfermions, gluinos and charginos to higher values and finally out of the detectable mass range. A general ansatz for this Lagrangian term is [21]

$$\begin{aligned}
\mathcal{L}_{soft}^{MSSM} = & -\frac{1}{2}(M_3\tilde{g}\tilde{g} + M_2\tilde{W}\tilde{W} + M_1\tilde{B}\tilde{B} + c.c.) \\
& - (\tilde{\bar{u}}\mathbf{h_u}\mathbf{A_u}\tilde{Q}H_u + \tilde{\bar{d}}\mathbf{h_d}\mathbf{A_d}\tilde{Q}H_d + \tilde{e}\mathbf{h_e}\mathbf{A_e}\tilde{L}H_d + c.c.) \\
& - \tilde{Q}^\dagger\mathbf{m}_\mathbf{Q}^2\tilde{Q} - \tilde{L}^\dagger\mathbf{m}_\mathbf{L}^2\tilde{L} - \tilde{u}^\dagger\mathbf{m}_\mathbf{\bar{u}}^2\tilde{u}^\dagger - \tilde{\bar{d}}^\dagger\mathbf{m}_\mathbf{\bar{d}}^2\tilde{\bar{d}}^\dagger - \tilde{e}^\dagger\mathbf{m}_\mathbf{\tilde{e}}^2\tilde{e}^\dagger \\
& - m_{H_u}^2 H_u^* H_u - m_{H_d}^2 H_d^* H_d - (m_3^2 H_u H_d + c.c.).
\end{aligned} \tag{3.23}$$

The first line introduces gaugino mass parameters. The bino and wino masses will enter into the neutralino and chargino mass matrices. The trilinear couplings $\mathbf{h_i}\mathbf{A_i}$ correspond to the Yukawa couplings of the superpotential. The squark and slepton mass matrices in the third line are 3×3 matrices in family space. In the decoupling limit they are set to a multi TeV scale. The last line contains soft SUSY breaking contributions to the Higgs potential.

The Higgs sector

Collecting all relevant terms, the scalar potential of the Higgs sector reads

$$\begin{aligned}
V = \quad & (|\mu|^2 + m_{H_u}^2)\left(\left|H_u^{0+}\right|^2 + |H_u^+|^2\right) + (|\mu|^2 + m_{H_d}^2)\left(\left|H_d^0\right|^2 + \left|H_d^-\right|^2\right) \\
& + \left[m_3^2(H_u^+ H_d^- - H_u^0 H_d^0) + c.c.\right] \\
& + \frac{1}{8}(g^2 + g'^2)\left(\left|H_u^0\right|^2 + |H_u^+|^2 - \left|H_d^0\right|^2 - \left|H_d^-\right|^2\right)^2 + \frac{1}{8}g^2\left|H_u^+ H_d^{0*} + H_u^0 H_d^{-*}\right|^2 .
\end{aligned} \tag{3.24}$$

From this potential we can determine the tree–level Higgs masses of the two scalars h and H, the pseudoscalar A and the charged Higgs $H^{\pm}$. Using the minimization conditions $\partial V/\partial H_u^0 = 0$ and $\partial V/\partial H_d^0 = 0$ yields

$$\sin(2\beta) = \frac{2m_3^2}{m_{H_u}^2 + m_{H_d}^2 + 2|\mu|^2} \tag{3.25}$$

$$m_Z^2 = m_{H_u}^2\left(\frac{1}{\cos(2\beta)} - 1\right) - m_{H_d}^2\left(\frac{1}{\cos(2\beta)} + 1\right) - 2|\mu|^2, \tag{3.26}$$

where $\tan\beta$ is defined as the ratio of the vacuum expectation values

$$\tan\beta \equiv \frac{v_u}{v_d} = \frac{\langle H_u^0\rangle}{\langle H_d^0\rangle}. \tag{3.27}$$

Here we have fixed gauge choice and used that the charged components of the Higgs doublets have to vanish at the minimum, since otherwise electromagnetism would be broken. Replacing $m_{H_u}^2$ and $m_{H_d}^2$ in the full scalar potential and expressing the gauge eigenstates in terms of mass eigenstates, the tree–level Higgs masses are given by

$$m_A^2 = \frac{2m_3^2}{\sin(2\beta)} \tag{3.28}$$

$$m_{h,H}^2 = \frac{1}{2}\left(m_A^2 + m_Z^2 \pm \sqrt{(m_A^2 - m_Z^2)^2 + 4m_A^2 m_Z^2 \sin^2(2\beta)}\right) \tag{3.29}$$

$$m_{H^{\pm}}^2 = m_A^2 + m_W^2. \tag{3.30}$$

While m_A^2, m_H^2 and $m_{H^{\pm}}^2$ can become arbitrarily large, the mass of the lightest Higgs is bound to be smaller than the Z boson mass. This is of course contradictory to the measured Higgs mass of 125.1 ± 0.1 GeV. However, loop contributions due to top squarks can be sizable and increase the mass of the lightest Higgs to match the observed value.

The neutralino sector

For our purpose of explaining the relic density we are interested in the MSSM dark matter candidate. The MSSM is often defined to conserve R-parity

$$P_R = (-1)^{3(B-L)+2s}, \tag{3.31}$$

a $\mathbb{Z}_2$ symmetry that protects baryon and lepton number conservation and is motivated for example by the proton lifetime. B is the baryon number that is $+1/3$ for quarks and $-1/3$ for antiquarks. The lepton number L is $+1$ for leptons and -1 for antileptons and s is the spin of the particle. This results in an R-parity of $P_R = +1$ for SM particles and $P_R = -1$ for their supersymmetric partners and as a consequence forbids the decay of SUSY particles into genuine

SM particles. Therefore if R-parity is conserved, the lightest supersymmetric particle (LSP) will be stable. If the LSP was also electromagnetically neutral, it would provide a good dark matter candidate. Valid possibilities are neutralinos, and sneutrinos, or possibly a gravitino, which is not included in our model. A standard sneutrino solution is excluded due to the required annihilation cross section. The minimal required cross section would have led to discovery via Z-boson interactions. The only possibility to find sneutrino solutions is by including sterile sneutrinos [119]. The more popular solution is therefore neutralino dark matter. Its mass is determined by the neutralino mass matrix

$$M_\chi = \begin{pmatrix} M_1 & 0 & -m_Z c_\beta s_w & m_Z s_\beta s_w \\ 0 & M_2 & m_Z c_\beta c_w & -m_Z s_\beta c_w \\ -m_Z c_\beta s_w & m_Z c_\beta c_w & 0 & -\mu \\ m_Z s_\beta s_w & -m_Z s_\beta c_w & -\mu & 0 \end{pmatrix}, \tag{3.32}$$

using the abbreviation $s_\beta = \sin\beta$ and $c_\beta = \cos\beta$. For small M_1 the LSP is bino–like, for small M_2 it becomes a wino and for small μ it becomes a Higgsino mixture. The composition of the LSP is important for its coupling to the gauge bosons and Higgs scalars,

$$g_{Z\chi_i^0\chi_j^0} = \frac{g}{2\cos\theta_w}\left(N_{i3}N_{j3} - N_{i4}N_{j4}\right) \tag{3.33}$$

$$g_{h\chi_i^0\chi_j^0} = \frac{1}{2}\left(g' N_{i1} - g N_{i2}\right)\left(\sin\alpha\ N_{j3} + \cos\alpha\ N_{j4}\right) + (i \leftrightarrow j) \tag{3.34}$$

$$g_{A\chi_i^0\chi_j^0} = \frac{1}{2}\left(g' N_{i1} - g N_{i2}\right)\left(\sin\beta\ N_{j3} - \cos\beta\ N_{j4}\right) + (i \leftrightarrow j) \tag{3.35}$$

$$g_{W\chi_i^\pm\chi_j^0} = \frac{g\sin\theta_w}{\cos\theta_w}\left(\frac{1}{\sqrt{2}}N_{j4}V_{i2}^* - N_{j2}V_{i1}^*\right). \tag{3.36}$$

The mixture of each neutralino is given by the neutralino mixing matrix N_{ij}. The first index indicates the mass eigenstate while the second index refers to the bino, wino or Higgsino admixture, respectively. V_{ij} is the equivalent matrix for the chargino sector. We see that apart from the W-coupling all couplings require a Higgsino component of at least one of the neutralinos. Therefore smaller values of μ will usually lead to larger couplings of the LSP. On the other hand μ always has to remain larger than 103 GeV, otherwise the mass of the lightest chargino would be less than 103 GeV and thus be excluded by LEP searches [120–128].

3.2.2 The NMSSM

The simplest extension of the MSSM is the next-to-minimal supersymmetric Standard Model, which includes an additional chiral superfield $\hat{S}$, which is a singlet under the gauge groups. The main motivation for the NMSSM is the μ problem in the MSSM. The μ term introduces the only mass scale in the superpotential and as a SUSY-respecting parameter it is expected to be around the Planck scale as a natural cutoff scale. However it has to cancel with the soft SUSY breaking terms $m_{H_u}^2$ and $m_{H_u}^2$ in Eq. 3.26 which are expected to be at the SUSY breaking scale around a

few TeV. The tension between these scales can be resolved in the NMSSM. The superpotential of the NMSSM [21, 117, 129–133] including the additional singlet superfield $\hat{S}$ and associated terms is given by

$$W_{\text{NMSSM}} = W_{\text{MSSM}} + \lambda \hat{S}\hat{H}_u\hat{H}_d + \xi_F\hat{S} + \frac{\mu'}{2}\hat{S}^2 + \frac{\kappa}{3}\hat{S}^3 \,, \tag{3.37}$$

where λ and κ are dimensionless couplings that couple the singlet to itself and to the Higgs bosons. When the singlet acquires a vacuum expectation value v_s, the Higgs–singlet mixing introduces an effective μ term $\mu_{\text{eff}} = \lambda v_s$ that is now determined by the vacuum expectation value of the singlet. The quadratic term proportional to μ' is the supersymmetric mass term for the singlet, comparable to the μ term for the MSSM Higgs bosons. Assuming a global supersymmetry the tadpole term proportional to ξ_F can be removed though a constant shift of the singlet field. Finally, with the help of an ad-hoc $\mathbb{Z}_3$-symmetry we can make the superpotential scale invariant and set the one remaining dimensionful parameter, μ', to zero.

The extended superpotential in Eq. (3.37) in terms of the superfield $\hat{S}$ can be translated into additional soft-SUSY-breaking terms for the physical singlet field S [21, 117, 129],

$$-\mathcal{L}_{\text{soft}}^{\text{NMSSM}} = m_S^2\,|S|^2 + \left(\lambda A_\lambda H_u H_d S + \xi_S S + \frac{m_S'^2}{2}S^2 + \frac{\kappa}{3}A_\kappa S^3 + \text{h.c.}\right) . \tag{3.38}$$

A_λ and A_κ have mass dimension one and fix the scale of the Lagrangian, while λ and κ defined in Eq. (3.37) are complex numbers. An alternative parametrization of the same Lagrangian uses the mass terms $m_3^2 = B\mu$ and $m_S'^2 = B'\mu'$ to emphasize the connection to the superpotential. In order to be consistent with the $\mathbb{Z}_3$-symmetry of the superpotential we also eliminate the corresponding SUSY-breaking terms by setting $m_3^2 = m_S'^2 = \xi_S = 0$. In the presence of the effective μ term we can neglect the original μ parameter, eliminating all scales in the superpotential. Correspondingly, μ will in the following indicate the effective μ term. The relevant NMSSM Lagrangian now reads

$$-\mathcal{L}_{\text{soft}}^{\text{NMSSM}} = m_S^2\,|S|^2 + \left(\lambda A_\lambda H_u H_d S + \frac{\kappa}{3}A_\kappa S^3 + \text{h.c.}\right) . \tag{3.39}$$

In the MSSM, the minimization conditions of the Higgs potential can be used to replace $m_{H_u}^2$ and $m_{H_d}^2$ by m_Z and $\tan\beta$ in the broken phase. Using the additional minimization condition of the NMSSM m_S^2 can be expressed in terms of μ. The Higgs–singlet sector [134–141] is therefore fully described by the parameters $\lambda, \kappa, A_\lambda, A_\kappa, \mu, \tan\beta$, and the mass of the Z boson.

For specific NMSSM models we have to define the input scale of these parameters. The ratio of the VEVs $\tan\beta$ is always evaluated at the weak scale m_Z, because it assumes electroweak symmetry breaking. For the low-scale models in Sec. 5.2.1 all supersymmetric parameters

including $\lambda, \kappa, A_\lambda, A_\kappa, \mu$, the squark and slepton masses, etc. are set at the SUSY scale. For the high-scale models discussed in Sec. 5.3 λ, κ and μ are set at the SUSY scale of 1 TeV, while A_λ and A_κ can either be unified to A_0 at the GUT scale or set individually (also at the GUT scale).

Higgs–singlet–singlino sector

Compared to the Higgs sector of the MSSM, the phenomenology of the NMSSM is strongly modified by the additional supermultiplet, consisting of a scalar and a pseudoscalar Higgs boson and a fifth neutralino. While in general the mass of the singlet states is a free parameter, we will assume that the singlino contributes to a light LSP and that the singlet Higgs states are therefore lighter than their SM-like counterparts. For example, the SM-like Higgs boson h with its mass of 125 GeV will typically be the second-lightest CP-even Higgs scalar. For a scale-invariant superpotential we can write out the symmetric Higgs mass matrix [130, 131, 142–149] in the (H, h, S)-basis, where h is the SM-like Higgs boson,

$$M^2_{H,h,S} = m_Z^2 \begin{pmatrix} s^2_{2\beta}\delta + \dfrac{2\mu}{s_{2\beta} m_Z^2}(A_\lambda + \tilde{\kappa}\mu) & c_{2\beta}s_{2\beta}\delta & -c_{2\beta}\dfrac{\lambda}{g m_Z}(A_\lambda + \tilde{\kappa}\mu) \\ \cdot & c^2_{2\beta} + s^2_{2\beta}\dfrac{\lambda^2}{g^2} & \dfrac{2\lambda}{g m_Z}\left(\mu - s_{2\beta}\dfrac{A_\lambda}{2} - s_{2\beta}\tilde{\kappa}\mu\right) \\ \cdot & \cdot & s_{2\beta}\dfrac{\lambda^2 A_\lambda}{2g^2\mu} + \dfrac{\tilde{\kappa}\mu}{m_Z^2}(A_\kappa + 4\tilde{\kappa}\mu) \end{pmatrix}, \tag{3.40}$$

using the abbreviation $\delta = 1 - \frac{\lambda^2}{g^2}$. In terms of the ordered mass eigenstates $H_2 \equiv h$ means that throughout the NMSSM analysis we identify the second-lightest Higgs with the observed SM-like state. Instead of κ and λ, the modified parameter set

$$\begin{aligned} \tilde{\kappa} &= \frac{\kappa}{\lambda} \quad \text{(singlet mass parameter)} \\ \frac{\lambda}{g} &\quad \text{(singlet decoupling parameter)} \end{aligned} \tag{3.41}$$

appears in the diagonal entries for the light and heavy MSSM-like Higgs states. In the following, we replace κ with $\tilde{\kappa}$ but keep λ instead of trivially rescaling it by a constant g. At tree–level level the two NMSSM parameters take the pressure off the stop sector for small values of $\tan\beta$. In our basis conventions the second Higgs state is the observed SM-like resonance. This means we can decouple the singlet contributions from the observed Higgs. Setting

$$A_\lambda = 2\mu\left(\frac{1}{s_{2\beta}} - \tilde{\kappa}\right) \tag{3.42}$$

at the SUSY scale removes the (2,3) entry from the mass matrix and therefore decouples the singlet sector from the SM-like Higgs boson h^0. Note that this condition does not require any of

the couplings in the NMSSM potential of Eq. (3.39) to vanish.

More generally, we can decouple the singlet from all other Higgs states in the limit $\lambda \ll g < 1$. This way the two corresponding entries in the extended Higgs mass matrix vanish. To make the singlet itself heavy we need to increase its entry in the mass matrix in the limit $\lambda \ll g$. Neglecting A_κ, the singlet entry in the Higgs mass matrix is $(2\tilde{\kappa}\mu)^2$, which for finite κ consistently decouples with the single condition $\lambda \ll 1$.

Aside from the extra CP-even Higgs, the singlet extensions of the MSSM Higgs sector adds an additional pseudoscalar. We can transform the weak eigenbasis-basis (H_u, H_d, S) into a mass basis (A, S) by a rotation and by removing the Goldstone boson, so that $A = c_\beta H_u + s_\beta H_d$. For large values of $\tan\beta$ the mass eigenstate A is approximately given by H_d. Removing the Goldstone modes, the 3×3 mass matrix in terms of the weak eigenstates can be reduced to a 2×2 mass matrix in the basis (A, S), which reads

$$M^2_{A,S} = m_Z^2 \begin{pmatrix} \dfrac{2\mu\,(A_\lambda + \tilde{\kappa}\mu)}{s_{2\beta} m_Z^2} & \dfrac{\lambda}{g m_Z}\,(A_\lambda - 2\tilde{\kappa}\mu) \\ \cdot & s_{2\beta}\dfrac{\lambda^2}{g^2}\left(\dfrac{A_\lambda}{2\mu} + 2\tilde{\kappa}\right) - 3\tilde{\kappa}\dfrac{\mu A_\kappa}{m_Z^2} \end{pmatrix} \simeq m_Z^2 \begin{pmatrix} \dfrac{4\mu^2}{s_{2\beta}^2 m_Z^2} & 2\dfrac{\lambda}{g m_Z}\dfrac{\mu}{s_{2\beta}} \\ \cdot & \dfrac{\lambda^2}{g^2} - 3\tilde{\kappa}\dfrac{\mu A_\kappa}{m_Z^2} \end{pmatrix}. \tag{3.43}$$

The pseudoscalar mass eigenstates are denoted as A_1 and A_2. In the second form we use the singlet decoupling condition Eq. (3.42) and assume $s_{2\beta} \ll 1$. As for the scalar sector, the limit $\lambda \ll g$ decouples the singlet; its squared mass is then given by $-3\tilde{\kappa}\mu A_\kappa$. The upper left entry of the matrix then corresponds to the MSSM pseudoscalar mass, $m_A^2 = 2\mu\,(A_\lambda + \tilde{\kappa}\mu)\,/s_{2\beta}$. This way we can choose either this MSSM-like mass or A_λ as an input parameter. Similarly, we can replace A_κ with the lower-right entry in $M^2_{A,S}$ as the input parameter.

Finally, the supersymmetric partner of the singlet field, the singlino, appears in the neutralino mass matrix,

$$M_{\tilde{\chi}} = \begin{pmatrix} M_1 & 0 & -m_Z c_\beta s_w & m_Z s_\beta s_w & 0 \\ 0 & M_2 & m_Z c_\beta c_w & -m_Z s_\beta c_w & 0 \\ -m_Z c_\beta s_w & m_Z c_\beta c_w & 0 & -\mu & -m_Z s_\beta \dfrac{\lambda}{g} \\ m_Z s_\beta s_w & -m_Z s_\beta c_w & -\mu & 0 & -m_Z c_\beta \dfrac{\lambda}{g} \\ 0 & 0 & -m_Z s_\beta \dfrac{\lambda}{g} & -m_Z c_\beta \dfrac{\lambda}{g} & 2\tilde{\kappa}\mu \end{pmatrix}. \tag{3.44}$$

The bottom-right entry indicates that in accordance with Eq. (3.41) the combination $2\tilde{\kappa}\mu$ determines the singlino mass. The gauginos do not mix with the singlino. To altogether decouple

the singlino, we have to remove the singlino–Higgsino mixing via $\lambda \ll 1$ and at the same time make the singlino heavy, $\tilde{\kappa} \gg 1$. In contrast, for $\tilde{\kappa} < 1/2$ the LSP will be mostly singlino. In this case the LSP mass $m_{\tilde{\chi}}$ is approximately given by the solution to

$$\begin{aligned} 2\tilde{\kappa}\mu &= m_{\tilde{\chi}} - m_Z^2 \frac{\lambda^2}{g^2} \frac{m_{\tilde{\chi}} - \mu s_{2\beta}}{m_{\tilde{\chi}}^2 - \mu^2} \\ \Leftrightarrow \qquad m_{\tilde{\chi}} &\simeq 2\tilde{\kappa}\mu + \frac{\lambda^2}{g^2} \frac{m_Z^2}{\mu} \frac{2\tilde{\kappa} - s_{2\beta}}{4\tilde{\kappa}^2 - 1} , \end{aligned} \tag{3.45}$$

so that the LSP mass can be fixed by adjusting $\tilde{\kappa}$.

For the interpretation of the galactic center excess a light pseudoscalar will be crucial. To describe its relevant couplings we have to rely on the different mixing matrices. The neutralino mass matrix will be rotated into its mass eigenstates through a matrix (N_{ij}) with $i, j = 1...5$. To rotate the pseudoscalar mass matrix into its mass eigenstates we also have to consider the Goldstone mode. The corresponding mixing matrix is (P_{ij}) with $i = 1, 2$ and $j = 1, 2, 3$ because the Goldstone is not counted as part of the mass eigenstates $A_{1,2}$. The lighter pseudoscalar Yukawa coupling to bottom quarks is given by

$$g_{A_1 bb} = \frac{m_b}{\sqrt{2} v c_\beta} P_{11} \qquad \text{with} \quad P_{11} \approx -s_\beta^2 c_\beta \frac{\lambda v}{\mu} P_{13} , \tag{3.46}$$

where P_{11} is the H_d component of the lightest mass eigenstate and in the second relation we assume $m_A \gg m_{A_1}$. Because the factor c_β cancels, there will be no enhancement at large $\tan\beta$. The coupling mediating the light pseudoscalar decay into the lightest neutralino is given by

$$\begin{aligned} g_{A_1 \tilde{\chi}\tilde{\chi}} =& \lambda\sqrt{2} \left(P_{11}N_{14}N_{15} + P_{12}N_{13}N_{15} + P_{13}N_{13}N_{14}\right) - \lambda\tilde{\kappa}\sqrt{2} P_{13} N_{15}^2 \\ & - \left(g_1 N_{11} - g_2 N_{12}\right) \left(P_{11}N_{13} - P_{12}N_{14}\right) . \end{aligned} \tag{3.47}$$

When we assign the second Higgs to be SM-like, the lightest pseudoscalar will be mainly singlet. Therefore the coupling simplifies to

$$g_{A_1 \tilde{\chi}\tilde{\chi}} = \lambda\sqrt{2} \left(N_{13}N_{14} - \tilde{\kappa} N_{15}^2\right) , \tag{3.48}$$

where we set $P_{11} = P_{12} \ll P_{13} \simeq 1$. As N_{13} and N_{14} differ in sign, both contributions will add up. For a singlino LSP we have sizable $N_{15} \to 1$, but following Eq. (3.45) $\tilde{\kappa}$ ranges around $m_{\tilde{\chi}}/(2\mu)$. This means that the singlino term in $g_{A_1 \tilde{\chi}\tilde{\chi}}$ decreases with increasing μ, but the same is true for the Higgsino fractions N_{13} and N_{14}. Altogether, a large mediator coupling to the LSP points to a singlino LSP. For the scalar Higgs sector the coupling is completely equivalent to the pseudoscalar expression, replacing only P_{ai} by S_{ai} that rotates the weak Higgs basis into the mass basis.

$$\begin{aligned} g_{H_i \tilde{\chi}\tilde{\chi}} = i \Big[& \lambda\sqrt{2} \left(S_{i1}N_{14}N_{15} + S_{i2}N_{13}N_{15} + S_{i3}N_{13}N_{14}\right) - \lambda\tilde{\kappa}\sqrt{2} S_{i3} N_{15}^2 \\ & - \left(g_1 N_{11} - g_2 N_{12}\right) \left(S_{i1}N_{13} - S_{i2}N_{14}\right) \Big] \end{aligned} \tag{3.49}$$

Otherwise the coupling only differs by an overall complex phase i. The coupling of the LSP to the Z boson remains the same as for the MSSM, because the additional singlino couples only to the Higgs.

High-Scale NMSSM

Instead of using the full set of TeV-scale model parameters we can require the NMSSM to fulfill a set of unification assumptions at large energy scales. We start with a unified squark and slepton mass m_0, a unified gaugino mass $m_{1/2}$, and a unified trilinear coupling A_0 at the GUT scale [150–154]. Furthermore, we require a $\mathbb{Z}_3$ symmetry to remove for example the μ term and replace it with an effective μ term induced by the singlet VEV. Because we do not require unified Higgs masses $m_{H_u}^2$, $m_{H_d}^2$, and m_S^2 we refer to the model as the NUH-NMSSM (non-universal Higgs masses) [155].

From the analysis of the Higgs and neutralino sectors we know that to produce a light scalar and a light pseudoscalar, $\tilde{\kappa}$ has to be small and A_κ evaluated at 10 TeV has to range around the electroweak scale. The running of the different model parameters from the GUT scale to the weak scale is described by renormalization group equations, for example the singlet couplings are [117]

$$\begin{aligned}
16\pi^2 \frac{d\lambda}{d\log Q^2} &= \frac{\lambda}{2}\left(4\lambda^2 + 3h_t^2 + 3h_b^2 + h_\tau^2 + 2\kappa^2 - g_1^2 - 3g_2^2\right) \\
16\pi^2 \frac{d\kappa}{d\log Q^2} &= \frac{\kappa}{2}\left(6\lambda^2 + 6\kappa^2\right) \\
16\pi^2 \frac{d\tilde{\kappa}}{d\log Q^2} &= \frac{\tilde{\kappa}}{2}\left(4\tilde{\kappa}^2\lambda^2 + 2\lambda^2 - 3h_t^2 - 3h_b^2 - h_\tau^2 + g_1^2 + 3g_2^2\right) \ .
\end{aligned} \tag{3.50}$$

The Yukawa couplings are defined as $m_f = h_f v \sin\beta/\sqrt{2}$. The couplings κ and λ appear squared, so that for a choice of signs our argument will hold for their absolute values. If we neglect the gauge couplings, λ increases with Q and runs into a Landau pole. If we also neglect the Yukawa couplings, which accelerate this increase, the Landau pole is approximately given by

$$\lambda(Q) = \lambda_0 \left[1 - \frac{\lambda_0^2}{2\pi^2}\log\frac{Q}{Q_0}\right]^{-1/2} \to \infty \ . \tag{3.51}$$

For our theory to be valid up to $Q = 10^{16}$ GeV the Higgs–singlet coupling is limited to $\lambda_0 < 0.81$ at $Q_0 = 1$ TeV. The large and also increasing top Yukawa coupling further accelerates the approach of a strongly interacting regime, requiring $\lambda_0 \lesssim 0.5 \ldots 0.6$ for a valid theory to the GUT scale. Assuming roughly constant λ and also ignoring the Standard Model Yukawa and gauge couplings, the running singlet self-coupling κ is given by

$$\kappa(Q) = \kappa_0 \left[1 + \frac{\kappa_0^2}{\lambda^2}\left(1 - \left(\frac{Q}{Q_0}\right)^{\frac{3\lambda^2}{4\pi^2}}\right)\right]^{-1/2} \left(\frac{Q}{Q_0}\right)^{\frac{3\lambda^2}{8\pi^2}} \ . \tag{3.52}$$

The maximum value of κ_0 for which the theory is defined up to $Q = 10^{16}$ GeV ranges around

$$\kappa_{\max} = \frac{\lambda}{\sqrt{\left(\frac{Q}{Q_0}\right)^{\frac{3\lambda^2}{4\pi^2}} - 1}} = \begin{cases} 0.66 & \text{for } \lambda \to 0 \\ 0.53 & \text{for } \lambda = 0.6\ . \end{cases} \tag{3.53}$$

In this approximation we can compute a few example values by iterating: starting with $\lambda_0 = 0.3 = \kappa_0$ at the TeV scale we find $\kappa = 0.43$ and $\lambda = 0.61$ at 10^{16} GeV. The singlet mass parameter $\tilde{\kappa}$ decreases from 1.0 to 0.7.

In the running of $\tilde{\kappa}$ the top Yukawa coupling enters with a negative sign. Therefore κ increases slower with the scale than λ as long as $\kappa, \lambda \ll h_t$. If we consider larger values for the weak-scale starting points, κ increases faster than λ. $\lambda = 0.45 = \kappa_0$ gives $\kappa = 1.7$ and $\lambda = 1.2$ at the GUT scale, so $\tilde{\kappa}$ increases from 1.0 to 1.4.

For both components, the Higgs–singlet coupling and the singlet self-coupling come with associated mass scales. They run like

$$\begin{aligned} 16\pi^2 \frac{dA_\lambda}{d\log Q^2} &= 4\lambda^2 A_\lambda + 3h_t^2 A_t + 3h_b^2 A_b + h_\tau^2 A_\tau + 2\kappa^2 A_\kappa + g_1^2 M_1 + 3g_2^2 M_2 \\ 16\pi^2 \frac{dA_\kappa}{d\log Q^2} &= 6\lambda^2 \left(\tilde{\kappa}^2 A_\kappa + A_\lambda\right) \\ 16\pi^2 \frac{dm_S^2}{d\log Q^2} &= 2\lambda^2 \left(m_{H_u}^2 + m_{H_d}^2 + m_S^2 + {A_\lambda}^2 + 3\tilde{\kappa}^2 m_S^2 + \tilde{\kappa}^2 {A_\kappa}^2\right) \end{aligned} \tag{3.54}$$

The increase of these mass scales towards high energy scales clearly does not help with the appearance of a strongly interacting Higgs–singlet sector in the NMSSM.

Finally, we can ask how the new NMSSM Higgs–singlet parameters affect the running of the MSSM-like parameters. An interesting parameter in the MSSM is the stop mixing parameter, which now runs like

$$16\pi^2 \frac{dA_t}{d\log Q^2} = 6h_t^2 A_t + h_b^2 A_b + \lambda^2 A_\lambda + \frac{13}{9} g_1^2 M_1 + 3g_2^2 M_2 + \frac{16}{3} g_3^2 M_3 \tag{3.55}$$

While there will be an effect from the additional singlet on the running of the MSSM-like parameters, its impact will be numerically small. The only exception appears when we allow the Higgs–singlet sector to become strongly interacting at relatively low scales, in which case for example the stop mixing parameter will also sharply increase.

Having established the mass spectrum, couplings and necessary scale dependencies for further discussion, we will now set the phenomenology of the SUSY models into context with dark matter constraints.

3.3 Dark matter annihilation channels in supersymmetric models

For any SUSY fit the relic density is a key constraint shaping the likelihood map of supersymmetric models. For a typical weakly interacting dark matter candidate comprising all of the dark matter and following a standard cosmological history, the thermal relic abundance is determined by the dark matter annihilation cross section. Following our calculation in Sec. 3.1.2, the relic density is roughly given by the inverse of the velocity averaged annihilation cross section $\langle \sigma v \rangle$. The same annihilation cross section also fixes the GC excess up to the difference in the velocity distribution between the early Universe and today.

However, in a theory containing multiple components of dark matter and/or a nonstandard cosmology, the relic abundance and the annihilation cross section are less correlated. For this reason, we remain somewhat agnostic as to whether the dark matter abundance arises from the usual freeze-out calculation. In Chapter 4 and 5 we will therefore first indicate the best fit regions for the GC excess and the relic density separately, before we perform a combined fit of the GC excess and the relic abundance assuming a standard cosmological history.

Our SUSY parameter analysis can be most easily organized in terms of the dominant dark matter annihilation channels. The main annihilation channels can be sorted into the categories s-channel, t-channel and co-annihilation as illustrated in Fig. 3.2 and Fig. 3.3. While the measured relic density can be realized with all three channels, it is generally difficult to realize large enough cross sections to explain the GC excess [39, 156–161] for an LSP with a suitable mass. For example, t-channel annihilation channels are generally not very efficient and decouple rapidly with the mediator mass [6].

In the SUSY framework, the lightest neutralino provides an excellent dark matter candidate. Its properties are largely determined by the wino mass M_2, the Higgsino mass parameter μ, and the bino mass M_1. For the NMSSM the additional parameter $\tilde{\kappa}$ determines the singlino content of the LSP. As we will see below, the masses of the heavy Higgs states $m_{A,H}$ can play an important role for dark matter annihilation. Again for the NMSSM the singlet scalar and pseudoscalar particles offer additional annihilation channels via light singlet–like mediators. The mass of the SM like Higgs m_h has to match the measured value of 126 GeV and is adjusted with the help of $\tan\beta$, A_t and the stop mass.

The remaining squark masses, together with the sleptons and gluinos are assumed to decouple, as suggested by the direct limits from the null results of LHC searches. Moreover we require the lightest chargino to be heavier than the LEP limit of 103 GeV for all scenarios [120–128].

s-channel

The most efficient annihilation channel is usually s-channel annihilation. Two dark matter particles annihilate via a boson ($h/H/A/Z$) into SM particles. If the propagator can be on-shell, the annihilation cross section becomes very large and is only constrained by the width

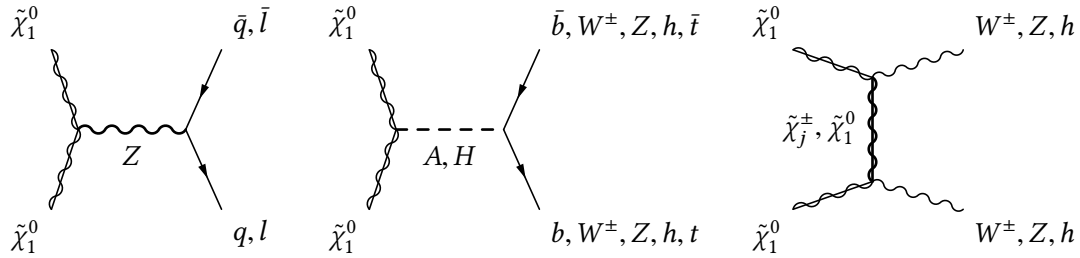

Figure 3.2: Feynman diagrams illustrating dark matter annihilation $\tilde{\chi}_1^0\tilde{\chi}_1^0 \to b\bar{b}, WW, ZZ, hh, t\bar{t}$ for s-channel and t-channel processes.

of the propagator. In table 3.2 we display the annihilation cross section multiplied by the relative velocity of the colliding particles for specific channels. The results are expanded in powers of v^2 and assume Majorana dark matter and light quarks as final states so that $m_q \ll m_\chi$.

Candidates for s-channel mediators in the MSSM and NMSSM are:

- Z-funnel annihilation
  The (N)MSSM neutralino is a Majorana particle that couples to the axial vector component of the Z boson. The interaction in Eq. (3.33) is proportional to the Higgsino component of the LSP. The coupling vanishes in the limit $\tan\beta \to 1$, due to approximately equal Higgsino fractions. Another reason to consider large $\tan\beta$ is the reduction of the predicted spin-independent direct detection cross section, which allows for a larger parameter space [162]. From table 3.2 we see that the v-independent contribution is suppressed by the light mass of the outgoing quarks and leptons. Close to the on–shell condition, the v^2 suppressed term will therefore be dominant. Because of the velocity dependence of the annihilation rate $\langle\sigma v\rangle$ this channel usually prefers LSP masses slightly above or below 45 GeV, because directly on the Z pole the annihilation is too efficient. Finally the velocity suppression of the annihilation process today compared to the time of freeze out makes it impossible to fit the relic density and the GC excess simultaneously without further contributions from other channels.
- Scalar h-funnel annihilation
  For the annihilation via the SM Higgs, the LSP mass should be around $m_{\tilde{\chi}_1^0} = 63$ GeV, slightly away from the resonance. However, in combination with other annihilation channels the h-funnel can give the largest contribution already for LSP masses around 55 GeV. The neutralino coupling to the Higgs in Eq. (3.34) relies on Higgsino-gaugino mixing, which will also be relevant for potential invisible Higgs decays. Aside from a potential invisible branching ratio of the Higgs, almost the entire neutralino annihilation rate through the light Higgs funnel goes to $b\bar{b}$, with small contributions or $\tau^+\tau^-$ and WW. Like for the Z-mediated process, the h-funnel is velocity suppressed which makes it difficult to generate a large annihilation cross section exclusively via the Higgs in the GC.

Process	Channel	σv
$\chi\chi \to A \to q\bar{q}$	s-channel	$\frac{3\lambda_{\chi A}^2 \lambda_{qA}^2}{2\pi} \frac{m_\chi^2}{(M_A^2 - 4m_\chi^2)^2}$
$\chi\chi \to h \to q\bar{q}$	s-channel	$\frac{3\lambda_{\chi h}^2 \lambda_{qh}^2}{8\pi} \frac{v^2 m_\chi^2}{(M_h^2 - 4m_\chi^2)^2}$
$\chi\chi \to Z \to q\bar{q}$	s-channel	$\frac{3\lambda_{\chi Z_{ax}}^2}{2\pi} \left[\frac{\lambda_{qZ_{ax}}^2 m_q^2}{M_Z^4} + \frac{v^2(\lambda_{qZ_{ax}}^2 + \lambda_{qZ_v}^2) m_\chi^2}{3(M_Z^2 - 4m_\chi^2)^2} \right]$
$\chi\chi \to \chi\tilde{q}\bar{q} \to q\bar{q}$	t-channel	$\frac{3\lambda_{\chi q\tilde{q}}^4 (m_q + m_\chi)^2}{8\pi (M_{\tilde{q}}^2 - m_q^2 + m_\chi^2)^2}$

Table 3.2: Some examples for simplified annihilation cross sections expanded in powers of v^2 assuming Majorana dark matter and light final states [163].

However due to the small widths, very fine tuned solutions exist as we will demonstrate in Sec. 4.1.

Aside from the SM–like Higgs, the MSSM scalar H and the singlet scalar S can serve as a mediator for dark matter annihilation. The general statements for scalar mediated processes apply of course as well in this case. The main difference is the nature of the final state particles, which depends on the mass of the scalar. The singlet–like scalar coupling to the neutralino also receives additional contributions, given by Eq. (3.49).

- Pseudoscalar A-funnel annihilation
  In contrast to the scalar Higgs funnel, the annihilation via a pseudoscalar A is not p-wave suppressed, leading to larger cross sections. This is crucial since the velocity average does not drop with temperature, making it easier to fit the relic density together with the GC excess. The coupling to the LSP is again driven by Higgsino-gaugino mixing. In the final state, heavy pseudoscalar decays to down-type fermions are enhanced by $\tan\beta$, which implies that for $\tan\beta \gtrsim 30$ the resonance pole structure of the A-funnel gets significantly washed out and a $b\bar{b}$ final state appears from this topology.

  In the NMSSM, we have an additional singlet pseudoscalar channel. If the pseudoscalar is mainly singlet, the relevant contributions to the neutralino coupling are given by Eq. (3.48). Large Higgsino and singlino components therefore lead to a strong coupling.

t-channel

Two dark matter particles can as well annihilate via a supersymmetric mediator like a neutralino, a chargino, or a sfermion in the t-channel. In this case the propagator can not be on–shell, since the dark matter mass is always heavier than the final state quark, making the denominator in Tab. 3.2 positive. The resulting cross sections are hence in general smaller than for on-shell s-channel annihilations. Large enough annihilation cross sections still occur for:

- t-channel chargino exchange
  The chargino mediated t-channel is driven by the coupling to W-bosons $g_{W\tilde{\chi}_1^0\tilde{\chi}_1^+}$ in the final state given by Eq. (3.36). A substantial coupling to W bosons requires that the LSP and the light chargino contain either a sizable wino or Higgsino fraction. Due to the chargino mass in the propagator, the annihilation is most efficient for charginos just above the LEP limit $m_{\tilde{\chi}_1^+} = 103$ GeV.
- t-channel neutralino exchange
  Annihilation via a neutralino results in two final states $\tilde{\chi}_1^0\tilde{\chi}_1^0 \to ZZ$ or $\tilde{\chi}_1^0\tilde{\chi}_1^0 \to hh$ [100]. For the former, the relevant coupling is the axial-vector coupling $g_{Z\tilde{\chi}_1^0\tilde{\chi}_i^0}$ driven by the Higgsino content. For the latter process, the relevant couplings $g_{h\tilde{\chi}_1^0\tilde{\chi}_i^0}$ are products of Higgsino and gaugino fractions, requiring that the LSP be a highly mixed state,
- t-channel sfermion exchange, e. g. via tau sleptons
  In this case, a significant coupling requires a large wino fraction, which typically leads to excessively large annihilation rates into W bosons for LSP masses below around 1 TeV. Since we decouple the squark and slepton sector, this channel will be irrelevant for our analysis.

Co-annihilation

If the mass difference between LSP and the next–heaviest supersymmetric particle is smaller than about 10%, the decay of the heavier particle is suppressed such that a significant number of the next–to–lightest–particle has not yet decayed at the time of freeze–out and it can contribute to the annihilation of dark matter. Typical examples are stau [164, 165], stop [166] or chargino

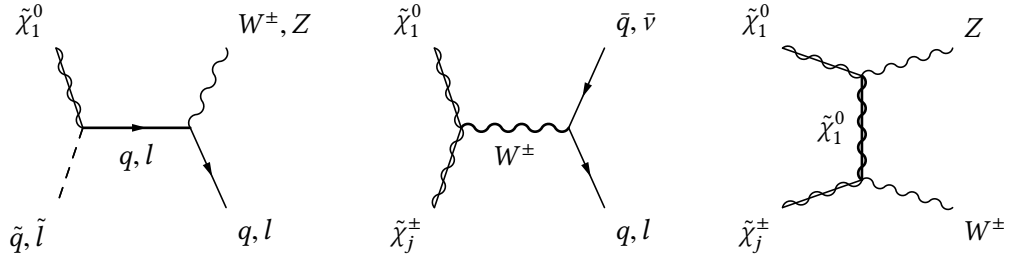

Figure 3.3: Feynman diagrams illustrating dark matter co-annihilation processes with squarks, sleptons and charginos.

co-annihilation [167, 168]. The corresponding mediator particles are tau, top and the charged Higgs and W bosons.

For the light dark matter particles, usually associated with the Fermi–LAT GC excess, additional light charginos or sfermions are strongly disfavored for example by LEP constraints [120–128], unless their masses are carefully tuned to only produce soft particles in their production and decays. For heavier dark matter, co-annihilation can significantly contribute for example for processes with a light chargino in the t-channel.

The above annihilation mechanisms are often closely linked to LHC search channels. For instance, t-channel chargino annihilation or neutralino/chargino co-annihilation point to more than one light electroweakino, where at least one of the additional light states is a chargino. In this situation one can search for $\tilde{\chi}_j^0 \tilde{\chi}_1^\pm$ or $\tilde{\chi}_1^+ \tilde{\chi}_1^-$ production. One of the classic signatures are tri-leptons, which become challenging when the mass differences between the chargino and the neutralino become small [169]. Similarly, t-channel sfermion exchange or sfermion co-annihilation point towards another light particle, which can be pair-produced through its QED or QCD interactions. As long as the mass difference is not extremely small, such light sfermions are accessible at the LHC, particularly when colored. The situation becomes more challenging when the mediator is a Standard Model particle. To establish this mediator role one would need to establish Z or Higgs coupling to the dark matter sector, for example through invisible Z [170] and/or Higgs decays [171].

Having discussed the potential dark matter annihilation channels, we are now ready to analyze which channels can describe the GC excess in agreement with the relic density and limits from direct detection.

Chapter 4

MSSM solutions to the Galactic center excess

In the previous chapter we have established the evidence for dark matter and introduced a potential dark matter signal from the GC. Furthermore we discussed dark matter annihilation channels that have to be considered when calculating the relic density and annihilation signatures in today's Universe. While it is premature to claim that the GC excess represents a confirmed signal of dark matter annihilation, in this analysis we interpret its properties under this assumption in the framework of the MSSM.

We will start out analysis of the γ–ray spectrum with a discussion of the relevant annihilation channels in Sec. 4.1. We then compare the resulting likelihood map in the μ–M_1 plane with parameter regions that reproduce the measured relic density. In Sec. 4.2 we present the results together with a combined fit including the relic density as an additional data point. The impact of bounds from direct detection experiments on the previous analyses is analyzed in Sec. 4.3. Finally we perform a global fit where we allow all relevant parameters of the neutralino Higgs sector to vary. The results are shown in Sec. 4.4 with and without limits from direction detection. All results are summarized in Sec. 4.5.

The research presented in this chapter has been previously published in Reference [1]. All displayed figures and tables as well as part of the text are identical to the content of this article.

4.1 Fitting the γ–ray spectrum

The MSSM is a prototypical model of weakly interacting massive particles. In the region of parameter space for which the lightest supersymmetric particle (LSP) is a neutralino, a rich spectrum for dark matter emerges, largely dictated by its component fractions of electroweak singlet, doublet, and triplet representations [71–75, 172]. Despite this flexibility, it is somewhat challenging to fit the original characterizations of the GC excess in the MSSM (though viable parameter space does exist [173–179]) due to the generic requirement of efficient mediators [163,

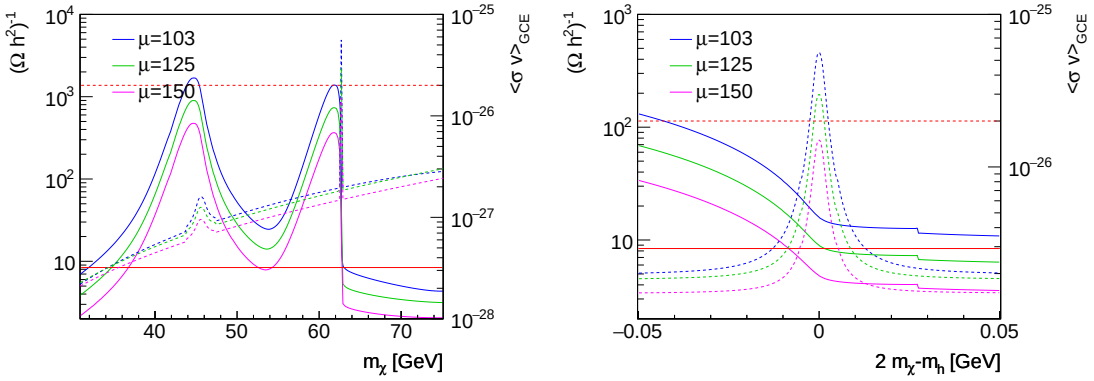

Figure 4.1: Inverse relic density (solid, left axis) and annihilation rate in the GC (dashed, right axis) for an MSSM parameter point where the annihilation is dominated by $\tilde{\chi}_1^0\tilde{\chi}_1^0 \to b\bar{b}$. The right panel is zoomed into the Higgs pole region. Additional model parameters are $\tan\beta = 45$, and third-generation squark masses range around 1 TeV.

180–182]. Such mediators are naturally present in extended models such as the NMSSM [2, 162, 183–188].

In this chapter, we perform an analysis of the MSSM parameter space capable of describing the GC excess as extracted by the Fermi–LAT Collaboration in Reference [16]. We include the wide range of spectra corresponding to the full suite of models for the interstellar emission developed therein. We examine how this range of spectra opens up regions of the MSSM parameter space describing the excess [189] by performing global fits. We use the SFitter framework [18, 37, 38], to fit the spectra consistently with the thermal relic density, the light Higgs boson mass, and the standard set of low energy indirect constraints. The power of such a global analysis rests in its ability to simultaneously interpret the wide range of relevant experimental observations [39, 112, 113, 190–193].

$\chi\chi \to b\bar{b}$

We start by considering an MSSM scenario with a light neutralino responsible for the GC excess. We examine the regions of MSSM parameter space where the annihilation $\tilde{\chi}_1^0\tilde{\chi}_1^0 \to b\bar{b}$ dominates the dark matter annihilation in Fig. 4.1. For light neutralinos, annihilation tends to be dominated by the s-channel light Higgs funnel, rather than the broad A-induced band. We choose the lightest neutralino to be mostly bino, with some Higgsino content to couple to the Z and the light Higgs mediators, and negligible wino content ($M_2 = 700$ GeV). We also fix $\tan\beta = 45$, though the results are rather insensitive to this choice. The varying neutralino mass on the x-axis is generated by adjusting M_1 for each of the fixed values of μ.

On the left y-axis in the left panel of Fig. 4.1 we show the inverse relic density, proportional

to the annihilation rate in the early Universe. The corresponding solid curves exhibit two distinct peaks, one for Z-funnel annihilation and one for h-funnel annihilation. For both peaks the width is given by the velocity spectrum rather than the intrinsic width of the mediators. The enhancement of the two peaks over the continuum end up being comparable, as both annihilation channels are velocity suppressed with $v \lesssim 1/10$. The Z-funnel is coupled to the axial-vector current, whereas the Higgs funnel is suppressed by the small bottom Yukawa coupling. However the neutralino coupling to the Higgs benefits from the larger bino component of the LSP, whereas the Z-coupling is suppressed by the square of the Higgsino component, leading to a comparable cross section in both channels. The measured relic density can be reproduced on the shoulders of the resonance peaks, with a slight preference for larger μ-values and hence smaller couplings.

On the right y-axis of Fig. 4.1, corresponding to the dashed curves, we show the annihilation rate in the GC, with the approximate target rate indicated by the horizontal line. Because of the much smaller velocities, the widths of the resonance peaks are now determined by the physical widths of the Z and the Higgs. The Higgs resonance leads to much larger peak rates, because of its comparably small width. We observe that the continuum as well as the reduced Z-pole annihilation are not capable of explaining the GC excess, but the light Higgs pole scans through the required cross section.

In the right panel of Fig. 4.1 we show a zoomed-in version of the Higgs peak. The interesting parameter regions for a combined fit of the relic density with the GC excess are given by the solid relic density curves crossing the solid horizontal line and the dashed GC lines crossing the dashed horizontal line. As expected from the left panel, there are finely tuned regions around the Higgs pole with today's velocity spectrum, which allow for an explanation of the GC excess via a thermal relic through the process $\tilde{\chi}_1^0 \tilde{\chi}_1^0 \to b\bar{b}$ for $\mu < 140$ GeV. A simultaneous consistency with the measured relic density can be achieved for $\mu \approx 125$ GeV resulting in an LSP mass of 62.5 GeV with 80% bino and 16% respectively 3% Higgsino admixture.

Additional decays of the light Higgs mediator to lighter fermions, like tau leptons, are subleading effects to the annihilation process because of the smaller Yukawa coupling and the smaller color factor.

$\chi\chi \to WW$

At slightly larger LSP masses, the dominant neutralino annihilation channel is $\tilde{\chi}_1^0 \tilde{\chi}_1^0 \to WW$, mediated by a light chargino in the t-channel. Eq. (3.36) indicates that wino and Higgsino LSP content enhance this annihilation rate. In Fig. 4.2 we show the regions of the $M_1 - \mu$ plane explaining the GC excess. In the left panel as throughout our analysis we only show log-likelihood differences with respect to the best fit point as indicated in Eq. (2.4). The best-fit regions typically lead to a Gaussian equivalent of $\chi^2/\text{d.o.f} \approx 1$. In this figure, we fix $M_2 = 700$ GeV, implying that the LSP is a mixture of Higgsino, coupling to electroweak bosons, and bino. The preferred parameter range compensates an increase in $|\mu|$ by an increase in M_1. This way the sizable Higgsino content survives, while the neutralino mass increases, as can be seen in the

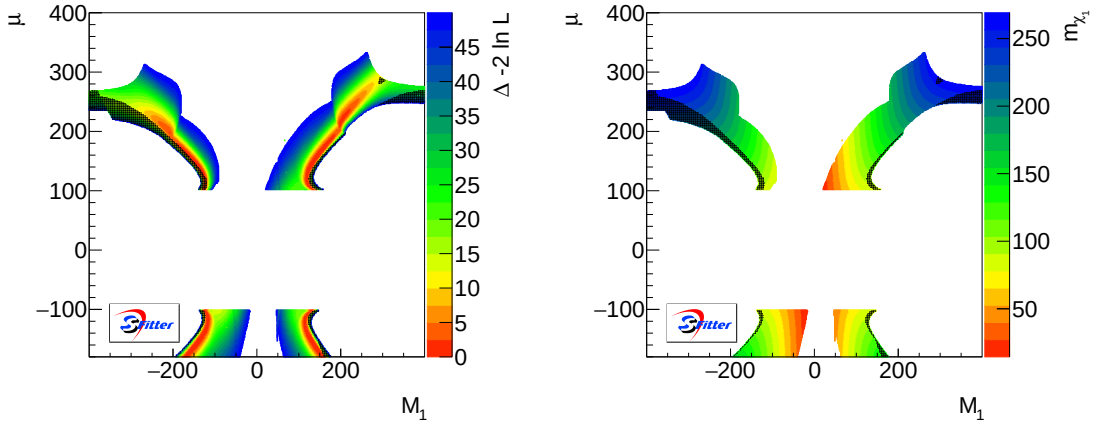

Figure 4.2: Log-likelihood map (left) and corresponding LSP mass (right) based on the Fermi–LAT photon spectrum for $M_2 = 700$ GeV and $\tan\beta = 45$, where $\tilde{\chi}_1^0\tilde{\chi}_1^0 \to WW$ is a dominant annihilation channel. The heavy Higgses are decoupled to 1 TeV. The shaded dots are excluded by the Fermi–LAT limits from dwarf spheroidal galaxies.

right panel of Fig. 4.2. In the lower bands the allowed LSP masses extend to $m_{\tilde{\chi}_1^0} \approx 150$ GeV, without much decrease in the log-likelihood. The change in shape around $M_1 = |\mu| = 200$ GeV is caused by the on-set of the annihilation to top pairs. The t-channel annihilation is mediated by a light stop in the mass range of 500 GeV. Even though the SUSY breaking masses for the squark sector are set to be larger than 1 TeV, these low masses arise from the stop mass matrix due to the large trilinear coupling necessary to adjust the Higgs mass. While light squark masses are severely constrained by collider results it is instructive to see that the annihilation channel is efficient enough to explain the GC excess.

The MSSM parameter regions which allow for efficient annihilation in gauge bosons are strongly correlated in M_1 and μ, but not as tuned as the light Higgs funnel region with its underlying pole condition. Technically, this means that they are easy to identify in a global fit, while the h and Z-funnel are barely visible. In Fig. 4.2 we also indicate the Fermi–LAT limits from dwarf spheroidal galaxies [194] as black dots. While these constraints are visible in the M_1 vs μ plane, they do not significantly interfere with the best-fit regions from the GC excess.

$\chi\chi \to t\bar{t}$

Large annihilation cross sections for $\tilde{\chi}_1^0\tilde{\chi}_1^0 \to t\bar{t}$ can be accomplished by decreasing the heavy pseudoscalar mass to $m_A = 500$ GeV and increasing the effective top Yukawa coupling by choosing $\tan\beta = 3$. Due to the modified pseudoscalar mass terms we can set all squark and slepton masses to 4 TeV and assume a completely decoupled squark and slepton sector. We show the allowed parameter range for heavy winos, $M_2 = 700$ GeV, in Fig. 4.3. From Fig. 4.2 we

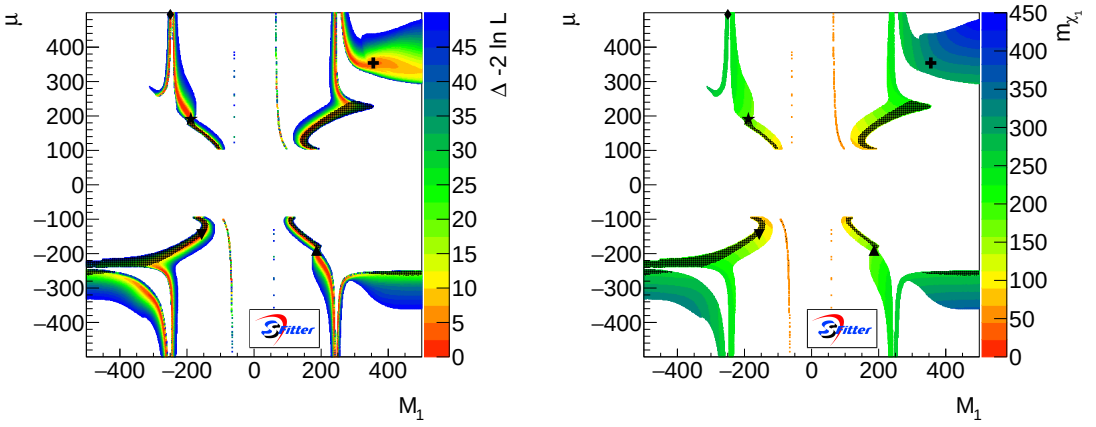

Figure 4.3: Log-likelihood map (left) and corresponding LSP mass (right) based on the Fermi–LAT photon spectrum for $M_2 = 700$ GeV, $\tan\beta = 3$, and $m_A = 500$ GeV, where we also observe the annihilation $\tilde{\chi}_1^0\tilde{\chi}_1^0 \to t\bar{t}$. The shaded dots are excluded by the Fermi–LAT limits from dwarf spheroidal galaxies. The five symbols indicate local best-fitting parameter points.

observe that for $m_{\tilde{\chi}_1^0} > 175$ GeV the annihilation into top pairs follows the WW–annihilation region in the $M_1 - \mu$ plane. We note that the WW–annihilation now behaves exactly the same way, in spite of the lower choice of $\tan\beta$.

According to Fig. 4.3 the allowed mass range now extends to $m_{\tilde{\chi}_1^0} \gtrsim 300$ GeV. The main new feature for the reduced value of $m_A = 500$ GeV is the peak towards large μ values for $M_1 \approx 300$ GeV. The corresponding LSP mass is around 250 GeV, close to the A-pole. On the pole, annihilation is too efficient and the preferred coupling is reduced by a smaller Higgsino fraction in the LSP. Beyond the pole, the allowed region extends to LSP masses above 250 GeV, but with a reduced log-likelihood. If we choose larger values of $\tan\beta$ the same structure remains, but the narrow pole gets washed out into a wider band of dark matter masses. Aside from the A-pole we can now see the narrow h-funnel region, due to larger statistics necessary for this fit. The fact that the large-$|M_1|$ regime does not appear in the upper left corner of Fig. 4.3 is explained by the default SuSpect setup, where this region of parameter space can lead to $m_{\tilde{\chi}_1^+} < m_{\tilde{\chi}_1^0}$. However, an appropriate renormalization scheme like for example an on-shell scheme for the lightest three neutralinos/charginos ensures that the tree-level hierarchy $m_{\tilde{\chi}_1^+} > m_{\tilde{\chi}_1^0}$ remains intact at loop level [195–197].

$\chi\chi \to hh$

In principle, for $m_{\tilde{\chi}_1^0} > m_h$ the LSP can also annihilate to a pair of SM-like Higgs bosons, $\tilde{\chi}_1^0\tilde{\chi}_1^0 \to hh$. While the t-channel neutralino diagram will typically be overwhelmed by the

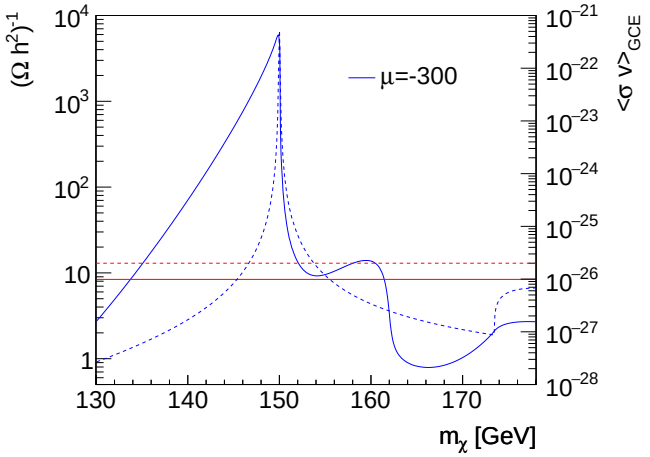

Figure 4.4: Inverse relic density (solid, left axis) and annihilation rate in the GC (dashed, right axis) for an MSSM parameter point where the annihilation receives a contribution from $\tilde{\chi}_1^0\tilde{\chi}_1^0 \to hh$.

annihilation to weak bosons with the same t-channel mediator, an s-channel mediator with $m_{med} \approx 2m_h$ can dominate for small $\tan\beta$. In Fig. 4.4 we show the corresponding effect for dark matter annihilation in the early Universe (left axis) and in the GC (right axis), similar to the $b\bar{b}$ case in Fig. 4.1. The LSP mass is varied through M_1, while $\mu = -300$ GeV and $M_2 = 700$ GeV. The heavy Higgses are light, namely $m_A = 300$ GeV and $m_H \approx 320$ GeV. The heavy Higgs' branching ratio to a pair of light Higgses is $\text{BR}(H \to hh) = 30\%$ [198]. For comparably large velocities depicted by the solid line we see how both s-channel mediators, H and A, contribute through their respective on-shell configuration. In contrast, for the smaller velocities associated with the Fermi–LAT GC excess the CP-odd mediator A completely dominates, while the CP-even H does not contribute visibly. Because only the latter couples to two light Higgs bosons, the annihilation to Higgs pairs leading to the GC excess is difficult to realize in the MSSM. This outcome is different from the case of a single-scalar Higgs portal model [199]. The increase we observe in Fig. 4.4 for $m_{\tilde{\chi}_1^0} > 170$ again shows the onset of the annihilation into two tops.

Based on these example scenarios it is now clear that the GC excess can be realized by the dominant annihilation channels

$$\tilde{\chi}_1^0\tilde{\chi}_1^0 \to b\bar{b}, WW, t\bar{t} \tag{4.1}$$

in more or less finely tuned parameter ranges of the MSSM. Annihilation to light fermions like $b\bar{b}$ is realized through a finely tuned, resonant s-channel mediator. In addition, the LSP can be a

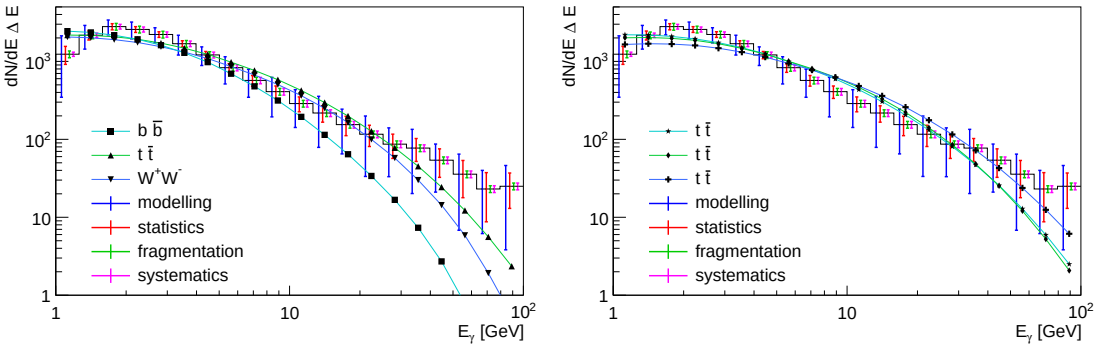

Figure 4.5: Spectra for local best fitting MSSM parameter points, assuming dark matter annihilation dominantly to $b\bar{b}$, WW, $t\bar{t}$ (left) and for three different $t\bar{t}$ annihilation channels (right). The markers correspond to Fig. 4.3, as indicated.

neutralino with $m_{\tilde{\chi}_1^0} = 100 \ldots 350$ GeV with dominant annihilation to WW and/or $t\bar{t}$ pairs.

In Fig. 4.5 we show a set of sample energy spectra for different scenarios, defined as five local best-fitting points in Fig. 4.3 and an exemplary spectrum for h-funnel annihilation into $b\bar{b}$. We overlay the spectra with the Fermi–LAT spectrum shown in Fig. 3.1. The three scenarios with leading decays to $b\bar{b}$, WW, and $t\bar{t}$ shown in the left panel agree similarly well with the Fermi–LAT results. The lowest and highest energy bins cause the largest problem in particular for a light LSP with Higgs funnel annihilation into $b\bar{b}$ pairs. In the right panel of Fig. 4.5 we show three different parameter points, all with a leading annihilation to $t\bar{t}$ pairs, and with LSP masses $m_{\tilde{\chi}_1^0} = 180, 255$, and 320 GeV. The over-all agreement with the Fermi–LAT spectrum gets slightly worse towards larger masses, leading to a Gaussian-equivalent $\Delta\chi^2 = 4$ between the three curves.

4.2 Combining the GC excess with the relic density

After understanding how different annihilation channels can be realized in the MSSM we now perform a global analysis to determine the range of MSSM parameter space which can best describe the GC excess. This will be in the context of an LSP which makes up the entirety of the dark matter and whose abundance is set by freeze-out in a standard cosmology. We also impose the additional constraints shown in Tab. 4.1. For $m_{\tilde{\chi}_1^0} < 45$ GeV and large Z–couplings the additional contribution to the invisible Z-width [170] from decays into pairs of LSPs increases tension with the measurement as we will discuss in Chapter 5, but due to the larger masses in this analysis we do not have to take it into account. The top mass is fixed as an input, because the effect from the small range of values consistent with collider measurements can be

absorbed into small shifts in the stop parameters. Limits from the direct detection experiments Xenon [217, 218], LUX [33], and PandaX [219], are only applied in the Sec. 4.3 of this chapter.

In the upper two panels of Fig. 4.6 we show the allowed parameter range in the bino and Higgsino mass parameters, fixing the wino mass to be essentially decoupled $M_2 = 700$ GeV and also decoupling the heavy Higgs bosons. The upper left panel mainly shows the WW and $t\bar{t}$ annihilation regions; in contrast to Fig. 4.2 we also show the parameter points which give the correct relic density $\Omega_\chi h^2$, quoted in Tab. 4.1. From Fig. 4.1 and Fig. 4.2 we observe that the LSP masses in the $b\bar{b}$ scenario are very close to $m_{\tilde{\chi}_1^0} = m_h/2$, while for the WW scenario they extend from $m_{\tilde{\chi}_1^0} \approx 80$ GeV to around $m_{\tilde{\chi}_1^0} \approx 150$ GeV. As expected from the similar underlying cross sections, the relic density and the GC excess point to similar parameter regions, with slightly larger μ for the relic density and hence smaller annihilation cross sections $\langle\sigma v\rangle$. The annihilation cross section in the prolongation of the black line receives further contributions from t-channel annihilation mediated by sbottom and stop squarks in the mass range of 300 to 500 GeV. However we observe a strong tension between the best fit regions from relic density and GC excess leading to a minimal log-likelihood difference of $-2\log\mathcal{L} = 10$. For the Z-mediated annihilation channel around $M_1 \approx 45$ GeV the relic density can not be connected to the GC excess.

In the upper right panel of Fig. 4.6 we show the result of a properly combined analysis of the GC excess and the measured relic density. Because of the significantly smaller errors, the relic density measurement dominates the combined structures in the M_1 vs μ parameter space. The narrow regions in the parameter space that fit the relic density make it necessary to increase the maximum of the displayed log-likelihood to 200 to improve visibility. In Reference [1] we show the same results with the maximum set to 500, which further widens the displayed regions but reduces the possibility to distinguish the best fit regions. We observe four different annihilation mechanisms: the vertical Higgs-pole $b\bar{b}$ peak next to the Z–mediated annihilation channel for small M_1, the WW region extending diagonally to $M_1 \approx 200$ GeV, and a continuum $t\bar{t}$ region

Measurement	Value	
m_h	$(125.09 \pm 0.21_{\text{stat}} \pm 0.11_{\text{syst}} \pm 3.0_{\text{theo}})$ GeV	[200–208]
$\Omega_\chi h^2$	$0.1188 \pm 0.0010_{\text{stat}} \pm 0.0120_{\text{theo}}$	[30]
a_μ	$(287 \pm 63_{\text{exp}} \pm 49_{\text{SM}} \pm 20_{\text{theo}}) \cdot 10^{-11}$	[209–211]
$\text{BR}(B \to X_s\gamma)$	$(3.43 \pm 0.21_{\text{stat}} \pm 0.07_{\text{syst}}) \cdot 10^{-4}$	[212–214]
$\text{BR}(B_s^0 \to \mu^+\mu^-)$	$(3.2 \pm 1.4_{\text{stat}} \pm 0.5_{\text{syst}} \pm 0.2_{\text{theo}}) \cdot 10^{-9}$	[215, 216]
$m_{\chi_1^+}$	> 103 GeV	[120–128]

Table 4.1: Data used for the fit including their systematic, statistical, and theoretical uncertainties, as appropriate.

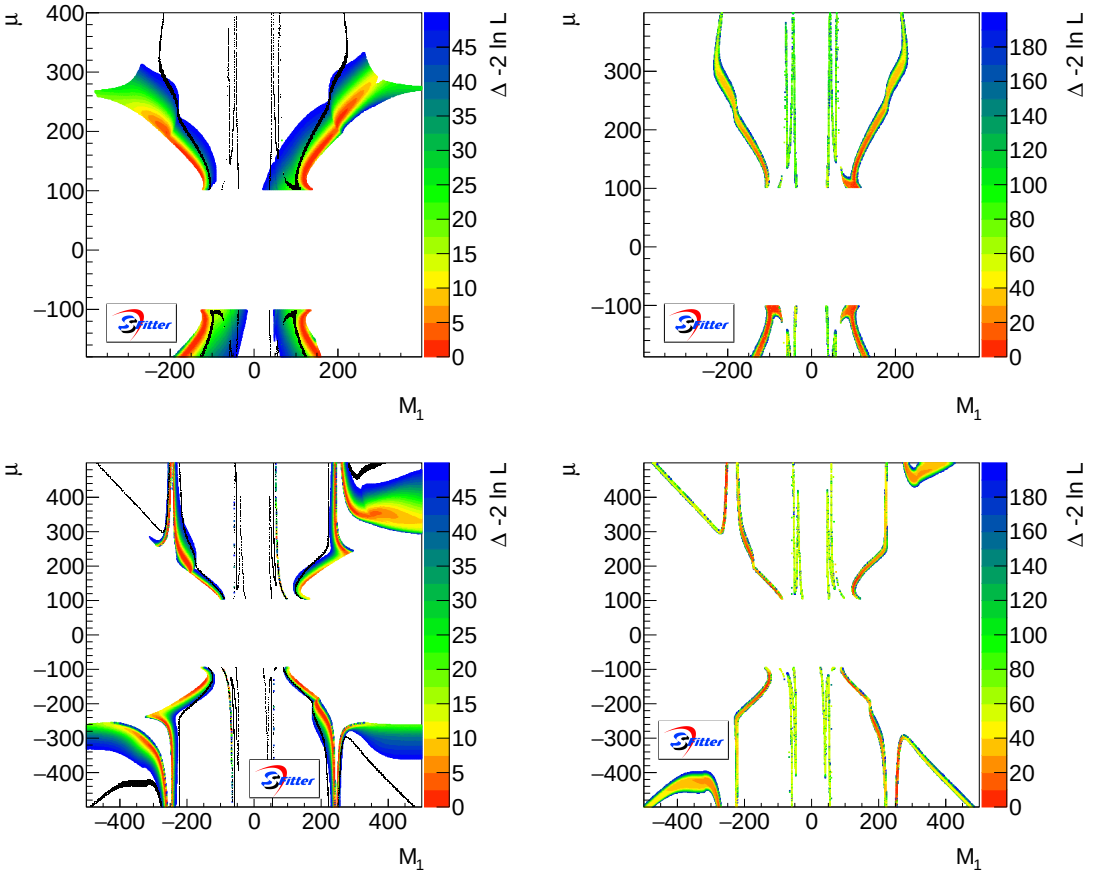

Figure 4.6: Log-likelihood map including the Fermi–LAT photon spectrum and the Fermi–LAT limits from dwarf spheroidal galaxies only (left) and in combination with the observed relic density, and other constraints (right) discussed in the text. We fix $M_2 = 700$ GeV, $m_A = 1$ TeV, $\tan\beta = 45$ (upper) or $m_A = 500$ GeV, $\tan\beta = 3$ (lower), and vary M_1 and μ. The black dots in the left panels are roughly compatible with the observed relic density.

for even larger values of M_1. The best fit region corresponds to the onset of the annihilation into WW with an LSP mass of roughly 80 to 100 GeV, while the fit is not suited to resolve the Higgs-pole with sufficient precision.

In the two lower panels of Fig. 4.6 we show the same parameters, but including a pseudoscalar with $m_A = 500$ GeV. The left panel illustrates the s-channel annihilation regime and in particular above the A-pole the relic density and the GC excess are difficult to reconcile. In the right panel we show how the combined fit follows again the relic density contours with its much

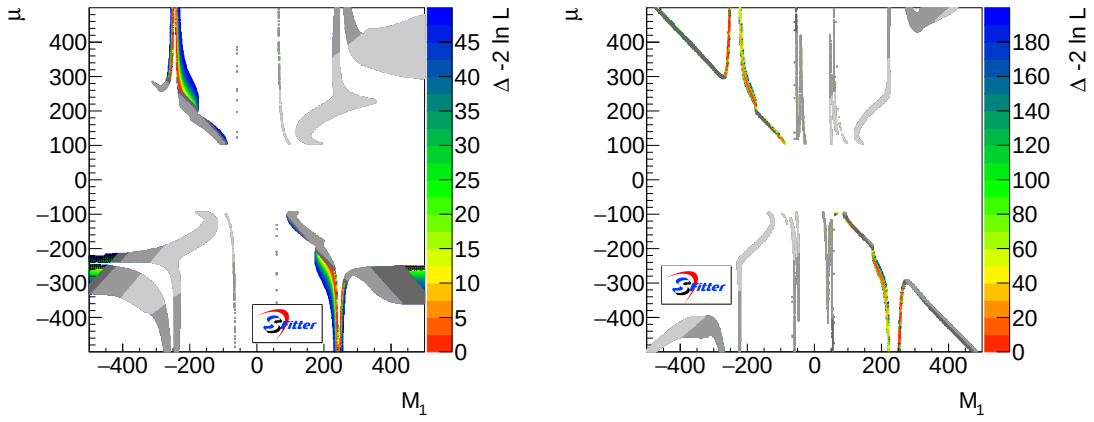

Figure 4.7: Log-likelihood map including the GC excess, combined with Fermi–LAT limits from dwarf spheroidal galaxies and direct detection constraints (left) and after adding the relic density, and other constraints discussed in the text (right). We fix $M_2 = 700$ GeV, $m_A = 500$ GeV, $\tan\beta = 3$, and vary M_1 and μ. Different shades of gray indicate (from light to dark) the most recent exclusion limits from Xenon 100, PandaX and LUX.

smaller uncertainties. This also implies that the asymmetry in the left panel vanishes and the missing region at large negative M_1 and large positive μ re-appears in the combined fit. Here the problem with $m_{\tilde{\chi}_1^0} > m_{\tilde{\chi}_1^+}$ does not occur. The best fit regions recover again the onset of the annihilation into WW. In addition we find valid solutions around the pseudoscalar-pole, in particular for LSP masses marginally above the pole condition.

4.3 Direct detection

An important, recently improved constraint comes from the direct detection experiments probing coherent spin-independent scattering of dark matter with a heavy nucleus. In the left panel of Fig. 4.7 we show the combination of the Fermi–LAT GC excess and different direct detection constraints, not including the observed relic density and hence allowing for a non-standard cosmology where e.g. the LSP is only responsible for a fraction of the relic density. Three shades indicate constraints from Xenon100 [217, 218] (light), PandaX [219] (medium), and LUX [33] (dark). These constraints are included at face value as published by the collaborations rather than in terms of a combined log-likelihood. Instead of a notoriously difficult error bar, we show three different rounds of exclusion limits to illustrate the possible effect of weaker direct detection constraints. The remaining parameter points are colored according to their log-likelihood from indirect constraints and the combined Fermi–LAT GC excess. All of the surviving parameter points rely on the annihilation process $\tilde{\chi}_1^0\tilde{\chi}_1^0 \to t\bar{t}$. The reason is that

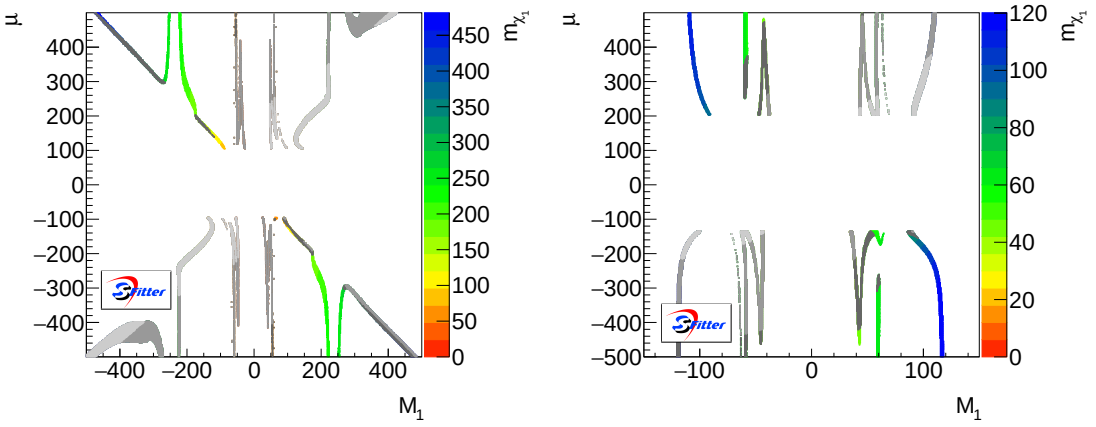

Figure 4.8: Log-likelihood map including the Fermi–LAT photon spectrum, direct detection constraints, the observed relic density, and other constraints discussed in the text for fixed $m_A = 500$ GeV and $M_2 = 700$ GeV, $\tan\beta = 3$ (left) or $M_2 = 120$ GeV, $\tan\beta = 7$ (right). Different shades of gray indicate (from light to dark) the most recent exclusion limits from Xenon100, PandaX and LUX.

the heavy (pseudo-)scalar mediator does not couple strongly to the non-relativistic proton content, leaving the corresponding explanation of the GC excess untouched. The asymmetry between different signs of the input parameters arises from a sign change of one Higgsino component of the LSP. The limit on the spin–independent interaction cross section is violated by Higgs mediated processes. For different signs of μ and M_1 the Higgsino contributions in the Higgs–neutralino coupling in Eq. (3.34) cancel each other, making it possible to avoid the constraints from direct detection.

For the right panel of Fig. 4.7 we combine the Fermi–LAT GC excess, direct detection constraints, the observed relic density, and the other constraints shown in Tab. 4.1. As shown before, the preferred regions in the $M_1 - \mu$ plane are now slightly shifted and defined by the correct prediction of the relic density. With this modification, the A-funnel with an annihilation to $t\bar{t}$ as well as a small range of points with the annihilation signature $\tilde{\chi}_1^0\tilde{\chi}_1^0 \to WW$ avoid direct detection constraints.

A key parameter is the mass of a dark matter candidate which simultaneously explains the observed relic density and the GC excess, and at the same time respects all constraints in Tab. 4.1 as well as those from direct detection experiments. In Fig. 4.8 we show all points with $\Delta(-2\log L) \lesssim 200$, colored according to the LSP mass $m_{\tilde{\chi}_1^0}$. In the left panel we fix $M_2 = 700$ and $\tan\beta = 3$, as before. The low value of $m_A = 500$ GeV opens a $t\bar{t}$ annihilation region with $m_{\tilde{\chi}_1^0} \approx 200$ GeV. In addition we see a few allowed points with $m_{\tilde{\chi}_1^0} \lesssim 100$ GeV in the WW regime.

In the right panel of Fig. 4.8 we fix $M_2 = 120$ GeV, allowing for a significant wino fraction in

the LSP. According to Eq. (3.36) the wino content generally allows for a sizable annihilation rate through a t-channel chargino, implying that the LSP mass after requiring the annihilation rate matching the GC excess as well as the observed relic density will never exceed 120 GeV. On the other hand, a Higgsino admixture can lead to lighter valid dark matter candidates. We again identify the very narrow h-peak and the broader Z-peak. They define the allowed parameter points with $m_{\tilde{\chi}_1^0} \approx 45$ GeV and $m_{\tilde{\chi}_1^0} \approx 63$ GeV. In addition, we see a non-resonant band of allowed points with $m_{\tilde{\chi}_1^0} = 100 \ldots 120$ GeV, with an annihilation into WW pairs and chargino co-annihilation via a W boson for the relic density. Annihilation into a pair of top quarks is kinematically impossible. Direct detection experiments have a weaker impact because gaugino mixtures have smaller couplings to the light Higgs.

In summary, we see that in particular for a mixed wino-Higgsino LSP the annihilation channels $b\bar{b}$, and WW survive current direct detection limits, but with a much reduced number of allowed parameter points. For $t\bar{t}$ final states the annihilation via a light pseudoscalar escapes the direct detection limits. With the next generation of direct detection experiments [31] it should be possible to probe these remaining MSSM parameter points.

4.4 Global parameter study

Finally, we perform a global MSSM fit including all relevant parameters of the neutralino/chargino parameter space. To assure the possibility of the heavy Higgs funnel we fix $m_A = 500$ GeV and vary:

$$\begin{aligned} &|M_1| < 500 \text{ GeV} && |M_2| < 700 \text{ GeV} && |\mu| < 500 \text{ GeV} \\ &|A_t| < 7 \text{ TeV} && \tan\beta = 2 \ldots 45 \,. \end{aligned} \tag{4.2}$$

The remaining parameters, including squark masses, slepton masses, and trilinear couplings, are decoupled at 4 TeV. This choice allows for points interpolating between the two scenarios shown in Fig. 4.8: bino-Higgsino dark matter and wino-Higgsino dark matter. In addition, the simultaneous variation of $\tan\beta$ and A_t ensures that for any value of $\tan\beta$ we can generate the correct light Higgs mass while at the same time scanning the bottom Yukawa coupling or the width of the heavy Higgses.

In the upper panels of Fig. 4.9 we show the result of a global analysis taking into account all constraints defined in Tab. 4.1, but not including direct detection bounds. For example the $\mu - M_1$ plane is now shown as a profile likelihood after maximizing with respect to the remaining model parameters. In general, this leads to a broadening of all features discussed before. We still see the usual narrow regions corresponding to the annihilation channels $\tilde{\chi}_1^0\tilde{\chi}_1^0 \to WW$ and $t\bar{t}$. In addition, broader structures for large $|\mu| \sim |M_1|$ are generated by the $\tan\beta$-enhanced annihilation $\tilde{\chi}_1^0\tilde{\chi}_1^0 \to A \to b\bar{b}$. They are much wider than all other structures because the heavy Higgs width scales with $\tan^2\beta$. In the middle upper panel we see how the low-M_1 scenarios reach a better agreement with data towards large $\tan\beta$, and how the width of the pseudoscalar

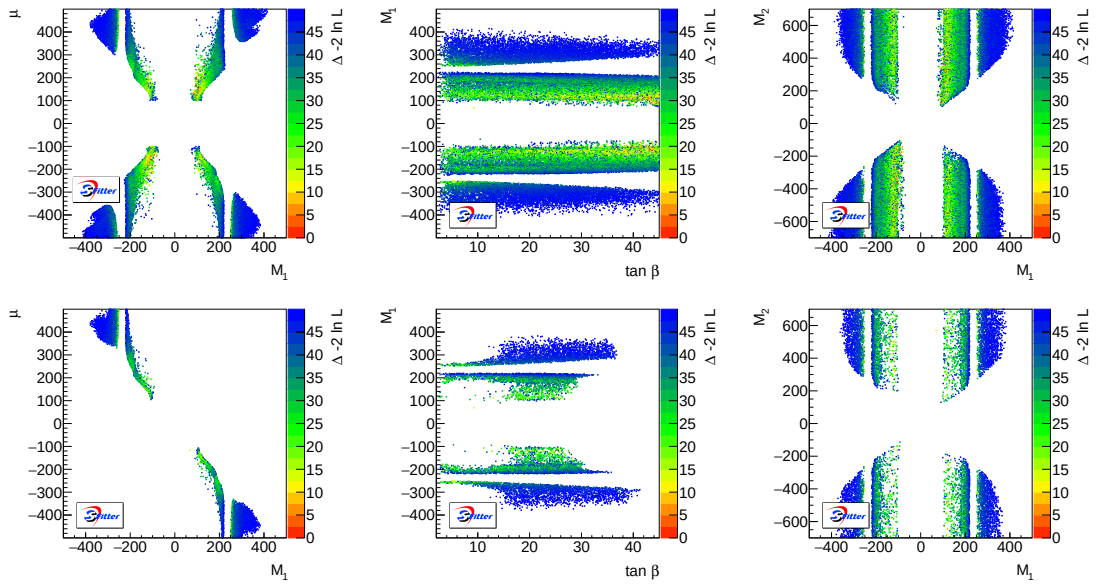

Figure 4.9: Log-likelihood map for the combined SFitter analysis of the Fermi–LAT photon spectrum, the observed relic density, and other constraints with (lower) and without (upper) including the LUX direct detection bounds.

Higgs with $m_A = 500$ GeV increases. Furthermore we observe that $\tan\beta$ has hardly any global effect on the annihilation rate, both for the GC excess and for the observed relic density. Finally, in the right panel we observe a strong correlation between M_2 and M_1, similar to the first panel, but with more washed-out structures in the profile likelihood. The Z-funnel and h-funnel are not resolved by the usual global analysis, and do not appear. From the previous discussion, it is clear that they are viable in the absence of direct detection constraints.

In the lower panels of Fig. 4.9 we add the LUX direct detection constraints. All general structures in the $\mu - M_1$ plane, corresponding to the different decay channels, survive. An independent sign change in μ and M_1 is no longer possible because of the large degree of fine-tuning. The main difference between this global result and the previous, two-dimensional analysis is that for large $\mu \sim -M_1$ the pseudoscalar Higgs funnel mediates an annihilation to $b\bar{b}$ pairs at large $\tan\beta$.

Another new feature in the global fit is an allowed Higgsino LSP region for $M_1 = 100 \ldots 150$ GeV and $\tan\beta = 15 \ldots 25$. It corresponds to a combined annihilation to WW and ZZ pairs. Following Eq. (3.36) and Eq. (3.33) both, the $\tilde{\chi}_1^0 - \tilde{\chi}_1^\pm - W$ and $\tilde{\chi}_1^0 - \tilde{\chi}_1^0 - Z$ couplings increase for large $\tan\beta$. This way they lead to an efficient annihilation, but are also ruled out by direct detection constraints. When we reduce $\tan\beta \to 1$, the $\tilde{\chi}_1^0 - \tilde{\chi}_1^\pm - W$ coupling approaches a finite value, while the $\tilde{\chi}_1^0 - \tilde{\chi}_1^0 - Z$ vanishes.

4.5 Conclusion

Based on a realistic estimate of the different sources of uncertainty we have shown that the lightest neutralino in the MSSM can explain the Fermi–LAT GC excess. The different annihilation channels $\tilde{\chi}_1^0\tilde{\chi}_1^0 \to b\bar{b}$, WW, and $t\bar{t}$ define the corresponding LSPs with increasing masses. The annihilation channel $\tilde{\chi}_1^0\tilde{\chi}_1^0 \to hh$ does not work in the MSSM, because of the velocity suppression of the CP-even heavy Higgs funnel. Nevertheless, viable explanations of the GC excess in the MSSM can annihilate to a wide range of Standard Model states and cover a mass range from 45 GeV to well above 250 GeV.

If one demands that the LSP is a standard thermal relic, the preferred regions of parameter space slightly shift. The typical width of the structures in parameter space decreases significantly, corresponding to the small uncertainties from the Planck fits. Consequently, the allowed region of a combined SFitter analysis follows the patterns of the correct relic density. The best-fit region is again defined by the $b\bar{b}$, WW, and $t\bar{t}$ annihilation channels; it extends to LSP masses up to 300 GeV, in particular in combination with a pseudoscalar heavy Higgs mass around 500 GeV. In addition, we confirm two more features in the MSSM parameter space. First, a $\tan\beta$-enhanced annihilation of heavy neutralinos to $b\bar{b}$ pairs can be mediated by the pseudoscalar Higgs in complete analogy to the top quark case. Second, the different scaling of the neutral current and charged current couplings of the neutralino/chargino sector opens an allowed wino region for intermediate $\tan\beta$.

Finally, when we apply the full set of limits, the direct detection constraint cuts deeply into the allowed parameter space. Nevertheless, for a mixed wino-Higgsino LSP all three annihilation channels with their corresponding regions of parameter space survive. Most notably, a heavy neutralino annihilating to top or bottom pairs remains largely intact. Ignoring the relic density constraint and only considering the GC excess combined with direct detection constraints does not improve the situation qualitatively. All of our preferred regions of parameter space should be covered by the next generation of direct detection experiments.

Chapter 5

Relating the Galactic center excess to the Higgs invisible branching ratio

Searches for dark matter coupled to Standard Model fields beyond the gravitational interaction follow three distinct strategies: direct detection, indirect detection, and production at colliders. Global fits try to answer the key question how in the case of weakly interacting dark matter the different search strategies can complement and inspire each other. One of the main search strategies for dark matter at the LHC are invisible Higgs decays, most notably in weak boson fusion [171, 220, 221]. For example, in models without new strongly interacting particles such invisible Higgs decays will drive mono-jet searches and are likely to dominate over dark matter pair production in weak boson fusion [222]. In the previous chapter we have shown that it is possible to simultaneously fit the relic density and the Fermi–LAT excess and avoid direct detection constraints. In this analysis we will establish a specific link between the Fermi GC excess [30, 86–100, 223] and invisible Higgs decays at the LHC [224–233] in the framework of the NMSSM [21, 117, 129–133]. Making use of the extended Higgs particle content we can easily fit the GC excess with light dark matter candidates which turns out to create a strong link to invisible decays of the SM–like Higgs.

In Sec. 5.1 we discuss invisible Higgs decays in the framework of the MSSM. Since it is not possible to connect the resulting regions of parameter space to the GC excess, we move to the NMSSM that allows for annihilations via a light pseudoscalar that is excluded in the MSSM.

Because of the structure of the NMSSM we can follow two strategies to accommodate the GC excess [162, 234]: first, we can keep the standard bino–Higgsino LSP composition of the MSSM and only couple the neutralinos to the light additional pseudoscalar. Alternatively, we can replace the bino content by a singlino content and assume a singlino–Higgsino, or better bino–singlino–Higgsino LSP. Again, it will couple to the pseudoscalar mediator.

For the bino–Higgsino case the relevant LSP and mediator states are not decoupled from the Standard Model. This means that for example the pseudoscalar mediator can be searched for at the LHC [162]. The singlino–Higgsino channel is more challenging. We will study the phenomenology of the NMSSM singlet/singlino sector and its TeV-scale parameter space linked

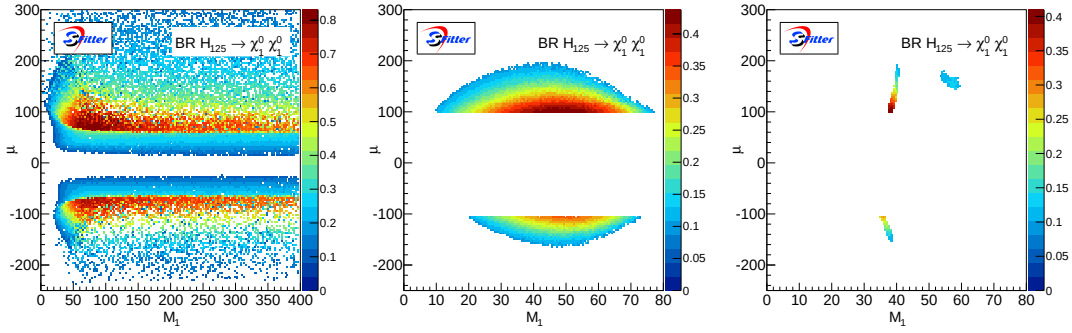

Figure 5.1: Branching ratio for $H_1 \to \tilde{\chi}\tilde{\chi}$. From left to right we consecutively apply the constraints: (1) $m_{H_{125}} = 122 \ldots 128$ GeV and $\text{BR}_{\text{inv}} > 10\%$, (2) $m_{\tilde{\chi}^\pm} > 103$ GeV, and (3) $\Omega_{\tilde{\chi}} h^2 = 0.107 \ldots 0.131$. The projections are profiled over M_2, showing the maximal branching ratio. The z-axis for the coloring scheme is rescaled to the maximum value of each plot.

to the GC excess in Sec. 5.2.1.

In Sec. 5.2.2 we will link the parameter space yielding the necessary cross section to the size of invisible Higgs couplings. It turns out that similar to a dark matter Higgs portal [235–250] the NMSSM interpretation of the GC excess leads to invisible Higgs decays with branching ratios accessible during the upcoming LHC run. In Sec. 5.3 we will apply the same criteria to a high-scale NMSSM setup. For this model a global SFitter likelihood analysis without the GC excess is useful, before we turn to the link between the GC excess and invisible Higgs decays.

The research presented in this chapter has previously been published in Reference [2]. All displayed figures and tables as well as part of the text are identical to the content of this article.

5.1 Invisible Higgs decays in the MSSM

Before we discuss the relation of the GC excess and LHC searches in the NMSSM we briefly review the constraints on invisible Higgs decays in the MSSM with a SM-like light Higgs. In the MSSM, the LSP can be a combination of bino, wino, and Higgsino. First, invisible Higgs decays $H \to \tilde{\chi}\tilde{\chi}$ require the LSP to be lighter than 63 GeV. Therefore, at least one of the mass parameters μ, M_1, and M_2 has to be around 100 GeV or below. The second ingredient is the size of the coupling. Its form given in Eq. (3.34) requires a mixed Higgsino-gaugino states, which means we again expect to need small values of $|\mu|$.

The left panel of Fig. 5.1 illustrates the dependence of the invisible branching ratio on μ and M_1. We vary the MSSM parameters μ, M_1, and M_2 and profile over the non-displayed parameter,

showing the maximal invisible branching ratio. For all points shown we require the Higgs invisible branching ratio to be at least 10%. In this example we set the sfermion and gluino masses to 2 TeV, so that they decouple from the electroweak sector, and as before set $\tan\beta = 40$. The Higgs-sector parameters M_A, A_t and A_τ now have to be carefully chosen to reproduce the observed Higgs mass.

Without constraints on the chargino mass and dark matter properties the maximal branching ratio exceeds 80%. The relevant parameter space is located around $|\mu| = 80$ GeV and $M_1 = 100 \ldots 150$ GeV. Away from this region, the LSP is no longer well tempered, reducing the coupling and leading to an invisible branching ratio below 10%.

In the center panel of Fig. 5.1 we add the LEP limits [120–128] on the chargino mass. The minimal value of 103 GeV translates into a lower bound $\mu, M_2 \gtrsim 100$ GeV. The lower bound on μ can be seen directly in Fig. 5.1. The constraint on M_2 works indirectly: it excludes wino LSPs lighter than 63 GeV, which means that a light LSP has to be mainly bino. This is visible as an upper bound $M_1 < 80$ GeV.

In addition to the LSP mass, we also have to adjust the couplings. The required bino-Higgsino mixing restricts the allowed parameter region to $M_1 < 80$ GeV and $|\mu| < 200$ GeV. Constant invisible branching ratios correspond to the two half-circles in the center panel of Fig. 5.1. Without the mass constraints on the chargino and the Higgs we would see two approximately circular shapes centered around $M_1 \approx 50$ GeV and slightly bigger values of $|\mu|$. This reflects the preference for a light, well-tempered LSP with roughly equal bino and Higgsino fractions. In particular the chargino mass limit simply removes the region with $|\mu| \lesssim 100$ GeV. The maximum invisible branching ratio in the MSSM is 45%.

In the right panel of Fig. 5.1 we add the Planck measurement of the LSP relic density. In this configuration the annihilation proceeds via an s-channel Z-boson. Planck excludes neutralino masses around 45 GeV, where resonant annihilation leads to a too small relic density. Three distinct strips remain compatible with the measured relic density: two with neutralino masses between 35 GeV and 40 GeV, and one between 50 GeV and 55 GeV. However, the latter is excluded by Xenon100. This additional constraint further reduces the maximal invisible branching ratio

$$\mathrm{BR}(H_{125} \to \tilde{\chi}\tilde{\chi}) \lesssim 50\% \qquad \text{for} \quad \mu = 100\ \text{GeV}, \quad M_1 = 45\ \text{GeV}\,, \tag{5.1}$$

Finally, we consider Z-decays to neutralinos for neutralino masses smaller than 45 GeV. The corresponding partial width adds to the width from Z-decays into neutrinos, whose SM prediction already exceeds the measured value of $\Gamma(Z \to \text{inv})$ by 1.9 MeV. While an invisible Higgs branching ratio of 10% only adds an additional 0.2 MeV to the Z-width, a Higgs branching ratio of 40% can imply an additional Z-decay width of 3 MeV. This increases the already existing tension between theory prediction and experimental results for invisible Z-decays [251].

We conclude that the MSSM provides viable dark matter candidates, that reproduce the Planck measurement of the relic density and lead to a large invisible decay width of the SM-like Higgs. As discussed in Sec. 4.1, the annihilation via the Z-boson can not generate a sufficiently

large annihilation cross section to fit the γ-ray excess. Therefore we will turn to the NMSSM where the annihilation can get enhanced by a light pseudoscalar mediator.

5.2 The GC excess in the NMSSM

Following our previous analysis, the excess of γ-rays measured by Fermi–LAT can be explained by annihilating dark matter distributed spherically around the center of our galaxy. Its spectrum gives preferred mass values for different dark matter candidates depending on the final state. For an annihilation to bottom quarks the preferred mass of the dark matter agent ranges around 40 GeV [86–100], extending all the way to 70 GeV [93, 97, 100]. In our NMSSM analysis of the $b\bar{b}$ case we will follow Reference [93, 97, 100] and assume a conservative LSP of 30 GeV to 70 GeV. The annihilation cross section should be in the range of $\sigma v \approx 1.8 \cdot 10^{-26}\text{cm}^3/\text{s}$ [86–100] [*], consistent with the Planck thermally averaged results [30] within appropriate theoretical or parametric uncertainties for example from the choice of the dark matter profile. Such values are intriguingly close to the expectations for a thermally produced weakly interacting dark matter particle (WIMP) [71–75, 172, 172].

In the MSSM the preferred mass range of a dark matter agent reproducing the GC excess is a challenge and typically relies on dark matter annihilation into a pair of gauge bosons [112, 189] or top quarks as we have illustrated in the previous chapter. In the absence of the annihilation through an efficient s-channel mediator decaying for example into $b\bar{b}$ pairs the predicted relic density in the Universe tends to be too large. Finding efficient annihilation channels is a serious issue in supersymmetric models [39, 156–161] in particular for light dark matter particles with masses below 80 GeV: s-channel annihilation through the Z-pole, the SM-like Higgs resonance H_{125}, or a heavy Higgs resonance are forbidden by other constraints or too small. Any co-annihilation channel requires an additional supersymmetric particle within 10% of the LSP mass [164–168], which is disfavored by LEP constraints [120–128]. The way out is an additional mediator, ideally a pseudoscalar with a mass not far above twice the LSP mass [183, 184]. This feature is clearly visible in an analysis in terms of simplified models or effective field theory [163, 180, 181].

As an extension of the MSSM, the NMSSM provides exactly such a mediator, the pseudoscalar part of the singlet/singlino superfield mixed with the MSSM-like pseudoscalar [134–141]. In the required mass range it will naturally decay to $b\bar{b}$ pairs, and with a reduced branching ratio to $\tau^+\tau^-$. Such an NMSSM setup can be tested in a parameter scan [173–178] and then linked for example to 4-body Higgs decay [185], trilepton searches at the LHC [186, 187] or even the electroweak phase transition [188].

[*] In contrast to the previous chapter we will only fit the annihilation cross section instead of the full spectrum. The analysis has been performed before the Fermi–LAT spectrum was available and relies on cross section estimations from the indicated publications.

Before we start the analysis of the NMSSM parameter space, we will list the crucial measurements that we have to take into account for light dark matter particles. In addition to the dark matter relic density and the observed Higgs mass value there exists a wealth of measurements in electroweak and B-physics which might constrain supersymmetric models. The data which we use for our SFitter parameter study are listed in Tab. 5.1.

In comparison to the previous analysis, the decay width of the Z-boson becomes important for light neutralinos. The invisible width for Z-decays, $\Gamma_{Z\to\text{inv}}$ [170], is identified with the additional contribution to the Z-width from decays into a pair of LSPs. For LSP candidates with a mass smaller than 45 GeV, the LEP results for the Z-width become powerful constraints, limiting the partial decay width of Z to neutralinos. If the sum of the lightest CP-even and CP-odd Higgs is smaller than the mass of the Z-boson, the total width gets an additional contribution. This contribution is compared to the difference between the SM prediction and the measured total width of the Z. The measurement of the anomalous magnetic moment of the muon a_μ can only be satisfied with small slepton masses around 400 GeV or lower. As we decouple the sfermion sector this measurement will only lead to an overall constant contribution to the log-likelihood.

The mass of the top is an input parameter to the supersymmetric SM-like Higgs. In addition, we require the lightest chargino to have a mass above 103 GeV, because it is very hard to avoid the LEP2 constraints for charged particle production [120–128]. This constraint becomes important when we consider regions with small $\mu < 200$ GeV. Finally we also include the Xenon100 [217, 218] limits on direct detection. They are most powerful in the 30 to 100 GeV

measurement	value and error	
$\Omega_{\tilde\chi} h^2$	$0.1188 \pm 0.0010_{\text{stat}} \pm 0.0120_{\text{theo}}$	[30]
$m_{H_{125}}$	$(125.09 \pm 0.21_{\text{stat}} \pm 0.11_{\text{syst}} \pm 3.0_{\text{theo}})$ GeV	[200–208]
$\Gamma_{Z\to\text{inv}}$	$(-1.9 \pm 1.5_{\text{stat}} \pm 0.2_{\text{theo}})$ MeV	[251]
$\Gamma_{Z\to\text{Higgs}}$	$(6.5 \pm 2.3_{\text{stat}} \pm 1.0_{\text{theo}})$ MeV	[251]
a_μ	$(287 \pm 63_{\text{exp}} \pm 49_{\text{SM}} \pm 20_{\text{theo}}) \cdot 10^{-11}$	[209–211]
$\text{BR}(B \to X_s\gamma)$	$(3.43 \pm 0.21_{\text{stat}} \pm 0.07_{\text{syst}}) \cdot 10^{-4}$	[212–214]
$\text{BR}(B_s^0 \to \mu^+\mu^-)$	$(3.2 \pm 1.4_{\text{stat}} \pm 0.5_{\text{syst}} \pm 0.2_{\text{theo}}) \cdot 10^{-9}$	[215, 216]
$\text{BR}(B^+ \to \tau^+\nu)$	$(1.41 \pm 0.43_{\text{stat}}) \cdot 10^{-4}$	[252]
Δm_{B^0}	$(0.510 \pm 0.004_{\text{stat}} \pm 0.003_{\text{syst}} \pm 0.400_{\text{theo}}) \cdot 10^{12}\,\hbar\text{s}^{-1}$	[252]
$\Delta m_{B_s^0}$	$(17.69 \pm 0.08_{\text{stat}} \pm 7.00_{\text{theo}}) \cdot 10^{12}\,\hbar\text{s}^{-1}$	[252]
m_t	$(173.5 \pm 0.6_{\text{stat}} \pm 0.8_{\text{syst}})$ GeV	[253–255]
$m_{\chi_1^+}$	> 103 GeV	[120–128]
$\sigma_{\tilde\chi N}$	direct detection limits	[217, 218]

Table 5.1: Data used for the fit including their systematic and statistical errors from the measurements and theoretical errors for SUSY calculations as far as they are considered.

range, so this measurement will prove to have a strong exclusion power for the scenarios we are interested in.

Dark matter explanations of the GC excess [86–100] are described by two parameters: the LSP mass and the annihilation cross section in the center of the galaxy. For our first analysis we will assume the conservative range [93, 97, 100]

$$\begin{aligned} m_{\tilde{\chi}} &= (30 \ldots 70)\,\text{GeV} \\ \sigma v &= (0.4 \ldots 10) \cdot 10^{-26}\,\frac{\text{cm}^3}{\text{s}} \end{aligned} \tag{5.2}$$

A more detailed analysis in the two-dimensional plane will be part of the full analysis in Sec. 5.2.2.

Similar mass ranges of the LSP have already been targeted by the ATLAS and CMS searches [256–258]. As those searches consider the specific setup of a bino-like LSP with a wino-like lightest chargino and a second-lightest neutralino, it is highly convoluted to reliably include the ATLAS and CMS limits in our analysis. Moreover they typically assume light sleptons, while we decouple the sfermion sector.

For the TeV-scale fits we use the typical SFitter setup described in Chapter 2. When we display observables instead of the likelihood function, only points that pass sharp criteria, e. g. $\Omega_{\tilde{\chi}} h^2$ within the theory uncertainties, are displayed. Similar to a profile likelihood, we assign the value of the point with highest likelihood to each bin.

We assume a $\mathbb{Z}_3$-symmetric NMSSM introduced in Sec. 3.2.2, where all input parameters are set at the scale 1 TeV. The absence of unifying assumptions leads to a large number of model parameters, namely the slepton and squark masses, the trilinear couplings and the gaugino mass parameters. In this study we decouple the squarks, sleptons, and gluinos by setting the soft masses to 10 TeV and the trilinear couplings to zero, because these sectors are not experimentally relevant. To obtain the correct 125 GeV Higgs mass we adjust the stop masses in the TeV-range appropriately. For the Higgs–singlet sector the relevant input parameters are

$$\{\lambda, \tilde{\kappa}, A_\lambda, A_\kappa, \tan\beta, \mu\}\ . \tag{5.3}$$

Alternatively, we can replace $A_{\lambda,\kappa}$ by the diagonal entries in the pseudoscalar mass matrix of Eq. (3.43). The neutralino–chargino sector adds the free parameters M_1 and M_2.

While A_κ is given at the SUSY scale of 1 TeV, NMSSMTools computes the Higgs masses at the averaged squark masses, in our case around 10 TeV. The scale dependence of the singlet related parameters mentioned in Sec. 3.2.2 will be particularly relevant for the high-scale NMSSM. However for the coupling A_κ, the running of the parameter between SUSY scale and

the evaluation scale is essential for our understanding of the results. The approximate form of A_κ at the averaged squark mass scale can be computed from the RGE in Eq. (3.54) via

$$\begin{aligned} A_\kappa(10\text{ TeV}) &= A_{\kappa,0} 10^{\frac{3\lambda\tilde{\kappa}^2}{4\pi^2}} + \left(10^{\frac{3\lambda\tilde{\kappa}^2}{4\pi^2}} - 1\right)\frac{A_\lambda}{\tilde{\kappa}^2} \\ &\approx A_{\kappa,0} + \frac{3\log 10}{4\pi^2}\lambda A_\lambda \ . \end{aligned} \tag{5.4}$$

Due to the large value of $|A_\lambda|$, that further increases with the absolute value of μ, A_κ increases from -250 GeV to the order of 30 GeV at 10 TeV for $\lambda = 0.2$ and $A_\lambda = 8$ TeV. When we consider small singlet masses, the scale dependence of A_κ plays an important role in their parameter dependence.

5.2.1 Light dark matter solutions to the GC excess

With the GC excess of gamma ray photons we add an experimental motivation for a light neutralino in combination with a light pseudoscalar mediator [86–100, 163, 180, 181] to the merely constraining experimental results in Tab 5.1. The excess can be explained by a neutralino in the range of 30 GeV to 40 GeV or even 70 GeV, that annihilates into a pair of fermions, for example $\tilde{\chi}\tilde{\chi} \to b\bar{b}$. For a type-II two-Higgs doublet model the bottom and tau Yukawa couplings are aligned, which means that the assumed decay to a $b\bar{b}$ pair will dominate over the accompanying decay to $\tau^+\tau^-$. In our preferred data regions the A_1 decays into $b\bar{b}$ (94%) as well as into $\tau\bar{\tau}$ (6%) pairs, the ratio reflecting the size of the Yukawa couplings and the color factor in the case of quarks.

Following the results from Chapter 4 in the MSSM such a light neutralino LSP is a problem in the presence of direct SUSY and Higgs search results because there is no obvious way to annihilate it efficiently enough to arrive at the necessary annihilation rate. Different co-annihilation channels [164–168] require new charged states in reach of LEP2 and are therefore not viable [120–128].

In contrast, the two pseudoscalars in the NMSSM can mediate a sufficiently fast annihilation, because the LSP annihilation through its resonance pole is not p-wave suppressed like it is for vector bosons or scalars. While the mass of the MSSM-like pseudoscalar Higgs is strongly constrained by heavy neutral and charged Higgs searches, the additional light pseudoscalar can be mostly singlet. The neutralino coupling to such a mediator is given in Eq. (3.47) for a largely singlino mediator turning into Eq. (3.48).

We consider a generic NMSSM scenario based on a light singlino with a bino and a Higgsino admixture, i. e. $\tilde{\kappa} \ll 1$ [185]. An alternative solution combines a bino-Higgsino LSP with an NMSSM pseudoscalar mediator [162], but will not lead to the measurable invisible Higgs decay we are interested in. Light neutralinos with a sizable wino or Higgsino component are essentially ruled out by Z-pole measurements and by chargino searches at LEP, so we decouple the wino at $M_2 = 4$ TeV. In this limit we can link $\tilde{\kappa}$ to the neutralino mass through Eq. (3.45). We then

adjust A_λ such that the singlet component of the SM-like Higgs is minimized, avoiding Higgs sector constraints altogether [19, 40, 41].

If the annihilation process leading to the GC excess proceeds via a pseudoscalar decaying into a pair of bottom quarks, today's dark matter annihilation cross section is [163, 180, 181]

$$\sigma v\Big|_{v=0} \approx \frac{3}{2\pi} \sqrt{1-\frac{m_b^2}{m_{\tilde\chi}^2}}\, \frac{g_{A_1\tilde\chi\tilde\chi}^2 g_{A_1 bb}^2 m_{\tilde\chi}^2}{\left(m_{A_1}^2 - 4m_{\tilde\chi}^2\right)^2 + m_{A_1}^2\Gamma_{A_1}^2} \,. \tag{5.5}$$

Using SFitter we analyze the NMSSM parameter space with a focus on the SM-like Higgs mass, the LSP mass, the observed relic density $\Omega_{\tilde\chi}h^2$, the Z width measurements, the Xenon direct detection constraints, and the GC excess. As expected from Sec. 3.2.2 the key model parameters are the Higgsino mass parameter μ, the singlet mass parameter $\tilde\kappa$, and the coupling λ, which links the singlet to the MSSM Higgs sector.

In Fig. 5.2 we choose $\tilde\kappa$ such that the LSP mass is set to 40 GeV and show the relic density and the pseudoscalar mass m_{A_1} color coded as a function of the remaining free parameters μ and λ. The SFitter set up makes sure that the algorithm focuses on the parameter space that generates the correct relic density.

We observe a broad band in the $\lambda - \mu$ plane, which is defined by non-zero values for the Higgs masses: for large $\mu \gg m_Z$ and $\lambda \to 1$ the mass of the lightest CP-odd scalar A_1 vanishes. This follows from the singlet mass term in pseudoscalar mass matrix in Eq. (3.43): Replacing $\tilde\kappa\mu$ by the leading term in Eq. (3.45), the pseudoscalar mass mainly depends on μ and λ via A_κ. When A_κ increases, the mass of the pseudoscalar approaches zero. At the scale of the averaged squark masses A_κ is of the order of 100 GeV. Following the scale dependence in Eq. (5.4), an increase of λ and A_λ, leads to an increase of A_κ. As A_λ increases with μ following Eq. (3.42), higher values of μ and λ lead to smaller pseudoscalar mass consistent with the observed behavior.

The mass of the lightest CP-even scalar H_1 is given by the $(3,3)$ entry of the Higgs mass matrix in Eq. (3.40) in the Higgs decoupling limit Eq. (3.42),

$$M_{H,h,S}^2\Big|_{33} = m_Z^2\left(\frac{\lambda^2}{g^2}\left(1 - s_{2\beta}\tilde\kappa\right) + \frac{\tilde\kappa\mu}{m_Z^2}\left(A_\kappa + 4\tilde\kappa\mu\right)\right) . \tag{5.6}$$

A_κ enters here with a positive sign, so that for small $\mu \lesssim m_Z$ and $\lambda \to 0$ the mass of this CP-even singlet vanishes. Possible experimental constraints are expected to further reduce this band [162].

Within this broad band shown in the upper panels of Fig. 5.2 the structure originates from two sets of input parameters to the calculation of the relic density. On the one hand there is a strong dependence on the mass of the pseudoscalar mediator, on the other hand the couplings of the LSP depend on the gaugino and Higgsino content of the LSP.

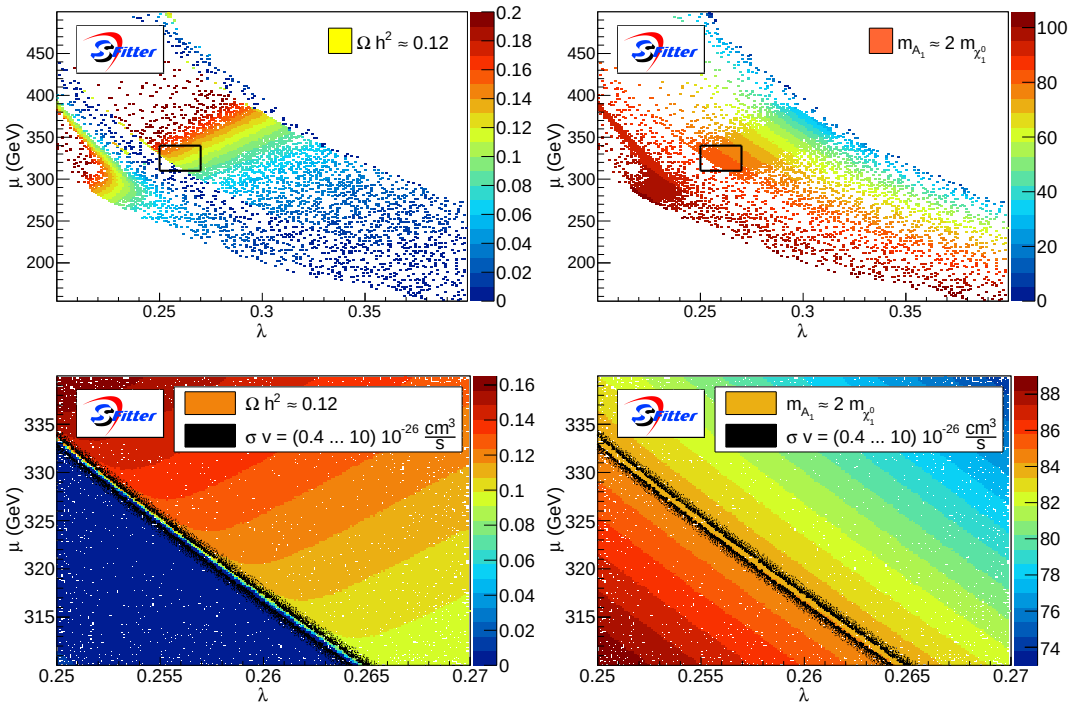

Figure 5.2: Neutralino relic density (left) and mass of the light pseudoscalar A_1 (right) color-coded as a function of μ and λ. The two lower panels are zoomed into the respective upper panels.The legend indicates the color range for which the predicted relic density and annihilation cross section respectively agree with the measurements. The orange regions in the lower left panel are compatible with the relic density $\Omega_{\tilde{\chi}} h^2 = 0.107 \ldots 0.131$, considering the theoretical uncertainty. In addition to the usual decoupling through large scalar masses we fix $\tan\beta = 40$, $A_\kappa = -250$ GeV, A_λ according to the decoupling condition Eq. (3.42), and $\tilde{\kappa}$ corresponding to an LSP mass of 40 GeV through Eq. (3.45).

In the upper part of the band, with $m_{A_1} < 80$ GeV and $0.26 < \lambda < 0.3$ the dark matter annihilation is mediated by the Z-funnel, with a coupling to the Higgsino content proportional to $N_{13}^2 - N_{14}^2$ as given in Eq. (3.33). Smaller values of the coupling of λ, correlated with large values of the Higgsino mass parameter μ, decouple the singlet/singlino sector from the MSSM. An efficient dark matter annihilation is not possible, and the relic density is too large. On the other hand, too small values of μ and large λ increase the Higgsino–singlino mixing via the off-diagonal terms in the neutralino mass matrix. The Higgsino component of the LSP then results in too small a relic density. Between these two regions, Fig. 5.2 indicates a well-defined regime with the correct relic density. The corresponding mass of the lightest pseudoscalar A_1

indicates that the resonance condition $m_{A_1} \approx 2m_{\tilde{\chi}}$ is only fulfilled at the lower end of this regime, while the larger part of the allowed band relies on Z-mediated dark matter annihilation.

In the lower part of the band, defined by the onset of the resonance condition $m_{A_1} \lesssim 2m_{\tilde{\chi}}$, a steep decrease of the relic density leaves a very narrow strip where the annihilation proceeds via the A-funnel and reproduces the correct value of $\Omega_{\tilde{\chi}} h^2$. With the increasing A-funnel contribution, the Z-mediated annihilation rate has to decrease, which means that the allowed region bends towards larger values of μ. The moment the resonance condition is actually fulfilled, the annihilation through the A-funnel becomes too efficient, and the predicted relic density drops well below the measured value. For $m_{A_1} \approx 90$ GeV, corresponding $\lambda < 0.24$ and $\mu \approx 300$ GeV, the annihilation again proceeds off-shell, predicting the correct relic density starting with a reduced Z-mediated rate at large μ. At $\lambda \approx 0.225$ and $\mu \approx 275$ GeV the annihilation is again mediated by the Z-boson alone.

A few hardly visible points with the correct relic density at the very top of the allowed mass band arise from H_1-funnel annihilation and will be of no relevance to our further discussion, because the scalar mediator with its p-wave suppression fails to explain the GC excess.

The lower panels of Fig. 5.2 focus on A_1-funnel annihilation just below the resonance condition. There are two regions separated by the widths of the pseudoscalar where the annihilation cross section is compatible with the galactic center excess — within a comparably broad range of $\sigma v = (0.4 \ldots 10) \cdot 10^{-26} \mathrm{cm}^3/\mathrm{s}$. The region below the resonance condition $m_{A_1} \lesssim 2m_{\tilde{\chi}}$ is compatible with the relic density, while the other one is not. The difference lies once again in the velocity dependence of the annihilation in the early Universe. For $m_{A_1} < 2m_{\chi_1}$ the annihilation via the A–funnel is strongly suppressed by the difference of the masses squared leading to a rapid change in the annihilation cross section. For $m_{A_1} > 2m_{\chi_1}$ the on–shell condition can still be fulfilled for a suitable relative velocity leading to a smaller relic density for same mass difference $\left|m_{A_1} - 2m_{\chi_1}\right|$, while the annihilation cross section today is symmetric around the pole. A simultaneous fit of relic density and the required annihilation cross section in the GC hence relies on a pseudoscalar mass below the on-shell condition.

5.2.2 Invisible Higgs decays

A contribution of invisible Higgs decays to the Higgs width has long been in the focus of collider studies and can be tested in two ways. First, they can be searched for directly, i. e. in the on-shell production of a SM-like Higgs boson with a decay to missing transverse energy. The most promising channel is weak boson fusion Higgs production [220, 221], which during the run time of the LHC should be sensitive to invisible branching ratios around 3% [171]. Current 95% C.L. limits on this invisible branching ratio are 57% in the WBF channel from CMS [227–233] and 78% combining associated Higgs production and gluon fusion from ATLAS [224–226] [†] .

[†] Since the publication of the corresponding paper, the measurements have known significant improvements leading to upper limits of 25% in an ATLAS combination of search channels targeting WBF and associated Higgs production [259] and 24% in the CMS combination of gluon fusion, WBF and associated Higgs production [260].

These analyses assume that the production rate of the SM-like Higgs boson is the same as in the Standard Model. Alternatively, we can include invisible Higgs decays in a global Higgs couplings analysis. In this case, all Higgs couplings are allowed to fluctuate around their Standard Model values. An SFitter combination of ATLAS and CMS measurements gives $\text{BR}_{\text{inv}} = 0.16^{+0.07}_{-0.11}$ [42] from a fully frequentist analysis of eight Higgs couplings. This corresponds to $\text{BR}_{\text{inv}} < 30.6\%$ at 95% C.L. For a dedicated NMSSM fit this limit is expected to be even more constraining. Because we are interested in the correlation of the GC excess with large invisible branching ratios of the SM-like Higgs we will not apply these limits in our analysis.

Usually, such invisible Higgs decays are associated for example with a Higgs portal to a scalar dark matter sector [235–250]. We will show that in the NMSSM, invisible Higgs searches can also probe a relevant part of the dark-matter-related parameter space through the decay $H_{125} \to \tilde{\chi}\tilde{\chi}$. Because this decay requires relatively light LSP neutralinos these scenarios can be linked to the GC excess discussed in Sec. 3.1.3.

The decay width of the CP-even Higgs into two neutralinos is given by

$$\Gamma(H_{125} \to \tilde{\chi}\tilde{\chi}) = \frac{m_{H_{125}}}{16\pi}\, g^2_{H_{125}\tilde{\chi}\tilde{\chi}}\, \Lambda^{3/2}\,, \qquad \text{with} \quad \Lambda = 1 - \frac{4m^2_{\tilde{\chi}}}{m^2_H}\,. \tag{5.7}$$

The Higgs–LSP coupling in the MSSM is

$$\begin{aligned} g_{H\tilde{\chi}\tilde{\chi}}\Big|_{\text{MSSM}} &= (g_1 N_{11} - g_2 N_{12})\ (\sin\alpha N_{13} + \cos\alpha N_{14}) \\ &\equiv (g_1 N_{11} - g_2 N_{12})\ (S_{21} N_{13} - S_{22} N_{14})\ . \end{aligned} \tag{5.8}$$

The N_{1j} are the entries of the neutralino mixing matrix, and S_{2i} are the entries of the CP-even Higgs mixing matrix. In the simple (2×2) case the latter are expressed in terms of the mixing angle α. In the MSSM invisible Higgs decays have to be mediated by gaugino and Higgsino fractions combined, or more specifically by a mixed bino–Higgsino LSP. In the NMSSM this coupling receives additional contributions from the singlet, namely

$$g_{H\tilde{\chi}\tilde{\chi}} = g_{H\tilde{\chi}\tilde{\chi}}\Big|_{\text{MSSM}} + \sqrt{2}\lambda\left[(S_{21}N_{14} + S_{22}N_{13})N_{15} + S_{23}N_{13}N_{14} - \tilde{\kappa}S_{23}N^2_{15}\right]\ . \tag{5.9}$$

Now, invisible Higgs decays can proceed to bino–Higgsino, singlino–Higgsino, and in the presence of a singlet component in the Higgs boson even pure Higgsino and pure singlino LSPs.

Just like the GC excess, invisible decays of the SM-like Higgs benefit from a light, mixed neutralino LSP. Decoupling squarks, sleptons, and gluino we can ask if there are regions with a large branching ratio $H_{125} \to \tilde{\chi}\tilde{\chi}$ for a mixed bino–Higgsino–singlino LSP, and such parameter regions can be related to the GC excess.

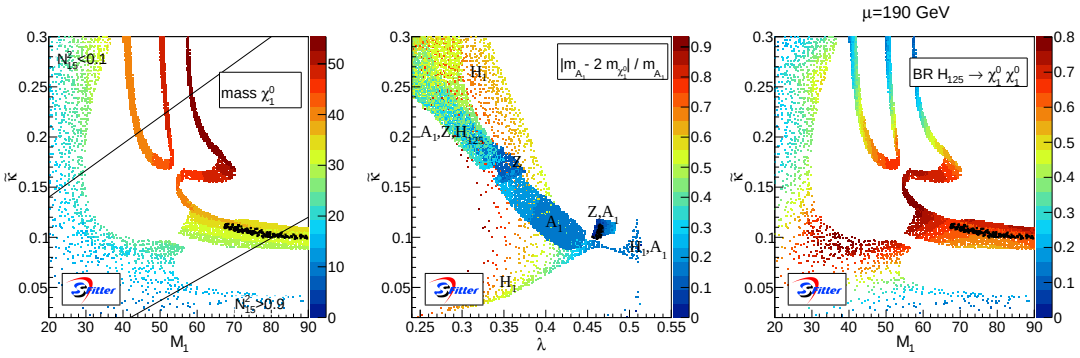

Figure 5.3: From left to right we show the LSP mass, the mass splitting between the LSP and the pseudoscalar mediator, and the invisible Higgs branching ratio with $\mu = 190$ GeV and $A_\kappa = -250$ GeV in the $\tilde{\kappa} - M_1$, $\tilde{\kappa} - \lambda$, and $\tilde{\kappa} - M_1$ planes. All displayed points are compatible with the relic density, Xenon, a chargino mass above 103 GeV, and the correct SM-like Higgs mass. Moreover, they always have an invisible branching ratio BR($H_{125} \to \tilde{\chi}\tilde{\chi}$) > 10%. The black points are consistent with the GC excess.

Following Eq. (3.45) the mass of the singlino LSP is given by $2\mu\tilde{\kappa}$. To suppress the Higgsino component we require $\tilde{\kappa} < 1/2$ and keep $\mu > 190$ GeV in a first step. This way the Higgsino component in the LSP ranges around 5% to 10%, leading to a sizable coupling to the Higgs sector but preventing a large coupling to the Z-boson. Our choice of parameters for the GC excess fixes $\tan\beta = 40$ and $A_\kappa < -250$ GeV. The decoupling condition Eq. (3.42) determines A_λ to minimize the singlet component of the SM-like Higgs. The remaining parameters are $\lambda, \tilde{\kappa}$ and M_1. Small values of M_1 increase the bino component of the LSP while small values of $\tilde{\kappa}$ increase the singlino component. To keep a constant neutralino mass, $\tilde{\kappa}$ and M_1 have to behave inversely proportional.

In Fig. 5.3 we show the result of the SFitter analysis, starting with fixed $\mu = 190$ GeV. Of the experimental constraints discussed in Sec. 5.2 we now only include the relic density, the Xenon constraints, the chargino mass constraints, the invisible Z-width constraint $\Gamma_{Z\to\text{inv}} < 1$ MeV [170], and the SM-like Higgs mass constraint $m_H = 122 \ldots 128$ GeV. We only show parameter points with BR($H_{125} \to \tilde{\chi}\tilde{\chi}$) > 10%. For our starting value $\mu = 190$ GeV we fix $A_\kappa = -250$ GeV.

Three distinct, narrow strips in the left panel of Fig. 5.3 are defined by constant LSP masses around 40 GeV, 48 GeV, and 55 GeV. For $m_{\tilde{\chi}} \approx 55$ GeV the annihilation is mediated by H_{125}. If the mass moves closer to the H_{125} on-shell condition the relic density becomes too small. At the lower end of the 55 GeV strip the additional annihilation through the A_1 pseudoscalar and the Z becomes too strong to reproduce the observed relic density. Numerically, the reason is that $m_{A_1} \propto \tilde{\kappa}$ reaches 120 GeV around $\tilde{\kappa} = 0.16$, which opens a pseudoscalar-mediated LSP annihilation channel. For $\mu = 190$ GeV this coincides with the possibility to efficiently annihilate

though an s-channel Z-exchange.

The 40 GeV and 48 GeV strips are defined by the Z-mediated LSP annihilation. Each of them lives on one side of the Z-pole, because the annihilation on the pole is too efficient to give the correct relic density. Both strips follow the asymptotic behavior of the LSP mass. The 40 GeV strip continues towards high values of M_1, but with a reduced LSP mass. The reason is that the additional annihilation mediated by A_1 adds to Z-mediated annihilation. Finally, the annihilation via the pseudoscalar connects the annihilation channels for $m_{\tilde{\chi}} = 48$ GeV and $m_{\tilde{\chi}} = 55$ GeV around $M_1 = 70$.

In the broad regions with $M_1 = 10 \ldots 40$ GeV the annihilation is in addition mediated by H_1 ($\tilde{\kappa} > 0.1$) and by a combination of H_1 and A_1 ($\tilde{\kappa} < 0.1$).

One key feature is the hole in the allowed parameter space around $\tilde{\kappa} = 0.15$ and $M_1 = 50$ GeV. For example along the 40 GeV strip the LSP composition changes from bino to singlino, with a 5% to 12% Higgsino contribution. While the sum of the two Higgsino components increases towards the singlino LSP, their ratio switches. This leads to an intermediate region where both components have a similar value. At this point $g_{Z\tilde{\chi}\tilde{\chi}}$ given by Eq. (3.33) vanishes, interrupting the Z-mediated annihilation. The other annihilation channels are weak, so the relic density is too large.

In the right panel of Fig. 5.3 we see that the parameter space which can account for the GC excess indicated by black points appear precisely where we also expect invisible decays for the SM-like Higgs H_{125}. Indeed, for $M_1 = 50 \ldots 60$ GeV and $\tilde{\kappa} \approx 0.1$ we find the highest branching ratio $H_{125} \to \tilde{\chi}\tilde{\chi}$. This region has unique properties: as discussed above, the dark matter annihilation in the early Universe proceeds through an on-shell Z-boson, with $m_{\tilde{\chi}} = 45 \pm 2$ GeV. The LSP is a mixed state with 8% Higgsino, 30% to 50% singlino, and 40% to 50% bino content. The two Higgsino components are of the same size, strongly reducing the Z-coupling $g_{Z\tilde{\chi}\tilde{\chi}}$. The lightest pseudoscalar A_1 has a mass around 115 to 135 GeV, but remains undetected due to its singlet content of at least 95%.. Because of the strongly mixed LSP content, each N_{1i} term can contribute to $g_{H_2\tilde{\chi}\tilde{\chi}}$. This large value induces an invisible branching ratio of up to[‡].

$$\text{BR}(H_{125} \to \tilde{\chi}\tilde{\chi}) \lesssim 70\% \qquad \text{for} \quad \mu = 190 \text{ GeV} , \tag{5.10}$$

for the parameter space consistent with the GC excess.

In this region with an overwhelming invisible Higgs decay width we need to check a few experimental constraints not represented in Fig. 5.3: First, the cancellation of the two Higgsino components renders the partial decay width $\Gamma_{Z\to\text{inv}}$ smaller than 0.1 MeV. For a mostly-singlino LSP region it increases through large N_{14} values up to 2 MeV. Second, the Xenon limits on direct dark matter detection exclude the region centered around $M_1 = 40$ GeV and $\tilde{\kappa} = 0.2$, linked to the H_1 and A_1 annihilation channels. However, none of these additional constraints affect the parameter regions with invisible Higgs branching ratios between 10% and 30%.

[‡]As mentioned above, in this discussion we ignore the limits on invisible Higgs decays of $\text{BR}_{\text{inv}} < 30.6\%$, for example from the SFitter Higgs analysis [42].

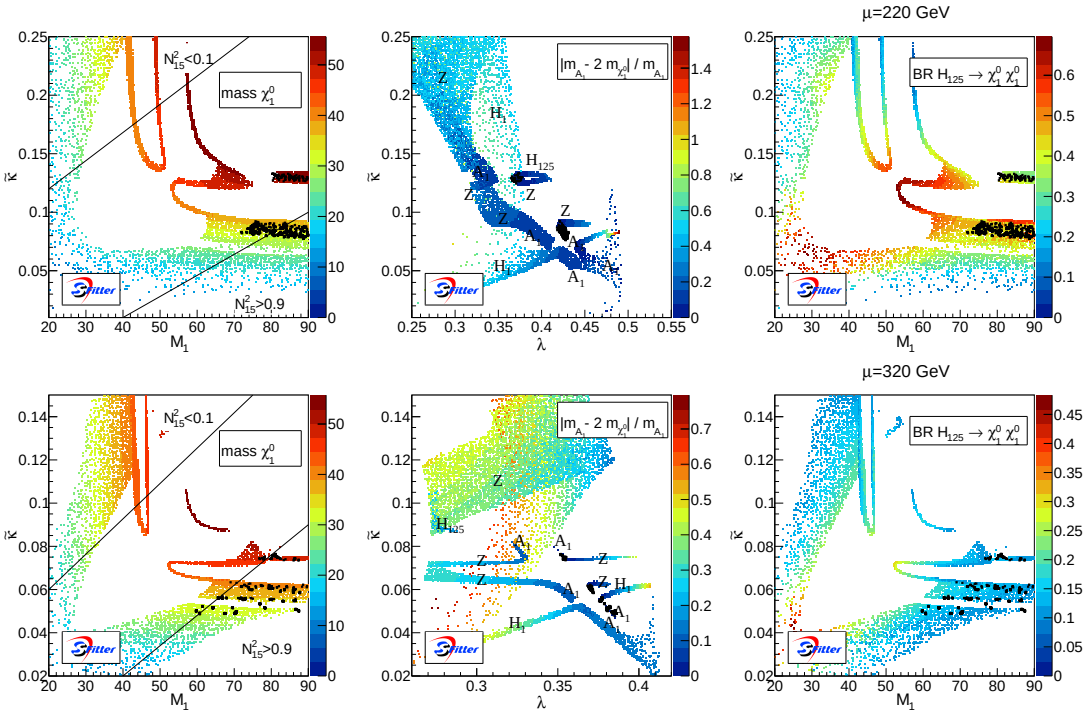

Figure 5.4: LSP mass, mass splitting between the LSP and the pseudoscalar mediator, and invisible Higgs branching ratio now for $\mu = 220$ GeV (upper row) and $\mu = 320$ GeV (lower row) in the $\tilde{\kappa}-M_1$, $\tilde{\kappa}-\lambda$, and $\tilde{\kappa}-M_1$ plane. Correspondingly we choose $A_\kappa = -280$ GeV and -380 GeV. As in Fig. 5.3 all displayed points are compatible with the relic density, Xenon, a chargino mass above 103 GeV, and the correct SM-like Higgs mass. Moreover, they always have an invisible branching ratio BR($H_{125} \to \tilde{\chi}\tilde{\chi}$) > 10%. The black points are consistent with the galactic center excess.

In the next step we vary μ, and with it A_κ to keep the singlet Higgs masses in the desired range. This means that for $\mu = 220$ GeV and $\mu = 320$ GeV we have to set $A_\kappa = -280$ GeV and $A_\kappa = -350$ GeV, respectively.

Increasing μ slowly impacts the LSP annihilation channels. We see that the allowed regions for $\mu = 220$ GeV shown in the upper left panel of Fig. 5.4 are very similar to the case of $\mu = 190$ GeV. This indicates that our above results are not very fine-tuned. For a fixed LSP mass an increase of μ merely leads to a smaller Higgsino component, which in turn leads to a smaller $Z\tilde{\chi}\tilde{\chi}$ coupling. It also decreases the invisible Higgs branching to

$$\text{BR}(H_{125} \to \tilde{\chi}\tilde{\chi}) \lesssim 40\% \qquad \text{for} \quad \mu = 220 \text{ GeV}\,, \tag{5.11}$$

in the relevant parameter region for the GC excess.

For larger $\mu = 320$ GeV the picture changes: for a fixed LSP mass an increase of μ leads to a even smaller Higgsino content. While for $\mu = 190$ GeV the two Higgsino components add to 5% ... 17%, they now stay in the 2% ... 5% range. This immediately leads to a smaller $Z\tilde{\chi}\tilde{\chi}$ coupling — and a reduced invisible Higgs branching ratio. The $Z\tilde{\chi}\tilde{\chi}$ coupling implies that the LSP mass has to be closer to the on-shell condition to give the correct relic density. Indeed, for a bino-like LSP and $\mu = 320$ GeV, the lowest mass strip is now defined by $m_{\tilde{\chi}} \approx 42$ GeV instead of 40 GeV. Similarly, the high-mass strip moves down from $m_{\tilde{\chi}} = 48$ GeV to 46 GeV. Altogether, in the lower left panel of Fig. 5.4 we see that the annihilation regions mediated by the Z-funnel and the H_1 funnel with $m_{\tilde{\chi}} = 55$ GeV clearly separate.

The annihilation processes can now best be identified in the central lower panel of Fig. 5.4, showing the correlation between $\tilde{\kappa}$ and λ. Annihilation through a Z-boson occurs in the two parallel strips with $\tilde{\kappa} \approx 0.065$ and $\tilde{\kappa} \approx 0.07$. They are divided by the actual on-shell condition $2m_{\tilde{\chi}} = m_Z$, for which LSP annihilation becomes too efficient.

Following Eq. (3.40) and replacing A_λ through Eq. (3.42) we see that the H_1 mass increases with λ directly, as well as indirectly via A_κ. Larger values of λ lead to a steeper increase of the scale dependence and thereby increases A_κ at the 10 TeV scale. At the same time the neutralino mass increases with $\tilde{\kappa}$. This explains why for an annihilation via H_1 we find a strip increasing from $\tilde{\kappa} \approx 0.02$ and $\lambda \approx 0.24$ to $\tilde{\kappa} \approx 0.06$ and $\lambda = 0.4$

As always, for the GC excess the annihilation via the pseudoscalar A_1 given by Eq. (5.5) is crucial. The LSP mass decreases with κ, while the mediator mass m_{A_1} decreases with λ. This is caused by the renormalization group running of the parameters, which for larger λ pushes A_κ to larger values at 10 TeV. Following Eq. (3.43) the pseudoscalar mass includes a factor $-A_\kappa$, which means it indeed decreases with increasing λ. To maintain the relation between the LSP and mediator masses, λ and $\tilde{\kappa}$ have to be anti-correlated. This is what we observe in the two A_1-mediated strips in the central lower panel of Fig. 5.4. These strips with the efficient pseudoscalar mediator also accommodate the GC excess, as expected from the simplified model analysis [163, 180, 181]. Again, as before the A_1-mediated annihilation blends in with Z-mediated annihilation.

For $\mu = 320$ GeV we find an increasingly small number of parameter points which accommodate the GC excess as well as the current relic density. However, they reside in a regime with

$$\text{BR}(H_{125} \to \tilde{\chi}\tilde{\chi}) \lesssim 15\% \qquad \text{for} \quad \mu = 320 \text{ GeV} , \tag{5.12}$$

again consistent with the GC excess. One aspect which becomes relevant when we embed the NMSSM in a unified framework at the GUT scale is the M_1-dependence of the GC-compatible parameter points. For all three μ-values we observe a tail towards large M_1 values, for which the LSP properties do not change any longer. While we do not show values above $M_1 > 90$ GeV, we could extend the curves to much larger bino masses.

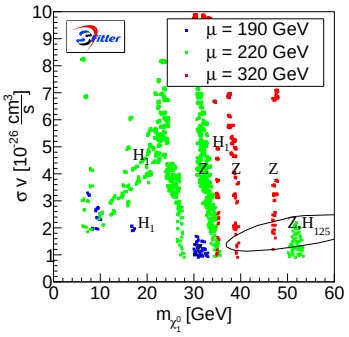

Figure 5.5: Correlation between the LSP mass and the dark matter annihilation rate for our three reference points in μ, to be compared to for example Fig. 3 in Reference [100]. The ellipse corresponds to the two sigma limits there. If available, we indicate the leading LSP annihilation channels. Points with $m_{\tilde{\chi}} < 30$ GeV shown in this figure are not included in our analysis in Figs. 5.3 and 5.4.

For a combination of the different μ values assumed in the above analysis we show the two-dimensional correlations between the LSP mass and the annihilation rate in Fig. 5.5. The displayed points fulfill all previously applied constraints including limits from direct detection and measured the relic density within the theory uncertainty. Moreover we require a minimal annihilation cross section at the GC within the range of Eq. (5.2). The valid NMSSM parameter points include LSP masses below 30 GeV, which we do not consider in our analysis of the invisible branching fractions [86–100]. We see that most of the NMSSM points would prefer a larger annihilation rate than the central value of the ellipse, but this annihilation rate can be accommodated by moving the different masses slightly on and off the respective resonance conditions. Moreover, the majority of allowed points have LSP masses between 10 and 30 GeV, in particular for $\mu = 220$ GeV. On the other hand, for all three values of μ it is possible to enter the preferred region taken from Reference [93, 97, 100] in the two-dimensional σv vs $m_{\tilde{\chi}}$ plane.

5.3 High-scale NMSSM

5.3.1 Global analysis

From the previous discussion it is clear that there are several, more or less distinct regions of the NMSSM parameter space, which allow us to describe the GC excess consistent with constraints from direct detection and collider searches. This is less clear when we constrain the model parameters through unification assumptions.

Before we focus on the GC excess and invisible Higgs decays, it makes sense to test how well the unified NUH-NMSSM can accommodate all other available data listed in Tab. 5.1, including

the observed relic density and the Xenon limits on direct detection. We also include the SM-like Higgs couplings strengths from the SFitter-Higgs analysis [19, 40, 41]. Our parameters of interest are λ, $\tilde{\kappa}$, and μ.

In the NUH-NMSSM with decoupled scalars ($m_0 = 2$ TeV) we face two major differences compared to the TeV-scale model. First, unification links the binos mass M_1 to the gluino mass, which is constrained by direct LHC searches [261]. Second, the SUSY-breaking singlet parameters A_λ and A_κ are set at the GUT scale. This means that we cannot apply the simple decoupling relations for example given in Eq. (3.42).

To get some control over the parameters we start with an SFitter likelihood analysis, to see how the requirement $H_2 = H_{125}$ translates into the high-scale parameters $A_\lambda, A_\kappa, m_{1/2}$, and A_0. The unified gaugino mass is proportional to the gluino mass and hence constrained to be $m_{1/2} \gtrsim 500$ GeV. The mass scales A_λ and A_κ will eventually be constrained by the requirement of a light scalar mass, and we fix their ranges to $A_\kappa = -1.5\ldots1.5$ TeV and $A_\lambda = -1\ldots5$ TeV. From our experience with the TeV-scale NMSSM we limit the singlet parameters, still defined at 1 TeV, to $\lambda < 1$, $\kappa < 1$, and $\mu < 400$ GeV. The ratio of the VEVs is fixed again to $\tan\beta = 40$.

As before, we use all data listed in Tab. 5.1. In the Higgs sector we identify the observed SM-like Higgs with the second-lightest NMSSM Higgs and include the Higgs couplings measurements from ATLAS and CMS searches [19, 40, 41]. A set of two-dimensional profile likelihood projections is displayed in Fig. 5.6.

	1	2	3	4	5
μ[GeV]	190	220	220	320	320
M_1[GeV]	80.07	94.09	81.59	89.87	84.28
λ	0.462	0.370	0.423	0.370	0.377
$\tilde{\kappa}$	0.112	0.129	0.091	0.062	0.056
$m_{\tilde{\chi}}$[GeV]	33.96	52.69	35.80	39.47	35.72
m_{H_1}[GeV]	61.89	50.35	61.72	74.80	76.98
m_{A_1}[GeV]	64.34	104.36	70.02	78.62	71.00
$\Gamma(Z \to \tilde{\chi}\tilde{\chi})$[MeV]	0.69	0.00	0.27	0.02	0.05
BR($H_{125} \to \tilde{\chi}\tilde{\chi}$)	0.68	0.30	0.51	0.11	0.12
$\sigma(\tilde{\chi}\tilde{\chi} \to b\bar{b})/\sigma_{\text{ann}}$	29%	48%	34%	39%	21%
$\sigma(\tilde{\chi}\tilde{\chi} \to s\bar{s})/\sigma_{\text{ann}}$	12%	8%	11%	11%	2%
$\sigma(\tilde{\chi}\tilde{\chi} \to c\bar{c})/\sigma_{\text{ann}}$	10%	6%	9%	8%	68%

Table 5.2: NMSSM benchmark points, in agreement with all experimental constraints with the exception of invisible Higgs decays. For the annihilation channels to the observed relic density we show the final states, because the mediators can interfere.

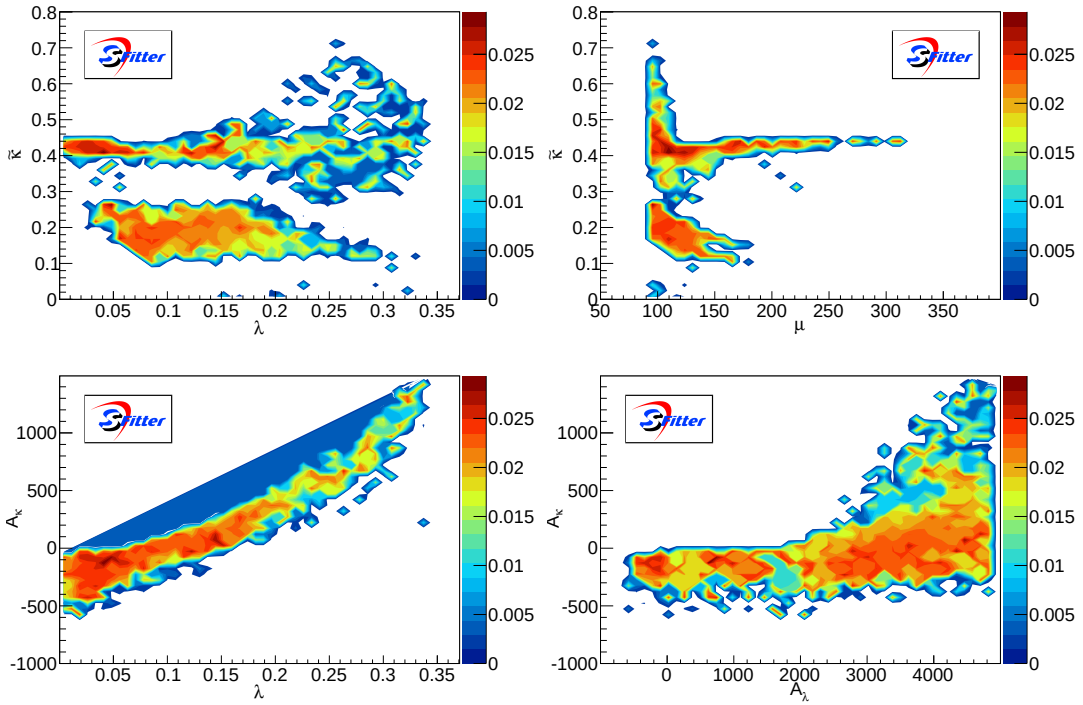

Figure 5.6: Profile likelihood projections of the NUH-NMSSM assuming a SM-like $H_2 \equiv H_{125}$. The color–scale indicates $-2\Delta(\log \mathcal{L})$. All measurements shown in Tab. 5.1 and the SM-like Higgs couplings [19, 40, 41] are included. Of the shown parameters A_κ, and A_λ are defined at the GUT scale. The singlet parameters $\lambda, \tilde{\kappa}$ and μ are defined at 1 TeV, just like in the low scale scenario.

The upper left panel shows the profile likelihood projection on the $\tilde{\kappa} - \lambda$ plane. We identify three distinct regions through their dark matter annihilation channels [39]:

1. a broad band with $\tilde{\kappa} = 0.1 \ldots 0.3, \lambda < 0.25$, and $\mu = 90 \ldots 200$ GeV. It includes two LSP mass regions with an annihilation through Z- and H_{125}-exchange.
2. a narrow strip around $\tilde{\kappa} \approx 0.42, \lambda < 0.2$, and $\mu = 90 \ldots 350$ GeV. It relies on a light chargino either for co-annihilation or for t-channel exchange for efficient dark matter annihilation.
3. a bulk region with $\tilde{\kappa} = 0.3 \ldots 0.7, \lambda > 0.2$, and $\mu = 90 \ldots 150$ GeV. Here, the annihilation occurs through a mix of channels, notably including the light singlet pseudoscalar.

The transition between the second and third region is not uniquely defined, but involves the appearance of the A_1-funnel annihilation and a drop in the LSP singlino content from 70% … 90% to 10% … 70%. Following Sec. 5.2.2, an invisible branching ratio needs a LSP mass smaller than 62 GeV. Therefore the only region compatible with the GC excess and an invisible branching ratio will be $\tilde{\kappa} = 0.1 \ldots 0.25$.

The upper right panel in Fig. 5.6 shows the profile likelihood projection on the $\tilde{\kappa} - \mu$ plane. A lower bound $\mu > 90$ GeV arises from the chargino mass limit. An upper bound is connected to the requirement that the second-lightest NMSSM Higgs be the SM-like state: the mass of the singlet-like Higgs is proportional to μ, so for large μ it approaches 125 GeV. This translates into the globally observed $\mu < 400$ GeV.

We then combine the range in μ with the $m_{1/2}$ dependence. As mentioned before, the gluino bound sets a lower limit on $m_{1/2} > 500$ GeV. The combination of $\mu < 400$ GeV and $m_{1/2} > 500$ GeV results in a sum of the bino and wino LSP components to be less than 1% throughout the plane. The mass and composition of the Higgsino-singlino LSP is set by $\mu, \tilde{\kappa}$, and λ. For $\tilde{\kappa} > 0.5$ it is mainly Higgsino, with its mass set by μ. For $\tilde{\kappa} < 0.4$ the LSP is mainly singlino, and following Eq. (3.45) its mass is given by $2\tilde{\kappa}\mu$. Large values of λ lead to a stronger mixing between singlino and Higgsino.

Of the list of regions introduced above we first consider the band with $\tilde{\kappa} = 0.1 \ldots 0.3$, where the singlino component is larger than 85%. The corresponding values of μ range from 90 GeV to 200 GeV, resulting in two regions of neutralino mass compatible with the measured relic density: for $m_{\tilde{\chi}} = 40 \ldots 50$ GeV the annihilation is mediated by a Z-boson, while for $m_{\tilde{\chi}} = 55 \ldots 60$ GeV the LSP annihilates via the SM-like Higgs into $b\bar{b}$ and partially into light Higgs bosons. Annihilation via the lightest pseudoscalar, as relevant for the GC excess can occur, but it is not a main annihilation channel.

In the narrow second strip, the higher value of $\tilde{\kappa} = 0.42$ leads to a smaller Higgsino component, that varies between 70% and 90%. The higher value of $\tilde{\kappa}$ leads to a mass ratio of about 0.85 between the LSP and the Higgsino-like chargino. This opens the chargino co-annihilation channel or neutralino annihilation into WW and ZZ through a chargino in the t-channel. In the upper right panel we can verify that this channel is open up to $\mu = 350$ GeV.

Finally, for $\lambda > 0.2$ the different annihilation processes are no longer well separated. Inversely correlated to $\tilde{\kappa} = 0.3 \ldots 0.7$ the singlino component decreases from 70% to 10%. For this region we find an upper bound of $\mu < 150$ GeV, resulting in neutralino masses between 60 and 100 GeV. For neutralinos around 60 GeV the annihilation proceeds via the SM-like Higgs, while for larger masses the annihilation channel is a mixture of a pseudoscalar funnel, chargino co-annihilation, and t-channel annihilation via a chargino.

The lower panels of Fig. 5.6 show the profile likelihood projection onto the $\lambda - A_\kappa$ and the $A_\lambda - A_\kappa$ planes. From Eq. (3.40) and Eq. (3.43) we know that the scalar and pseudoscalar singlet mass terms increase with λ. The singlet-like scalar has to remain lighter than 125 GeV, leading to an upper limit on λ depending on A_κ and A_λ. Large values of A_κ can either push the scalar mass to too large values or lead to a vanishing pseudoscalar mass. Both effects set an upper limit on A_κ. Because A_κ is set at the GUT scale, small starting values of A_κ can turn negative towards the TeV scale, leading to a very light scalar. The correlation between λ and A_κ occurs because for large λ we need larger values of A_κ to keep the pseudoscalar singlet heavy enough.

In the right panel we see that large values of A_κ are only possible for even larger values of A_λ.

The scalar and the pseudoscalar singlet mass-squares differ by $\Delta m^2 = 4(A_\kappa \tilde{\kappa}\mu + \tilde{\kappa}^2\mu^2)$, neglecting the subleading term proportional to $m_Z^2 s_{2\beta}\lambda^2\tilde{\kappa}$. For both, the scalar and the pseudoscalar masses to be above zero, this mass difference cannot be larger than the actual mass scale. This means that large A_κ has to be accompanied by even larger A_λ.

5.3.2 Galactic center excess

In the TeV-scale NMSSM a singlino-like LSP with a small Higgsino component can generate the GC excess in agreement with the relic density and linked to an enhanced branching ratio $H_{125} \to \tilde{\chi}\tilde{\chi}$. By definition, the NUH-NMSSM contains only a subset of the NMSSM models: the unification condition on $m_{1/2}$ impacts the range of M_1, and the stop masses can no longer be set independently of the remaining sfermion masses.

To be consistent with the TeV-scale study we decouple the sfermion sector at $m_0 = 10$ TeV and set $\tan\beta$ to 40. This is compatible with the observed Higgs mass, when we adjust A_λ accordingly. As before, μ is set at the SUSY scale of 1 TeV and limited to (150 … 220) GeV which will be compatible with the GC excess. To generate a singlino mass around 40 to 50 GeV, we vary $\tilde{\kappa} = 0.06 \ldots 0.18$, following Eq. (3.45).

As mentioned in the previous section, gaugino mass unification correlates the bino, wino, and gluino masses. Direct gluino searches set a lower limit of $m_{1/2} > 500$ GeV [261]. This leads to a heavy wino mass, out of reach for LEP2, and defines a lower bound $M_1 > 200$ GeV. Both, the bino and wino components of the lightest neutralino become negligible. To compensate for the missing bino component, the Higgsino component needs to be slightly enhanced with respect to the TeV-scale model, leading to the slightly reduced values of μ quoted above.

In the TeV-scale case we fix A_λ using Eq. (3.42). In the NUH-NMSSM this is no longer possible, as A_λ is now defined at the averaged squark mass scale, where also the Higgs masses are computed. We can estimate that for $\mu = 200$ GeV the value of A_λ at 10 TeV has to be approximately 8 TeV. Neglecting all contributions but A_λ itself in Eq. (3.54), the value of A_λ increases to around 8.6 TeV when evaluated at the GUT scale. From the global analysis we know that A_κ tends to have the same sign as A_λ. In this case, A_κ further increases the preferred value of A_λ at the GUT scale to around 9 TeV. This fixed value of A_λ now translates into preferred ranges of A_κ and λ via the singlet scalar and pseudoscalar squared mass terms, which need to be larger than zero. Choosing $\lambda = 0.25 \ldots 0.45$ gives $A_\kappa = (1.5 \ldots 5)$ TeV.

In Fig. 5.7 we show the results of our SFitter analysis. Just as in the TeV-scale study, we require all points to be compatible with direct detection limits, Higgs mass measurements, and the relic density within the theoretical uncertainty, as given in Tab. 5.1. The chargino masses have to be larger than 103 GeV and the additional contribution to the Z-width smaller than 1 MeV. All displayed points are consistent with an invisible branching ratio of at least 10%.

As mentioned before, we now study singlino LSPs with a small Higgsino component. On the left hand side of Fig. 5.7 we show the projection onto the $\tilde{\kappa} - \mu$ plane. This determines the

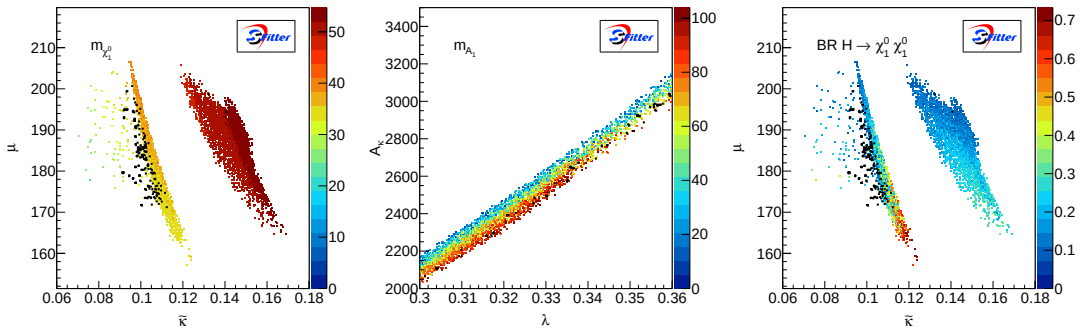

Figure 5.7: LSP mass, pseudoscalar mediator mass, and invisible Higgs branching ratio in the NUH-NMSSM. As before, we fix $\tan\beta = 40$. Like in Fig. 5.3 all displayed points are compatible with the relic density, Xenon, a chargino mass above 103 GeV, and the correct SM-like Higgs mass. Moreover, they always have an invisible branching ratio $\mathrm{BR}(H_{125} \to \tilde{\chi}\tilde{\chi}) > 10\%$. The black points are consistent with the galactic center excess.

mass and the composition of the LSP. For the singlino-like LSP the mass increases with μ and $\tilde{\kappa}$. The allowed region for larger $\tilde{\kappa}$ corresponds to an LSP mass of 50 to 52 GeV while the strip at $\tilde{\kappa} \approx 0.11$ corresponds to a neutralino mass of 30 to 40 GeV. In between the two regions, the annihilation via the Z-pole becomes too efficient. For larger masses the annihilation is too weak to predict the measured relic density. In contrast, towards smaller masses a combination of the A_1- and Z-channels gives the correct relic density as well as an annihilation cross section compatible with the GC excess.

Apart from its mass, the composition of the LSP plays a key role. For small $\tilde{\kappa} \approx 0.1$ the sum of the Higgsino components decreases with increasing μ, starting from 5% at $\mu = 205$ GeV and reaching 20% for $\mu = 160$ GeV. This increased active Higgsino component implies a larger coupling to the Higgs, which leads to an increase of the invisible branching ratio: for $\mu < 160$ GeV it can reach up to 80%, while for $\mu > 200$ GeV it drops below the required 10%. However, from the large coupling to the Z there follows a negligible annihilation via the pseudoscalar mediator, rendering this region in-compatible with the GC excess. Moreover, direct detection limits become relevant for a large Z-coupling and exclude points with smaller values of μ.

In the center panel, we show the $A_\kappa - \lambda$ plane for a reduced range of $\lambda = 0.30 \ldots 0.36$. This illustrates the dependence of the lightest pseudoscalar mass on A_κ and λ. From Eq. (3.43) now directly follows that the A_1-mass increases with λ, while it decreases with A_κ. Once A_κ becomes too large, the pseudoscalar mass squared crosses zero, limiting the allowed region. For the galactic center excess σv only reaches sufficiently high values around the on-shell condition for the A_1 funnel. From the discussion of the $\tilde{\kappa} - \mu$ plane we know that the mass range for neutralinos compatible with the GC excess is restricted to $m_{\tilde{\chi}} = 30 \ldots 48$ GeV. This translated

into pseudoscalar masses of 60 to 100 GeV.

In the right panel of Fig. 5.7 the projection on the $\tilde{\kappa} - \mu$ plane shows the resulting branching ratio for invisible Higgs decays. For the region around $\tilde{\kappa} \approx 0.15$, λ ranges from 0.25 to 0.3, while for $\tilde{\kappa} \approx 0.11$ the allowed range for λ increases up to 0.45 for $\mu = 160$ GeV. Small values of λ result in a small Higgsino component, leading to an invisible branching ratio of 10 to 30% in the region with $m_{\tilde{\chi}} \approx 50$ GeV. For the narrow region the lower limit of $\mu = 155$ GeV in combination with large values of λ allow for large invisible branching ratios up to 70%.

When we consider only points compatible with the GC excess we find

$$\text{BR}(H_{125} \to \tilde{\chi}\tilde{\chi}) \lesssim 40\% \qquad \text{for} \quad \mu = 170 \ldots 200 \text{ GeV} . \tag{5.13}$$

The maximal found branching ratio of 40% is comparable to the results for $\mu = 220$ GeV in the TeV scale NMSSM where the bino component enhances the coupling. Even though the NUH-NMSSM pushes the neutralino content to a pure singlino-Higgsino state, we can still find regions that are compatible with the relic density, the GC excess and a strongly enhanced invisible branching ratio.

5.4 Conclusion

A natural explanation of the Fermi GC excess is a light, weakly interacting dark matter particle decaying to a pair of bottom quarks through an s-channel pseudoscalar. The NMSSM is one of the few models which predict precisely this process.

In the NMSSM framework, the GC excess as well as the currently observed relic density can be accommodated with the help of Z-funnel and A_1-funnel annihilation [173–178]. Different preferred parameter spaces can be linked to LHC searches for trileptons [186, 187] or exotic Higgs searches [162]. We show that for a mixed bino–singlino–Higgsino LSP the explanation of the GC excess typically predicts large invisible branching ratios of the SM-like Higgs boson. In particular for small μ values the invisible branching ratios can reach 50%, testable with Run I Higgs data. Future LHC analyses, sensitive to invisible branching ratios around 3% [171], cover a large fraction of Higgs decays to a pair of dark matter particles compatible with the GC excess. The preferred NMSSM parameters at the TeV scale can also be realized in a unified version of the NMSSM, albeit with larger values of M_1 and slightly reduced μ.

Chapter 6

Limits from a combined TGV and Higgs EFT analysis

The direct exploration of the electroweak symmetry breaking sector started with the discovery of a light narrow Higgs boson [11–13] in 2012 [14, 15] — a triumph of particle physics. Already the LHC Run I allowed ATLAS and CMS to perform a large number of tests of the nature of the observed resonance, but no significant deviations from the Standard Model properties were observed for example in the Higgs production and decay rates [42, 262–278]. On the other hand, it is important to remind ourselves that the current constraints are still at a precision level for which no significant deviations would be expected in weakly interacting models of new physics [279].

If we accept the Standard Model assumption that the Higgs particle is closely related to the massive gauge bosons, the Higgs results from Run I should be combined with corresponding precision measurements in the electroweak sector. During Run I the LHC collaborations have also collected meaningful event samples probing electroweak gauge boson pair production. They contain information on the structure of the TGVs and allow for complementary tests of the electroweak symmetry breaking mechanism.

The eventual observation of departures of Higgs or gauge boson couplings from their SM predictions can give hints about physics beyond the Standard Model, characterized by a new energy scale Λ, that affect the electroweak sector.

One way of parametrizing low–energy effects of SM extensions is by means of an effective Lagrangian [280–282], which only depends on the low–energy particle content and symmetries. This bottom–up approach has the advantage of minimizing the amount of theoretical assumptions when studying deviations from the SM predictions.

One result of this effective theory approach is that modified Higgs couplings to weak bosons are related to triple gauge boson vertices in a largely model independent fashion. This allows us to use Higgs data not only to constrain TGVs [297], but also to use TGV data to test the strengths and structures of Higgs couplings. Usually, such combined analyses rely on LEP results for the TGVs [298–305], the only exception being Reference [277, 278]. The reason is that LEP provided

the strongest constraints on TGVs until now. However, during the LHC Run I both ATLAS and CMS have collected a substantial amount of data on di-boson searches. It contains information on TGVs, whose relevance has not been addressed quantitatively. We fill this void with the very first state–of–the–art global analysis of the complete di-boson and Higgs data from the LHC Run I [*].

The outline of the chapter is as follows: after briefly reviewing the concept of EFT and the relevant set of operators in Sec. 6.1, we present details of our di-boson simulations and the results of our global analysis of the LHC Run I data on di-boson searches in Sec. 6.2. In Sec. 6.3 we find that the combined LHC Run I results are substantially stronger than the LEP constraints. Sec. 6.4 contains the combined analysis of di-boson and Higgs data, giving the up-to-date limits on the ten relevant Wilson coefficients. We summarize in Sec. 6.5.

The research presented in this chapter has previously been published in Reference [3]. All displayed figures and tables as well as part of the text are identical to the content of this article.

6.1 Basic concepts of EFTs

As a complementary approach to specific high–scale models, EFTs are used to parametrize deviations from the SM without including additional particles. In the introduction we discussed how Fermi theory can be viewed as an effective theory of the SM at scales below the mass of the W boson. In the same sense we can consider the SM as an EFT of a theory living at higher scales and we can extend the SM Lagrangian with additional operators to parametrize our ignorance of the new physics effects.

Since the action needs to be of mass dimension zero, each term of a Lagrangian must have mass dimension four. Aside from the CP–violating operator $\tilde{G}^a_{\mu\nu} G^{\mu\nu,a}$ [283] all possible operators of this mass dimension are already included in the SM Lagrangian. Hence, the additional operators of the EFT will be of mass dimension five or higher and suppressed by a mass scale Λ to obtain terms with the appropriate mass dimension,

$$\mathcal{L}_{EFT} = \mathcal{L}_{SM} + \sum_i \frac{f_i}{\Lambda^{d_i-4}} O_i \ . \tag{6.1}$$

The prefactors f_i are called Wilson coefficients and d_i denotes the mass dimension of the operator O_i.

EFTs can be used either in a top–down or bottom–up approach. In the top–down approach a specific perturbative model is mapped to an EFT where the low–scale impact of new particles is parametrized via higher–dimensional operators, operating on the SM particle content and their derivatives. Λ is the natural choice for a matching scale with a given complete theory.

[*] At the time of publication of this thesis no combined analysis of the electroweak and Higgs–sector has been published by ATLAS and CMS.

Starting from the measured observables we use instead the EFT as a bottom-up approach to parametrize deviations from the SM prediction without the necessity to choose a specific high–scale model.

We apply several constraints to reduce the number of potential operators. In effective Lagrangian expansion the operators are suppressed by powers of the high energy scale, which provides a natural counting scheme, such that we can order the Lagrangian according to the inverse powers of the new physics scale. Motivated by this ordering, we will consider the lowest mass dimension yielding relevant operators under the assumption that higher dimensional operators will have suppressed effects. At mass dimension 5, the only operator that can be built from SM fields is the lepton number violating operators $(\bar{L}_L\tilde{\phi}^*)(\tilde{\phi}^\dagger L_L)$ that generates Majorana mass terms for neutrinos. For our analysis of the Higgs sector this operator is irrelevant. Hence, throughout the work presented in the thesis we focus on operators of mass dimension six.

Moreover we require that well tested symmetries like gauge and space time symmetries are conserved, reducing the number of possible dimension-six operators in the extension of the SM to 2499. Not counting flavor structure and Hermitian conjugation, the number of independent operators is further reduced to 59 [296].

We thus construct an effective Lagrangian expansion invariant under $SU(3)_c \times SU(2)_L \times U(1)_Y$ symmetry based on the SM field content, including the Higgs–like state as a light electroweak doublet. This approach is commonly referred in the literature as the linear effective theory [284–296].

The choice of the operators basis is not unique. Using equations of motions we can convert different basis choices into each other. For our analysis of the Higgs sector we rely on the Hagiwara-Ishihara-Szalapski-Zeppenfeld basis (HISZ) [294].

In the following we introduce the relevant operators for a Higgs–EFT including TGV.

6.1.1 A basis for a combined analysis

The minimum independent set of dimension–six operators consists of 59 baryon number conserving operators, barring flavor structure and Hermitian conjugation. We follow the definition of the relevant operator basis for LHC Higgs and TGV physics described in detail in Reference [298, 299]. We start by restricting the initial set to P and C–even operators. We then use the equations of motion to rotate to a basis where there are no blind directions linked to electroweak precision data. In practice, we can neglect all operators contributing to electroweak precision observables at tree–level; they are strongly constrained by the several low energy measurements, rendering them irrelevant for current Higgs and TGV studies at the LHC. We then neglect all operators that cannot be studied at the LHC yet, because they only contribute to interactions we are not sensitive to. This includes the HHH vertex or the Higgs interactions with light-generation fermions. Finally, we are left with ten dimension–six operators [298, 299] in Tab. 6.1. In our conventions, the Higgs doublet covariant derivative

$O_{GG} = \phi^\dagger\phi\, G^a_{\mu\nu}G^{a\mu\nu}$	$O_{\phi,2} = \frac{1}{2}\partial^\mu\left(\phi^\dagger\phi\right)\partial_\mu\left(\phi^\dagger\phi\right)$	$O_{e\phi,33} = (\phi^\dagger\phi)(\bar{L}_3\phi e_{R,3})$
$O_{BB} = \phi^\dagger\hat{B}_{\mu\nu}\hat{B}^{\mu\nu}\phi$	$O_B = (D_\mu\phi)^\dagger\hat{B}^{\mu\nu}(D_\nu\phi)$	$O_{u\phi,33} = (\phi^\dagger\phi)(\bar{Q}_3\tilde{\phi}u_{R,3})$
$O_{WW} = \phi^\dagger\hat{W}_{\mu\nu}\hat{W}^{\mu\nu}\phi$	$O_W = (D_\mu\phi)^\dagger\hat{W}^{\mu\nu}(D_\nu\phi)$	$O_{d\phi,33} = (\phi^\dagger\phi)(\bar{Q}_3\phi d_{R,3})$
$O_{WWW} = \mathrm{Tr}\left(\hat{W}_{\mu\nu}\hat{W}^{\nu\rho}\hat{W}^\mu_\rho\right)$		

Table 6.1: List of operators included in our analysis.

is $D_\mu\phi = \left(\partial_\mu + ig'B_\mu/2 + ig\sigma_a W^a_\mu/2\right)\phi$. The hatted field strengths are $\hat{B}_{\mu\nu} = ig'B_{\mu\nu}/2$ and $\hat{W}_{\mu\nu} = ig\sigma^a W^a_{\mu\nu}/2$, where σ^a are the Pauli matrices, and g and g' stand for the $SU(2)_L$ and $U(1)_Y$ gauge couplings. The adjoint Higgs field is $\tilde{\phi} = i\sigma_2\phi^*$. The effective Lagrangian which we use to interpret Higgs and TGV measurements at the LHC is

$$\begin{aligned}\mathcal{L}_{\text{eff}} = \mathcal{L}_{\text{SM}} &- \frac{\alpha_s}{8\pi}\frac{f_{GG}}{\Lambda^2}O_{GG} + \frac{f_{BB}}{\Lambda^2}O_{BB} + \frac{f_{WW}}{\Lambda^2}O_{WW} + \frac{f_{\phi,2}}{\Lambda^2}O_{\phi,2} + \frac{f_{WWW}}{\Lambda^2}O_{WWW} \\ &+ \frac{f_B}{\Lambda^2}O_B + \frac{f_W}{\Lambda^2}O_W + \frac{f_\tau m_\tau}{v\Lambda^2}O_{e\phi,33} + \frac{f_b m_b}{v\Lambda^2}O_{d\phi,33} + \frac{f_t m_t}{v\Lambda^2}O_{u\phi,33}\,. \end{aligned} \tag{6.2}$$

All operators except for O_{WWW} contribute to Higgs interactions. Their contributions to the several Higgs vertices, including non–SM Lorentz structures, are described in Reference [42, 262].

Some of the operators in Tab. 6.1 contribute to the self-interactions of the electroweak gauge bosons. They can be linked to specific deviations in the Lorentz structures entering the WWZ and $WW\gamma$ interactions, usually written as $\kappa_\gamma, \kappa_Z, g_1^Z, g_1^\gamma, \lambda_\gamma$, and λ_Z [306]. After g_1^γ is fixed to unity because of electromagnetic gauge invariance, writing the deviations with respect to the SM values for example as $\Delta\kappa \equiv \kappa - 1$, the shifts are defined as

$$\begin{aligned}\Delta\mathcal{L}_{\text{TGV}} =& -ie\,\Delta\kappa_\gamma\, W^+_\mu W^-_\nu\gamma^{\mu\nu} - \frac{ie\lambda_\gamma}{m_W^2}\, W^+_{\mu\nu}W^{-\nu\rho}\gamma^\mu_\rho - \frac{ig_Z\lambda_Z}{m_W^2}\, W^+_{\mu\nu}W^{-\nu\rho}Z^\mu_\rho \\ &- ig_Z\,\Delta\kappa_Z\, W^+_\mu W^-_\nu Z^{\mu\nu} - ig_Z\,\Delta g_1^Z\,\left(W^+_{\mu\nu}W^{-\mu}Z^\nu - W^+_\mu Z_\nu W^{-\mu\nu}\right) \\ =& -ie\,\frac{g^2v^2}{8\Lambda^2}\,(f_W + f_B)\, W^+_\mu W^-_\nu\gamma^{\mu\nu} - ie\,\frac{3g^2 f_{WWW}}{4\Lambda^2}\, W^+_{\mu\nu}W^{-\nu\rho}\gamma^\mu_\rho \\ &- ig_Z\,\frac{g^2v^2}{8c_w^2\Lambda^2}\left(c_w^2 f_W - s_w^2 f_B\right)\, W^+_\mu W^-_\nu Z^{\mu\nu} - ig_Z\,\frac{3g^2 f_{WWW}}{4\Lambda^2}\, W^+_{\mu\nu}W^{-\nu\rho}Z^\mu_\rho \\ &- ig_Z\,\frac{g^2v^2 f_W}{8c_w^2\Lambda^2}\,\left(W^+_{\mu\nu}W^{-\mu}Z^\nu - W^+_\mu Z_\nu W^{-\mu\nu}\right)\,, \end{aligned} \tag{6.3}$$

where $e = gs_w$ and $g_Z = gc_w$. The two notational conventions are linked as

$$\Delta\kappa_\gamma = \frac{g^2v^2}{8\Lambda^2}\left(f_W + f_B\right) \qquad \Delta\kappa_Z = \frac{g^2v^2}{8c_w^2\Lambda^2}\left(c_w^2 f_W - s_w^2 f_B\right)$$
$$\Delta g_1^Z = \frac{g^2v^2}{8c_w^2\Lambda^2} f_W \qquad \Delta g_1^\gamma = 0 \qquad \lambda_\gamma = \lambda_Z = \frac{3g^2M_W^2}{2\Lambda^2} f_{WWW} \,. \tag{6.4}$$

The $SU(2)$-gauge-invariant formulation in terms of dimension−six operators induces correlations of the formerly multi-dimensional space of modified gauge couplings,

$$\lambda_Z = \lambda_\gamma \qquad \text{and} \qquad \Delta\kappa_Z = -\frac{s_w^2}{c_w^2}\Delta\kappa_\gamma + \Delta g_1^Z \,. \tag{6.5}$$

This defines what is usually referred to as the LEP scenario in the analysis of anomalous TGV interactions. The three relevant Wilson coefficients relevant for our analysis of di-boson production are f_B, f_W and f_{WWW}.

The assumption that f_B, f_W and f_{WWW} parametrize the leading new physics deviations with respect to the SM triple gauge boson couplings is linked to the hypothesis of the Higgs boson being still part of an $SU(2)_L$ doublet. If we deviated from this scenario, and considered instead the more generic non-linear or chiral effective Lagrangian [300, 307–310], the parametrization would be extended. In the most generic scenario, the couplings defined in Eq. (6.3) depend on a larger number of parameters and the correlations expressed in Eq. (6.5) are lost. Furthermore, the deviations generated by non-linear operators in the TGVs could be completely decorrelated to the deviations generated in the Higgs interactions. As it has been studied in detail in [300, 310], this different pattern of anomalous interactions could be potentially used to test the nature of the Higgs boson.

6.2 Triple gauge boson interactions

In our analysis we describe the measured di-boson production rates from the LHC Run I in terms of the Lagrangian given in Eq. (6.3). We include the eight $WV(V = W, Z)$ di-boson measurements with the highest sensitivity for charged triple gauge boson vertices. Adding the public $W\gamma$ LHC results, only available for 7 TeV so far [46, 311], does not improve our results.

For each analysis we first determine which of the kinematic distributions given in the publications is most sensitive to anomalous TGVs. This defines our list of channels and kinematic variables displayed in Tab. 6.2, as well as the available number of bins of the distribution.

In the final states only $\ell^{(\prime)} = e, \mu$ are considered, channels with $(0j)$ include a jet veto, and the two semileptonic channels include a veto on a third hard jet.

Channel	Distribution	# bins	Data set
$WW \to \ell^+\ell'^- + \not{E}_T$ $(0j)$	Leading lepton p_T	4	ATLAS 8 TeV, 20.3 fb^{-1} [312]
$WW \to \ell^+\ell^{(\prime)-} + \not{E}_T$ $(0j)$	$m_{\ell\ell^{(\prime)}}$	8	CMS 8 TeV, 19.4 fb^{-1} [313]
$WZ \to \ell^+\ell^-\ell^{(\prime)\pm}$	m_T^{WZ}	6	ATLAS 8 TeV, 20.3 fb^{-1} [314]
$WZ \to \ell^+\ell^-\ell^{(\prime)\pm} + \not{E}_T$	Z candidate $p_T^{\ell\ell}$	10	CMS 8 TeV, 19.6 fb^{-1} [315]
$WV \to \ell^\pm jj + \not{E}_T$	V candidate p_T^{jj}	12	ATLAS 7 TeV, 4.6 fb^{-1} [316]
$WV \to \ell^\pm jj + \not{E}_T$	V candidate p_T^{jj}	10	CMS 7 TeV, 5.0 fb^{-1} [317]
$WZ \to \ell^+\ell^-\ell^{(\prime)\pm} + \not{E}_T$	Z candidate $p_T^{\ell\ell}$	7	ATLAS 7 TeV, 4.6 fb^{-1} [318]
$WZ \to \ell^+\ell^-\ell^{(\prime)\pm} + \not{E}_T$	Z candidate $p_T^{\ell\ell}$	8	CMS 7 TeV, 4.9 fb^{-1} [315]

Table 6.2: List of di-boson measurements we include in our analysis.

Using one of the leading experimental channel, i.e. the leptonic ATLAS WW production at 8 TeV [312] we illustrate the procedure of limit–setting. We start with the extraction of data from the paper, followed by the reproduction of the analysis. Next we parametrize the distributions in terms of Wilson coefficients using bin–by–bin correction factors. Finally we construct the likelihood function and perform the fit using the SFitter framework. Wherever the experimental collaborations present their results in terms of anomalous TGVs we validate our procedure through a detailed comparison with their results.

6.2.1 Analysis framework

As an illustrative example we use one of the most sensitive channels, namely the leptonic ATLAS WW analysis based on 20.3 fb^{-1} of 8 TeV data [312]. One advantage of this analysis is that ATLAS presents their results in terms of TGVs, which allows us to compare their results with the ones of our SFitter implementation. The other seven channels are treated exactly in the same way.

We start by directly reading off the background expectation (defined as all SM processes except for the di-boson production channels), the expected contribution from WW production in the Standard Model and the measured event number bin by bin from the relevant experimental figure. The background rates we use directly from the experimental analysis, without any need to modify them.

Next, we generate WW events with SM couplings in the fiducial region using MadGraph5 [319], Pythia [320] for parton shower and hadronization, and Delphes [321] for fast detector simulation. We model here the ATLAS selection, which is very similar to the analogous CMS analysis [313]. The selection procedure requires exactly one electron and one muon of opposite

charges in the central detector and outside the transition regions,

$$\begin{aligned} p_{T,\ell} &> 25,20 \text{ GeV} & |\eta_\mu| &< 2.4 \\ \Delta R_{e\mu} &> 0.1 & m_{e\mu} &> 10 \text{ GeV} \\ |\eta_e| &< 2.47 \quad \text{excluding } 1.37 < |\eta_e| < 1.52 \,. \end{aligned} \tag{6.6}$$

In addition, the summed transverse energy within a cone of $\Delta R = 0.3$ around each lepton is required to be smaller than 14% of $p_{T,\ell}$, and the scalar sum of the p_T of the tracks within the same cone has to stay below 10% of $p_{T,\ell}$ for the electron and 12% for the muon. A third lepton is vetoed for $p_{T,\ell} > 7$ GeV, as are jets with $p_{T,j} > 25$ GeV and $|\eta_j| < 4.5$. The latter removes the top pair background. A set of requirements on missing energy related variables starts with a requirement on p_T^{miss}, constructed as the length of the negative 2-vectorial sum of all identified leptons and tracks not associated with leptons [312]. To select events with neutrinos ATLAS requires

$$p_T^{\text{miss}} > 20 \text{ GeV} \qquad \text{and} \qquad \Delta\phi\left(\vec{E}_T^{\text{miss}}, \vec{p}_T^{\text{miss}}\right) < 0.6 \,. \tag{6.7}$$

A second missing energy variable has to fulfill

$$E_{T,\text{Rel}}^{\text{miss}} > 15 \text{ GeV} \qquad \text{with} \quad E_{T,\text{Rel}}^{\text{miss}} = \begin{cases} E_T^{\text{miss}} \sin(\Delta\phi_\ell) & \text{if} \quad \Delta\phi_\ell < \pi/2 \\ E_T^{\text{miss}} & \text{if} \quad \Delta\phi_\ell \geq \pi/2 \,, \end{cases} \tag{6.8}$$

where $\Delta\phi_\ell$ is the azimuthal angle between the missing transverse momentum vector and the nearest lepton.

We use the SM WW events rates in the signal region to tune our event generation, both in terms of the total rate and in the most relevant kinematic distribution. For the latter, we identify the kinematic distribution which is most sensitive to anomalous TGVs and which we will later include in our SFitter analysis. Of the variables and ranges shown in the ATLAS note, the leading $p_{T,\ell}$ has the largest potential because it tracks the momentum flow through the anomalous vertex best [336–339]. This means that our event generation has to reproduce Fig. 11 in Reference [312]. To ensure this, we introduce a bin-by-bin correction factor to account for phase–space dependent differences in the selection procedure because of detector effects as well as higher order corrections to the cross section prediction [322–327].

We check this default procedure using an alternative setup in each channel where instead of matching our SM WV distributions bin-by-bin, we only match our inclusive WV rate prediction in the Standard Model in the signal region. Both methods give consistent results for the combined analysis.

Assuming that the same bin-by-bin correction from the SM WW events applies to the relatively small new physics effects, we generate the leading $p_{T,\ell}$ distribution in the presence of dimension–six operators. For this we rely on an in-house MadGraph5 implementation of the operators constructed with FeynRules [328].

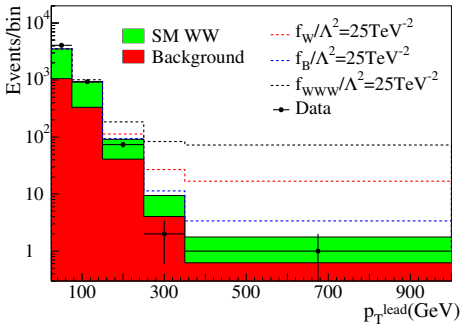

Figure 6.1: Leading $p_{T,\ell}$ distribution for the 8 TeV ATLAS WW analysis [312]. The red histogram shows the ATLAS background estimate (excluding the SM WW prediction), while the green histogram shows the total SM prediction once WW processes are added. The observed events are shown as dots, with error bars accounting for the statistical uncertainty. The dashed lines indicate the effects of dimension–six Wilson coefficients.

As is well known higher dimensional operators give rise to fast growth of the scattering amplitude with energy, eventually violating partial-wave unitarity [340–342]. Here we did not introduce ad-hoc form factors to dampen the scattering amplitude at high energies because we verified that there is no partial-wave unitarity violation in the different channels for the values of the Wilson coefficients in the 95% CL allowed regions, except for very large and already ruled out values of f_B.

The predicted number of events for a given Wilson coefficient is the sum of SM and new physics WW events, together with the SM backgrounds which we directly extract from the ATLAS documentation. These backgrounds are dominated by top production, followed by W+jets and Drell-Yan events. All of them are estimated using data-driven techniques. Only the small di-boson backgrounds are based on Monte Carlo estimates [312].

In Fig. 6.1 we show the final estimates for the SM background and the SM prediction for WW production. They are in agreement with the number of observed events. The dashed lines illustrate the effects from individual dimension-six operators, suggesting that we should be able to derive powerful constraints from the ATLAS measurements. The fact that the last bin extends to large transverse momenta also suggests that we have to be careful interpreting our dimension-six analysis in terms of an effective field theory expansion [42, 262, 331–338].

In the final step of the SFitter analysis we construct a likelihood function for the given data set to determine the part of parameter space allowed at a given CL. We include a Poisson–shaped statistical uncertainty for the observed number of events for each bin, a Poisson-shaped statistical uncertainty for the background events, a flat theoretical uncertainty correlating between all

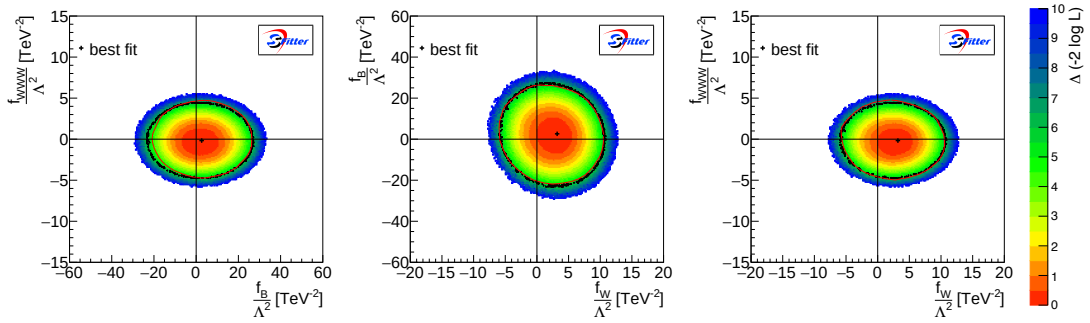

Figure 6.2: Correlated profile likelihood for sets of two Wilson coefficients from the 8 TeV ATLAS WW analysis [312]. Black dots signal $\Delta(-2\log L) = 5.99$, while the crosses stand for the best fit point. The red solid contour are the 95% CL limits from ATLAS [312].

bins in the $p_{T,\ell}$ distribution, and a selection of the most relevant systematic uncertainties with a Gaussian shape. For technical details on the likelihood construction we refer to Chapter 2. The systematic uncertainties include the luminosity estimate, detector and lepton reconstruction/isolation uncertainties, and some additional uncertainty for the background normalization and/or shape.

These uncertainties can be seen in the following, together with the selection of experimental systematic uncertainties considered for the rest of the analyses.

Channel	Exp	Lumi	Detector eff	Lepton eff	Background
$WW \to \ell^+\ell'^- + \not{E}_T$ $(0j)$ [312]	ATLAS	2.0%	1.4%	1.4%	2.0%
$WW \to \ell^+\ell^{(\prime)-} + \not{E}_T$ $(0j)$ [313]	CMS	2.6%	1.0%	3.8%	2.0%
$WZ \to \ell^+\ell^-\ell^{(\prime)\pm}$ [314]	ATLAS	2.8%	0.5%	1.7%	1.6%
$WZ \to \ell^+\ell^-\ell^{(\prime)\pm} + \not{E}_T$ [315]	CMS	4.4%	3.1%	2.0%	2.5%
$WV \to \ell^\pm jj + \not{E}_T$ [316]	ATLAS	1.8%	10%	1.1%	14%
$WV \to \ell^\pm jj + \not{E}_T$ [317]	CMS	2.2%	1.0%	2.0%	–
$WZ \to \ell^+\ell^-\ell^{(\prime)\pm} + \not{E}_T$ [318]	ATLAS	1.8%	0.5%	1.9%	–
$WZ \to \ell^+\ell^-\ell^{(\prime)\pm} + \not{E}_T$ [315]	CMS	2.2%	3.8%	2.4%	5.5%

For the cases where we quote no numbers we assume that those systematic uncertainties are well below the statistical and theoretical uncertainties for which we allow for a variation of 5% for WW, 4% for WZ and 4% for WV-semileptonic channels. We fully correlate theoretical uncertainties for sets with the same di-boson final state.

For the pure TGV analysis we construct Markov chains to probe the three-dimensional parameter space spanned by f_W, f_B and f_{WWW}. Based on these chains we determine the part of the parameter space allowed at a given CL.

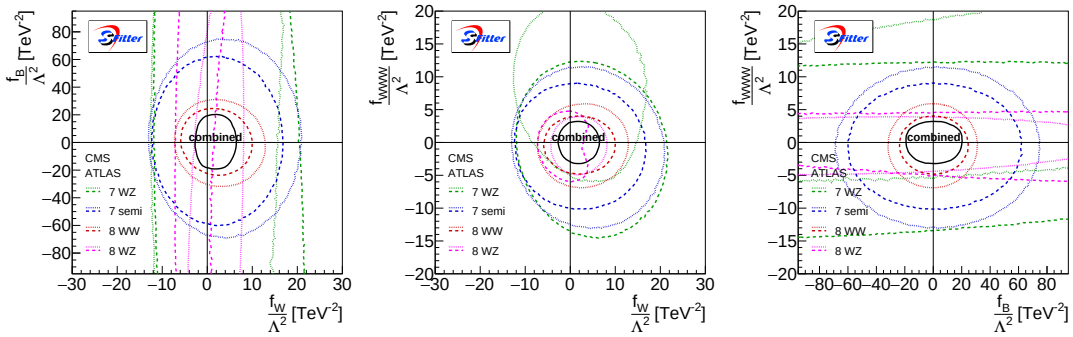

Figure 6.3: Results of the TGV analysis from LHC Run I. We show all two-dimensional profile likelihoods in the three-dimensional parameter space at 95% CL (2dof) for the individual channels as well as their combination.

In Fig. 6.2 we show the three two-dimensional profile likelihoods for the three relevant Wilson coefficients. We find the best-fit point for a mildly positive value of f_W/Λ^2, driven by a small deficit of events in the tail of the leading $p_{T,\ell}$ distribution shown in Fig. 6.1. The SM gives $\chi^2 \approx -2 \log L = 6.6$, defined after profiling over the theoretical uncertainties, and is perfectly compatible with the best fit point at $\chi^2 \approx -2 \log L = 6.0$. We have checked that none of these results change if we replace the profile likelihood by a slice of parameter space setting the third Wilson coefficient to zero.

The black dots in Fig. 6.2 indicate our 95% CL contour and allow us to compare with the red line, that illustrates the 95% CL region from the anomalous TGV analysis by ATLAS [312]. Both are in excellent agreement with each other, indicating that our approximations concerning detector effects or higher order corrections are more than sufficient given the current reached precision of the analysis.

We follow a similar procedure for all eight di-boson channels. Among those the 8 TeV CMS WW analysis [313] and the semi-leptonic 7 TeV ATLAS WV analysis [316] quote limits on dimension−six operators from the measurement of anomalous TGVs in the framework of Eq. (6.5). In both cases we find a similar level of agreement.

6.2.2 Results from LHC Run I

In Fig. 6.3 we show the results of our pure TGV analysis in terms of the Wilson coefficients defined in Eq. (6.2). In addition to each individual ATLAS and CMS channel we give the combined constraints from all eight channels. For the combination, we find a global minimum at a Gauss-equivalent $\chi^2 \approx -2 \log L = 48.3$ for a total of 65 data points, while $\chi^2 \approx -2 \log L = 49.7$ for the Standard Model. The regions allowed by the different searches are mutually compatible and show no significant preference for a deviation from the Standard Model. Moreover, the

structure of the parameter space is simple enough that none of the two-dimensional planes significantly change if instead of a profile likelihood we show a slice where the third Wilson coefficient is zero.

The Wilson coefficient f_B is the least constrained because it hardly affects the WWZ vertex since its contribution is suppressed by a factor s_w^2/c_w^2. Instead, the constraints on f_B come from the fully leptonic WW searches and to some degree from the WV-semileptonic analyses, both probing the $WW\gamma$ interaction. The ATLAS WW channel at 8 TeV sets the strongest bounds on f_B.

Comparing f_W and f_{WWW}, we notice that the combination of the WWZ and $WW\gamma$ vertices with the large transverse momentum available at the LHC leads to similar sensitivities on both; equivalently, we find comparable sensitivities on $\lambda_{\gamma,Z}$ and Δg_1^Z. The new physics reach in f_W and f_{WWW} is clearly stronger than in f_B. The strongest bounds on f_{WWW} stem from the combination of the two 8 TeV WZ leptonic searches together with the ATLAS 8 TeV WW analysis. In the case of f_W, the 8 TeV WZ analyses present a higher sensitivity, but again the 8 TeV WW searches are close in their precision. The constraint on f_W benefits most from a combination of the different experimental channels.

Generally, even though the WV-semileptonic results presented here are less sensitive to the dimension–six operators, they are not far from the most powerful leptonic WW and WZ analyses. This is remarkable, given the fact that these semileptonic measurements are still based on the 7 TeV smaller data sets. An update of the semileptonic channels should significantly contribute to a global TGV analysis.

The one-dimensional 95% CL constraints on the combination of Wilson coefficients are

$$\frac{f_W}{\Lambda^2} \in [-1.5, 6.3\,]\ \text{TeV}^{-2} \qquad \frac{f_B}{\Lambda^2} \in [-14.3, 15.9\,]\ \text{TeV}^{-2} \qquad \frac{f_{WWW}}{\Lambda^2} \in [-2.4, 3.2\,]\ \text{TeV}^{-2}\,. \tag{6.9}$$

The same results can also be expressed as

$$\frac{\Lambda}{\sqrt{|f_W|}} > 0.82\,(0.40)\ \text{TeV} \qquad \frac{\Lambda}{\sqrt{|f_B|}} > 0.26\,(0.25)\ \text{TeV} \qquad \frac{\Lambda}{\sqrt{|f_{WWW}|}} > 0.65\,(0.56)\ \text{TeV}\,, \tag{6.10}$$

where the bounds stand for the limits obtained assuming a negative (positive) Wilson coefficient. Moreover, we can present our results in terms of three independent TGV couplings [306], as described in Sec. 6.1, the 95% CL constraints then read

$$\Delta g_1^Z \in [-0.006,\ 0.026\,] \qquad \Delta\kappa_\gamma \in [-0.041,\ 0.072\,] \qquad \lambda_{\gamma,Z} \in [-0.0098,\ 0.013\,]\,. \tag{6.11}$$

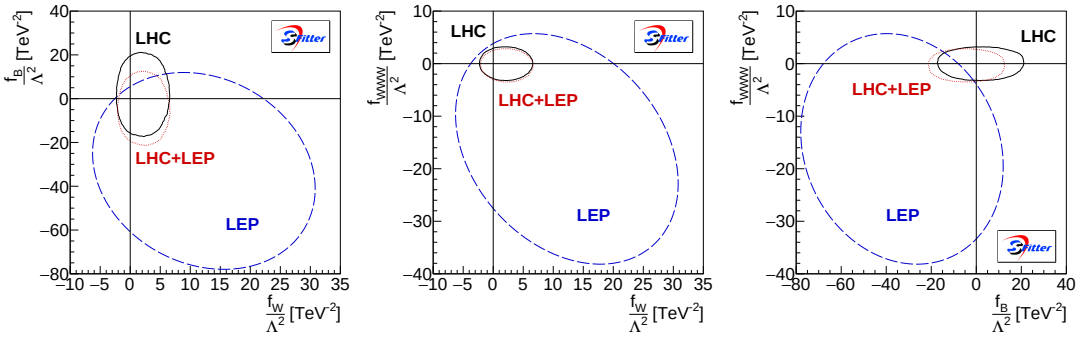

Figure 6.4: Results of the TGV analysis in terms of two-dimensional profile likelihoods from LHC Run I and from LEP [330]. We also show the statistical combination of both.

One aspect that we have tested is how robust our results are when we change our approximate treatment of fully correlated theoretical uncertainties. It turns out that removing these correlations slightly shifts the f_W range towards negative values and weaken the bound on f_B; both effects are at the level of less than 0.5 standard deviations.

To allow for an easy presentation of the approximate fit results we perform a Gaussian fit to the multi-dimensional probability distribution function of the three Wilson coefficients relevant for TGVs. For the mean, one standard deviation and the error correlation matrix we find

$$\frac{f_W}{\Lambda^2} = (2.2 \pm 1.9)\ \text{TeV}^{-2} \qquad \frac{f_B}{\Lambda^2} = (3.0 \pm 8.4)\ \text{TeV}^{-2} \qquad \frac{f_{WWW}}{\Lambda^2} = (0.55 \pm 1.4)\ \text{TeV}^{-2}$$
$$\rho = \begin{pmatrix} 1.00 & -0.012 & -0.062 \\ -0.012 & 1.00 & -0.0012 \\ -0.062 & -0.0012 & 1.00 \end{pmatrix}. \tag{6.12}$$

The corresponding Gaussian fit results to the multi-dimensional probability distribution function for the TGV couplings in Eq. (6.4) are shown in Table 6.3.

6.3 Comparison and combination with LEP

When we express our results in terms of the TGVs defined in Eq. (6.4) we can easily compare them and eventually combine them with the global LEP analysis results [330]. We show the separated LHC Run I and LEP limits in Table 6.3. As we can see, the combined LHC Run I di-boson channels determine the anomalous TGV parameters a factor 3-6 more precisely than LEP. Moreover, the more diverse set of LHC observables implies that the different coupling measurements are less correlated.

The same comparison between the combined LHC Run I results and the LEP bounds is illustrated in Fig. 6.4, now in terms of dimension-six Wilson coefficients. In these two-dimensional

	LHC Run I				LEP			
	68 % CL	Correlations			68 % CL	Correlations		
Δg_1^Z	0.010 ± 0.008	1.00	0.19	−0.06	$0.051^{+0.031}_{-0.032}$	1.00	0.23	−0.30
$\Delta\kappa_\gamma$	0.017 ± 0.028	0.19	1.00	−0.01	$-0.067^{+0.061}_{-0.057}$	0.23	1.00	−0.27
λ	0.0029 ± 0.0057	−0.06	−0.01	1.00	$-0.067^{+0.036}_{-0.038}$	−0.30	0.27	1.00

Table 6.3: Measured central values, standard deviations and correlation coefficients for Δg_1^Z, $\Delta\kappa_\gamma$ and λ from the combined LHC Run I di-boson analyses (left) and from LEP [330] (right).

profile likelihoods we also show the statistical combination of the two data sets. While the LHC precision shown in Eq. (6.9) clearly dominates the combination of LHC and LEP results, we still quote the combined limits on the three relevant Wilson coefficients,

$$\frac{f_W}{\Lambda^2} \in [-1.3,\ 6.3\,]\ \text{TeV}^{-2} \qquad \frac{f_B}{\Lambda^2} \in [-18.5,\ 10.9\,]\ \text{TeV}^{-2}$$
$$\frac{f_{WW}}{\Lambda^2} \in [-2.7,\ 2.8\,]\ \text{TeV}^{-2}\,. \tag{6.13}$$

Adding the LEP results does not lead to a significant improvement. The range for f_B slightly shifts towards more negative values as a consequence of the preferred LEP central values.

6.4 Gauge–Higgs combination

In the final step of our effective field theory analysis, we have to combine the LHC Run I results on TGVs and Higgs couplings. The main reason is that O_W and O_B contribute to anomalous Higgs interactions and the triple gauge boson interactions at the same time [287, 297–299]. Consequently, a study of the underlying Wilson coefficients should include both sets of experimental analyses. Furthermore, the combination of the two can be used to test the nature of the electroweak symmetry breaking mechanism [300].

For the sake of comparison we start with a brief summary of the global analysis of the LHC Run I Higgs data presented in Reference [42, 262], where constraints on the dimension-six Wilson coefficients in Eq. (6.2) are derived from Higgs measurements alone. That data consists of 159 observables for event rates, plus 14 additional measurements related to kinematics. This kinematic information is crucial to disentangle the strongly correlated effects of non–SM Lorentz structures generated by O_{WW}, O_{BB}, O_W, and O_B. This way, the kinematic distributions significantly improve the global Higgs fit.

As an illustration, we show three of the relevant two-dimensional profile likelihoods from the pure Higgs analysis including kinematic distributions in the first row of Fig. 6.5. In the

upper-left panel we see a strong correlation between O_{WW} and O_{BB}, even after including the kinematic distributions. This is due to both operators contributing to the decay rate $H\gamma\gamma$. Without kinematic information the wide pattern in the upper left part simply extends to the lower right part [42, 262]. The improvement in the region of large positive (negative) f_{WW} (f_{BB}) appears because both operators contribute to the HWW and HZZ vertices, to which the kinematic distributions are sensitive. In the upper-center panel we show the correlations between O_W and O_B. While the kinematic distributions significantly improve the situation, a secondary region still remains for negative f_B. Finally, in the upper-right panel we show the O_B vs O_{BB} plane. Again, the kinematic information largely removes the strong correlations for negative O_B and O_{BB} values.

In the lower panels of Fig. 6.5 we depict the same two-dimensional profile likelihoods once we include the di-boson TGV measurements from LHC Run I; although LEP limits hardly have any numerical effect, they are included as well. We construct the global likelihood accounting

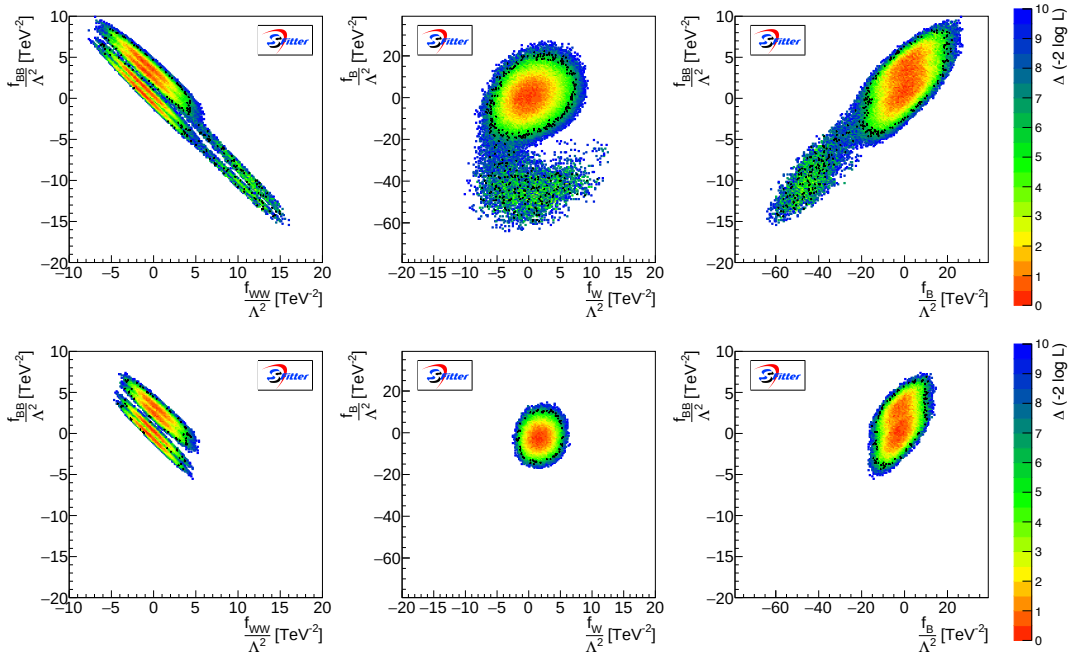

Figure 6.5: Correlated profile likelihood for sets of two Wilson coefficients. In the first row we include only LHC Run I Higgs data, including kinematic distributions, as shown in Fig. 11 of Reference [42, 262]. In the second row we add the Run I di-boson results probing anomalous TGV interactions (as well as the corresponding LEP results). The black points indicate $-2 \log L = 5.99$. The corresponding one-dimensional profile likelihoods can be found in Fig. 6.6.

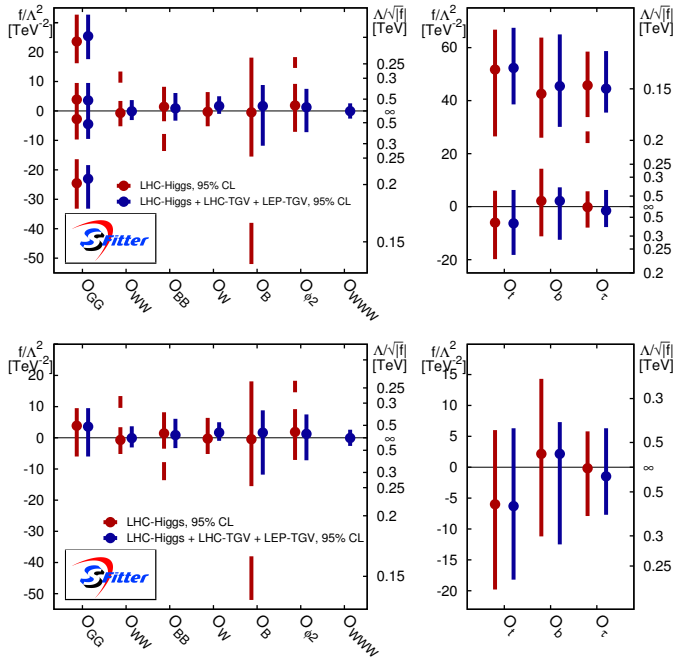

Figure 6.6: Allowed 95% CL ranges for individual Wilson coefficients f_x/Λ^2 from a one-dimensional profile likelihood. We show results from Run I Higgs observables only (red bars) and for a combined Higgs plus TGV analysis (blue). For the upper panels we allow for sign changes in the individual Yukawa couplings, while in the lower panel we fix their signs to the Standard Model one.

for the correlations in systematic uncertainties between the Higgs observables and the TGV observables. This can be easily achieved in the SFitter framework described in Sec. 6.2 and Reference [42, 262]. The systematic experimental uncertainties are assumed to be correlated for observables in ATLAS and in CMS, but uncorrelated between the two experiments.

For all three panels the effect of the TGV measurements is remarkable. The combination of Higgs and TGV results clearly deliver stronger limits than either of the two analyses independently. The secondary solution in f_B has vanished altogether, the precision on f_W has improved, negative values of f_{BB} are excluded through correlations with f_B, and in the correlation of f_{BB} and f_{WW} we can clearly see two different regions corresponding to sign changes in the $H\gamma\gamma$ coupling.

In Table 6.4 and Fig. 6.6 we show the limits on individual Wilson coefficients for each of the dimension–six operators included in the analysis, Eq. (6.2). In the upper panels of Fig. 6.6 and in the table we clearly see secondary solutions due to sign flips in the individual Yukawa and Hgg couplings. In the lower panels of Fig. 6.6 we show only the solutions for parameter space with

f_x/Λ^2		LHC–Higgs	LHC–Higgs + LHC–TGV + LEP–TGV	
[TeV^{-2}]	Best fit	95% CL interval	Best fit	95% CL interval
f_{GG}	−24.5	(−33.2, 16.4)	−4.5	(−32.5, −18.4)
	−2.8	(−9.7, 9.5)	−23.0	(−9.5, 9.5)
	3.9	(16.2, 32.7)	3.6	(17.6, 32.5)
	23.6		25.4	
f_{WW}	−0.7	(−5.2, 3.4) ∪ (9.6, 13.4)	−0.1	(−3.1, 3.7)
f_{BB}	1.4	(−13.6, −7.8) ∪ (−3.5, 8.2)	0.9	(−3.3, 6.1)
$f_{\phi,2}$	1.9	(−7.1, 9.2) ∪ (14.6, 18.3)	1.3	(−7.2, 7.5)
f_W	−0.3	(−5.2, 6.4)	1.7	(−0.98, 5.0)
f_B	−0.5	(−52, −38) ∪ (−15.5, 18.1)	1.7	(−11.8, 8.8)
f_{WWW}		−−	-0.06	(−2.6, 2.6)
f_b	2.2	(−11.2, 14.3)	2.2	(−12.5, 7.3)
	42.6	(26, 64)	45.6	(30, 65)
f_τ	45.8	(−7.9, 5.8) ∪ (24, 28)	44.5	(−7.7, 6.3)
	−0.2	(34, 59)	−1.5	(36, 59)
f_t	51.8	(−19.8, 6.0)	52.3	(−18.2, 6.3)
	−6.0	(27, 67)	−6.3	(39, 68)
	$-2\log L_{\text{min}} = 98.1$, $-2\log L_{\text{SM}} = 101.9$		$-2\log L_{\text{min}} = 152.3$, $-2\log L_{\text{SM}} = 156.8$	

Table 6.4: Best fit values and 95% CL ranges for the Higgs analysis (dark red bars in Fig. 6.6) and after combining with TGV results (blue bars in Fig. 6.6). We also show log-likelihood values, where $(-2\log L)_{\text{SM}}$ is defined after profiling over the theoretical uncertainties.

SM signs of the Yukawa couplings, and focusing on the f_{GG} containing the SM point, extending our set of simplifications discussed in Sec. 6.1. In both cases we see that the limits including di-boson channels are significantly improved. This improvement is driven by the highest sensitivity we have derived on f_B and f_W, which feeds through to the remaining operators because of the existing correlations. Including the di-boson data removes all secondary solutions from non-trivial parameter correlations or strong non-Gaussian effects. The additional Wilson coefficient f_{WWW} is among the best-measured dimension–six modification in the gauge–Higgs sector studied here.

One caveat applies to these results the same way it applies to the Higgs analyses alone [42, 262, 331–338]. If we consider the dimension–six Lagrangian of Eq. (6.2) as the leading contribution of a consistent effective field theory expansion we need to show that for the relevant observables it captures the features of the full theories we want to describe. Computing the effects of dimension–eight operators appears to be one way of estimating the theoretical uncertainties which enter the translation of our dimension–six results into actual models. However, detailed

studies in the Higgs sector [331–338] indicate that individual dimension–eight contributions are not necessarily a good measure for these uncertainties. Therefore, the effective theory interpretation of the results on the truncated dimension-six Lagrangian shown in Fig. 6.6 should be done with care.

We finally remark that the global analysis of Higgs and TGV searches presented here relies on the common contribution of f_W and f_B to both sets of interactions. As described at the end of Sec. 6.1, this is a consequence of the assumption that the electroweak symmetry breaking is linearly realized with the Higgs boson being part of a doublet of $SU(2)_L$. In the non-linear scenario, deviations on the TGVs could be in general decorrelated from deviations on the Higgs interactions. If such deviations are observed, the measurement of these correlation patterns could be ultimately linked to the nature of the Higgs boson as discussed in detail in [300, 310].

6.5 Conclusion

We have presented a final analysis of the LHC Run I measurements related to weak boson self-interactions and Higgs decays in the framework of an effective Lagrangian to dimension–six. The parameter space for this analysis spans 10 relevant Wilson coefficients given in Eq. (6.2). All of them can be strongly constrained by the combination of Higgs and di-boson data.

For triple gauge-boson data we give the first combination of all the di-boson production channels at LHC Run I, relevant to constrain the three dimension–six operators contributing. The current bounds derived in Sec. 6.2 are a factor 3-6 more precise than the corresponding LEP bounds. Since LHC Run I is sensitive to the TGVs in a diverse set of channels, the allowed parameter ranges for the couplings are only weakly correlated; see Eq. (6.12). In the future, we expect sizable progress in particular for channels with semi-leptonic decays of weak-boson pairs.

In Sec. 6.4 we combine the Run I di-boson data with the Run I Higgs measurements [42, 262]. This leads to a significant improvement compared to both individual analyses. While in the Higgs analysis alone we are left with strong correlations between the different Wilson coefficients — leading to large non-Gaussian structures in the correlated likelihood — secondary solutions in the combined analysis are exclusively due to the signs of the Yukawa couplings. Furthermore, the use of the Higgs data leads to an improvement on the determination of TGVs, specially f_B. Our results shown in Fig. 6.6 clearly indicate that di-boson data should be part of any effective Lagrangian analysis of the Higgs sector at the LHC.

Chapter 7

Conclusion

One major challenge of modern particle physics is to make optimal use of experimental results facing the large amount of data and the complimentary character of different search techniques. Hence, two questions arise: Can we link search results from very different approaches? And what can we learn from such a combination? In this thesis, we have answered these questions with global fits once in the context of dark matter and once for the combination of Higgs measurements with electroweak data.

Searches for dark matter are categorized into three approaches: direct detection experiments, which look for dark matter scattering off of SM particles; collider searches, that try to produce dark matter from high energy collisions of known particles; and indirect detection techniques, that search for the products of annihilating dark matter. In recent years, direct detection experiments have set very strong bounds on the scattering cross section and collider experiments have excluded increasingly large mass ranges of BSM models. Facing these limits, Fermi–LAT, an experiment of the third category, has measured a γ–ray excess from the galactic center where we expect a large dark matter density. The interpretation of this excess as a dark matter signal is motivated by the fact that the annihilation cross section needed to fit the GC excess is of the same order of magnitude as the cross section needed to obtain the measured relic density.

Taking into account the full spectrum evaluated by Fermi–LAT, including statistical, systematic and theory uncertainties, we can fit the GC excess in the MSSM with a dark matter mass ranging from 60 to 300 GeV. The dominant annihilation channels are $\chi\chi \to b\bar{b}, WW, t\bar{t}$. To achieve our goal of a global fit combining all relevant measurements, we incorporate the precisely measured relic density in our fit. Assuming a single component of dark matter and standard cosmology, Fig. 4.6 shows that a combination with the relic density is possible and prefers annihilation via a pseudoscalar mediator in particular for a mediator mass slightly below the on-shell condition. The t–channel WW annihilation yields best results at the onset of the annihilation for dark matter masses around 80 GeV. The valid parameter space for an annihilation into $b\bar{b}$ is extremely narrow and therefore very difficult to see in global fits. Including the severe limits from direct detection experiments excludes most of the otherwise valid parameter space as illustrated in Fig. 4.7. Only dark matter candidates with same–sign Higgsino components

annihilating via the pseudoscalar mediator can avoid the direct detection constraints completely, due to cancellations in the Higgs–neutralino coupling. For the annihilation into WW only a small region of parameter space remains, that will soon be tested by direct detection experiments. The annihilation into $b\bar{b}$ is excluded and can only be recovered by an admixture of a wino component. Again future direct detection experiments will soon test the remaining parameter space for this channel.

Finally we establish the connection to colliders physics by the requirement of a dark matter contribution to the invisible decay width of the Higgs boson. This is only possible in the extended NMSSM framework, because an efficient annihilation of dark matter with mass below 63 GeV requires a light pseudoscalar, which is excluded in the MSSM. In the NMSSM we profit in addition from the singlino component of the LSP to adjust its coupling to mediators. Fig. 5.4 illustrates the annihilation channels and the large invisible branching ratio that we can achieve in agreement with relic density and respecting direct detection limits.

We have shown that we can combine results from direct detection, indirect detection and collider searches, not only to constrain dark matter models, but also to motivate further LHC searches for invisible Higgs decays.

Since the discovery of the Higgs boson the precise determination of its properties has been one of the main objectives of LHC analyses. A question of particular interest is the possible connection to BSM models as illustrated in our global NMSSM fit. In the absence of new discoveries, the assumption that new physics might be hiding at higher scales allows us to parametrize limits on Higgs couplings in terms of effective field theories. In the framework of the linear effective Lagrangian the dimension–six operators relate the weak boson self–interaction to the Higgs decays.

We present the first combination of the electroweak di–boson production channels from LHC Run I parametrized in terms of the three relevant operators O_B, O_W, and O_{WWW}. In Fig. 6.4, we show that the bounds obtained from our combination are a factor of 3-6 more precise than the corresponding LEP bounds and will increase even further with the results of the current Run II.

The combination of our results with the Higgs sector analysis [42, 262] leads to significant improvements in both analyses. Secondary solutions arising in the Higgs only analysis from the undetermined sign of the Yukawa couplings are excluded and the precision of the bounds on the Wilson coefficients f_B and f_W increases roughly by a factor of 2 compared to the Higgs-only analysis, as illustrated in Fig. 6.6. Respectively the precision has also increased with respect to the TGV only analysis, in particular for the coefficient related to O_B. We conclude that the results from the di–boson channels should be included in any EFT analysis of the Higgs sector.

Both analyses show the power of global fits in narrowing down the parameter space for BSM models. Moreover they allow us to combine complementary results from different experiments in a meaningful way. With new generations of direct detection experiments coming up and the LHC collecting data from Run II, global fits will play an important role in the search for new physics.

Acknowledgements

Looking back at the last three years it has been my pleasure to meet a lot of extraordinary people. I would like to use this opportunity to thank those who have supported me along the way and whose presence has inspired me.

First of all I would like to thank my advisor Tilman Plehn for accepting me as a Bachelor–, Master– *and* PhD student, for believing in me when I did not and for always leaving his door open.

I would like to thank Björn Malte Schäfer for refereeing my thesis and Stephanie Hansmann-Menzemer and Teresa Marrodan Undagoitia for being part of my examination committee.

I am grateful to the Heidelberg Graduate School of Fundamental Physics for the financial aid in form of a scholarship and travel support as well as to the Research Training Group 'Particle physics at the LHC' (DFG GRK 1940) for paying my travels and the first months of my PhD.

If you talked to me about my work during the last few years, you probably did not manage to escape without a short introduction to a mysterious program called SFitter. Special thanks go to Michael Rauch and Dirk Zerwas for enlightening me in endless fights with fortran, compilers and other SFitter related challenges. I took my first steps with this program during my time in France, which preceded my thesis but had a lasting impact. Therefore I would like to thank Laurent Duflot, Sophie Henrot-Versille and once again Dirk Zerwas for the warm welcome. As a consequence of this 'French connection' I want to mention the GDR Terascale (now IRN Terascale) for giving me and young researches in general a great platform to present their work.

The research conducted during my PhD was done in collaboration with many inspiring people. In addition to previously mentioned collaborators I would like to thank Martin Bauer, Nishita Desai, Oscar Éboli, Juan Gonzalez–Fraile, Maria Concepion Gonzalez–Garcia, Gregor Kasieczka, Rémi Lafaye, Simona Murgia, Michael Russell and Tim Tait for successful collaboration.

Finishing a PhD is not only a matter of scientific input but also relies on the organizational framework as well as technical support. Therefore I would like to thank Eduard Thommes, the ladies in the secretariat and Elmar Bittner for their great work.

The average consumption of ice cream in Germany ranges around 7.7 liter per person, which we can translate into natural units of 0.98 Ep/w (Eisproben per week). I would like to thank Gonzalo Alonso, Martin Bauer, Elias Bernreuther, Anke Biekötter, Johann Brehmer, Katja Böhnke, Daniel Camargo, Nishita Desai, Anastasia Filimonova, Karin Firnkes, Patrick Foldenauer, Josua

Göcking, Juan Gonzalez–Fraile, Jamil Hetzel, Sebastian Hoof, Jan Horak, Thomas Hugle, Jörg Jäckel, Florian Jetter, Martin Klassen, Rabea Link, Georg Manten, Viraf Mehta, Luminita Mihaila, Rhea Moutafis, Tilman Plehn, Peter Reimitz, Michael Russell, Torben Schell, Sebastian Schenk, Peter Schichtel, Linda Shen, Beatriz Tapia Oregui, Jamie Tattersall, Valentin Tenorth, Jennifer Thompson, Susanne Westhoff and Nikolai Zerf or short the Heidelberg Pheno group for being way above average in the best way ;-). It was lots of fun to work with you guys!

If you are looking for some excellent proof readers, I can highly recommend Martin Bauer, Anke Biekötter, Johann Brehmer, Anthony DiFranzo, Patrick Foldenauer, Juan Gonzalez–Fraile, Luminita Mihaila and Sebastian Schenk. Thank you all very much for your great work that made this thesis legible!

On the dark side of physics I would like to thank the Xenon group from across the river for fun evenings and trips.

At the end of my academic career I want to use the opportunity to thank my physics teachers Harald Maxdorf and Thomas Schultheis–Kneip for helping me discover that physics is so much better than its reputation.

I would like to thank Johann, Juan and Torben whose life choices made them leave physics and partially even the country before I could finish my thesis (shame on you! ;-)):

Torben, I would like to thank you for all your help and patience especially in my first year back in Heidelberg, for countless walks to Marstall including funny weekend stories and our Pheno class trip. I wish you and your family all the best for the future!

Johann, sharing an office with you was so much fun and I am honored that I was the first person to step on your feet during Tango Argentino ;-). Thank you for all the discussions over tea and the more than welcome distractions, whenever there was too much work. I hope New York will be as amazing as you pictured it!

Juan, I think you are the only person who actually read and commented the entire thesis. Amazing! I would have loved to include the pac man plot in my thesis but the real results weren't too bad neither ;-). Thank you for diving with me into the convoluted SFitter statistic treatment and for being as torn between physics and industry as me. I very much enjoyed our work on various projects and the finally successful motivation speeches. And if there is nothing more to say: Stop whining! ;-)

Guillaume, I want to wholeheartedly thank you for all your support, in particular during the last weeks of writing, and for reminding me that there is a life outside of work. No matter what happens, you can make me smile and I am looking forward to the future with you!

Last but no least I want to thank my parents for their love and support through all stages of my life. Without you I would never have made it!

References

[1] A. Butter, S. Murgia, T. Plehn and T. M. P. Tait, "Harmonizing the MSSM with the Galactic Center Excess," Phys. Rev. D **96**, 035036 (2017) [arXiv:1612.07115 [hep-ph]].

[2] A. Butter, T. Plehn, M. Rauch, D. Zerwas, S. Henrot-Versillé and R. Lafaye, "Invisible Higgs Decays to Hooperons in the NMSSM," Phys. Rev. D **93**, 015011 (2016) [arXiv:1507.02288 [hep-ph]].

[3] A. Butter, O. J. P. Éboli, J. Gonzalez-Fraile, M. C. Gonzalez-Garcia, T. Plehn and M. Rauch, "The Gauge-Higgs Legacy of the LHC Run I," JHEP **1607**, 152 (2016) [arXiv:1604.03105 [hep-ph]].

[4] A. Butter, "Fitting Dark matter," Student lecture 2017, research training group 'Particle Physics Beyond the Standard Model'. http://www.thphys.uni-heidelberg.de/gk_ppbsm/lib/exe/fetch.php?media=undefined:students-lectures-anja-butter-i.pdf

[5] M. Bauer, A. Butter, J. Gonzalez-Fraile, T. Plehn and M. Rauch, "Learning from a Higgs-like scalar resonance," Phys. Rev. D **95**, no. 5, 055011 (2017) [arXiv:1607.04562 [hep-ph]].

[6] M. Bauer, A. Butter, N. Desai, J. Gonzalez-Fraile and T. Plehn, "Validity of dark matter effective theory," Phys. Rev. D **95**, no. 7, 075036 (2017) [arXiv:1611.09908 [hep-ph]].

[7] A. Butter, G. Kasieczka, T. Plehn and M. Russell, "Deep-learned Top Tagging using Lorentz Invariance and Nothing Else," [arXiv:1707.08966 [hep-ph]].

[8] S. L. Glashow, "Partial Symmetries of Weak Interactions," Nucl. Phys. **22**, 579 (1961).

[9] A. Salam, "Weak and Electromagnetic Interactions," Conf. Proc. C **680519**, 367 (1968).

[10] S. Weinberg, "A Model of Leptons," Phys. Rev. Lett. **19**, 1264 (1967).

[11] P. W. Higgs, "Broken symmetries, massless particles and gauge fields," Phys. Lett. **12**, 132 (1964).

[12] P. W. Higgs, "Broken Symmetries and the Masses of Gauge Bosons," Phys. Rev. Lett. **13**, 508 (1964).

[13] F. Englert and R. Brout, "Broken Symmetry and the Mass of Gauge Vector Mesons," Phys. Rev. Lett. **13**, 321 (1964).

[14] G. Aad *et al.* [ATLAS Collaboration], "Observation of a new particle in the search for the Standard Model Higgs boson with the ATLAS detector at the LHC," Phys. Lett. B **716**, 1 (2012) [arXiv:1207.7214 [hep-ex]].

[15] S. Chatrchyan *et al.* [CMS Collaboration], "Observation of a new boson at a mass of 125 GeV with the CMS experiment at the LHC," Phys. Lett. B **716**, 30 (2012) [arXiv:1207.7235 [hep-ex]].

[16] M. Ajello *et al.* [Fermi-LAT Collaboration], "Fermi-LAT Observations of High-Energy γ-Ray Emission Toward the Galactic Center," Astrophys. J. **819**, no. 1, 44 (2016) [arXiv:1511.02938 [astro-ph.HE]].

[17] R. Lafaye, T. Plehn and D. Zerwas, "SFITTER: SUSY parameter analysis at LHC and LC," arXiv:hep-ph/0404282;

[18] R. Lafaye, T. Plehn, M. Rauch and D. Zerwas, "Measuring Supersymmetry," Eur. Phys. J. C **54**, 617 (2008) [arXiv:0709.3985 [hep-ph]];

[19] R. Lafaye, T. Plehn, M. Rauch, D. Zerwas and M. Duhrssen, "Measuring the Higgs Sector," JHEP **0908**, 009 (2009) [arXiv:0904.3866 [hep-ph]].

[20] J. Wess and B. Zumino, "Supergauge Transformations in Four-Dimensions," Nucl. Phys. B **70**, 39 (1974).

[21] S. P. Martin, "A Supersymmetry primer," Adv. Ser. Direct. High Energy Phys. **21**, 1 (2010) [hep-ph/9709356].

[22] D. B. Kaplan and H. Georgi, "SU(2) x U(1) Breaking by Vacuum Misalignment," Phys. Lett. **136B**, 183 (1984).

[23] D. B. Kaplan, H. Georgi and S. Dimopoulos, "Composite Higgs Scalars," Phys. Lett. **136B**, 187 (1984).

[24] T. Banks, "CONSTRAINTS ON SU(2) x U(1) BREAKING BY VACUUM MISALIGNMENT," Nucl. Phys. B **243**, 125 (1984).

[25] K. Agashe, R. Contino and A. Pomarol, "The Minimal composite Higgs model," Nucl. Phys. B **719**, 165 (2005) [hep-ph/0412089].

[26] N. Arkani-Hamed, S. Dimopoulos and G. R. Dvali, "The Hierarchy problem and new dimensions at a millimeter," Phys. Lett. B **429**, 263 (1998) [hep-ph/9803315].

[27] N. Arkani-Hamed, S. Dimopoulos and G. R. Dvali, "Phenomenology, astrophysics and cosmology of theories with submillimeter dimensions and TeV scale quantum gravity," Phys. Rev. D **59**, 086004 (1999) [hep-ph/9807344].

[28] L. Randall and R. Sundrum, "A Large mass hierarchy from a small extra dimension," Phys. Rev. Lett. **83**, 3370 (1999) [hep-ph/9905221].

[29] T. Appelquist, H. C. Cheng and B. A. Dobrescu, "Bounds on universal extra dimensions," Phys. Rev. D **64**, 035002 (2001) [hep-ph/0012100].

[30] P. A. R. Ade *et al.* [Planck Collaboration], "Planck 2015 results. XIII. Cosmological parameters," Astron. Astrophys. **594**, A13 (2016) [arXiv:1502.01589 [astro-ph.CO]].

[31] J. Aalbers *et al.* [DARWIN Collaboration], "DARWIN: towards the ultimate dark matter detector," JCAP **1611**, 017 (2016) [arXiv:1606.07001 [astro-ph.IM]].

[32] E. Aprile [XENON1T Collaboration], "The XENON1T Dark Matter Search Experiment," Springer Proc. Phys. **148**, 93 (2013) [arXiv:1206.6288 [astro-ph.IM]].

[33] D. S. Akerib *et al.* [LUX Collaboration], "Results from a search for dark matter in the complete LUX exposure," Phys. Rev. Lett. **118**, no. 2, 021303 (2017) [arXiv:1608.07648 [astro-ph.CO]].

[34] A. M. Sirunyan *et al.* [CMS Collaboration], "Search for high-mass Zγ resonances in proton-proton collisions at $\sqrt{s} = 8$ and 13 TeV using jet substructure techniques," Phys. Lett. B **772**, 363 (2017) [arXiv:1612.09516 [hep-ex]].

[35] M. Aaboud *et al.* [ATLAS Collaboration], "Search for new phenomena in final states with an energetic jet and large missing transverse momentum in pp collisions at $\sqrt{s} = 13$ TeV using the ATLAS detector," Phys. Rev. D **94**, no. 3, 032005 (2016) [arXiv:1604.07773 [hep-ex]].

[36] J. Brehmer, "New Ideas for Effective Higgs Measurements," PhD thesis, Heidelberg University, 2017.

[37] C. Adam, J. -L. Kneur, R. Lafaye, T. Plehn, M. Rauch and D. Zerwas, "Measuring Unification," Eur. Phys. J. C **71**, 1520 (2011) [arXiv:1007.2190 [hep-ph]];

[38] E. Turlay, R. Lafaye, T. Plehn, M. Rauch and D. Zerwas, "Measuring Supersymmetry with Heavy Scalars," J. Phys. G **38**, 035003 (2011) [arXiv:1011.0759 [hep-ph]].

[39] S. Henrot-Versille, R. Lafaye, T. Plehn, M. Rauch, D. Zerwas, S. Plaszczynski, B. Rouille d'Orfeuil and M. Spinelli, "Constraining Supersymmetry using the relic density and the Higgs boson," Phys. Rev. D **89**, no. 5, 055017 (2014) [arXiv:1309.6958 [hep-ph]].

[40] M. Klute, R. Lafaye, T. Plehn, M. Rauch and D. Zerwas, "Measuring Higgs Couplings from LHC Data," Phys. Rev. Lett. **109**, 101801 (2012) [arXiv:1205.2699 [hep-ph]].

[41] D. López-Val, T. Plehn and M. Rauch, "Measuring extended Higgs sectors as a consistent free couplings model," JHEP **1310**, 134 (2013) [arXiv:1308.1979 [hep-ph]].

[42] T. Corbett, O. J. P. Eboli, D. Goncalves, J. Gonzalez-Fraile, T. Plehn and M. Rauch, "The Higgs Legacy of the LHC Run I," JHEP **1508**, 156 (2015) [arXiv:1505.05516 [hep-ph]].

[43] K. Cranmer, "Practical Statistics for the LHC," arXiv:1503.07622 [physics.data-an].

[44] Neyman, J. and Pearson, E. S., "On the Problem of the Most Efficient Tests of Statistical Hypotheses," Philosophical Transactions of the Royal Society of London A: Mathematical, Physical and Engineering Sciences, no. 231, 289–337 (1933).

[45] S. S. Wilks, "The Large-Sample Distribution of the Likelihood Ratio for Testing Composite Hypotheses," Annals Math. Statist. **9**, no. 1, 60 (1938).

[46] G. Aad *et al.* [ATLAS Collaboration], "Measurements of $W\gamma$ and $Z\gamma$ production in pp collisions at $\sqrt{s}$=7 TeV with the ATLAS detector at the LHC," Phys. Rev. D **87**, no. 11, 112003 (2013) Erratum: [Phys. Rev. D **91**, no. 11, 119901 (2015)] [arXiv:1302.1283 [hep-ex]].

[47] A. Höcker, H. Lacker, S. Laplace and F. Le Diberder, "A new approach to a global fit of the CKM matrix," Eur. Phys. J. C **21**, 225 (2001) [arXiv:hep-ph/0104062].

[48]

[49] F. James and M. Roos, "Minuit: A System for Function Minimization and Analysis of the Parameter Errors and Correlations," Comput. Phys. Commun. **10**, 343 (1975).

[50] J. A. Nelder and R. Mead, "A Simplex Method for Function Minimization," Comput. J. **7**, 308 (1965).

[51] W. C. Davidon, "Variable Metric Method For Minimization," ANL-5990-Rev. 2, ANL-5990.

[52] R. Fletcher, "A new approach to variable metric algorithms," The Computer Journal, **13**, 3 (1970).

[53] A. Djouadi, J. -L. Kneur and G. Moultaka, "SuSpect: A Fortran code for the supersymmetric and Higgs particle spectrum in the MSSM," Comput. Phys. Commun. **176**, 426 (2007) [arXiv:hep-ph/0211331];

[54] G. Brooijmans *et al.*, "Les Houches 2011: Physics at TeV Colliders New Physics Working Group Report," arXiv:1203.1488 [hep-ph].

[55] A. Djouadi, J. Kalinowski and M. Spira, "HDECAY: A Program for Higgs boson decays in the standard model and its supersymmetric extension," Comput. Phys. Commun. **108**, 56 (1998) [arXiv:hep-ph/9704448];

[56] M. Mühlleitner, A. Djouadi and Y. Mambrini, "SDECAY: A Fortran code for the decays of the supersymmetric particles in the MSSM," Comput. Phys. Commun. **168**, 46 (2005) [arXiv:hep-ph/0311167];

[57] A. Djouadi, M. M. Mühlleitner and M. Spira, "Decays of supersymmetric particles: The program SUSY-HIT (SUspect-SdecaY-Hdecay-InTerface)," Acta Phys. Polon. B **38**, 635 (2007) [arXiv:hep-ph/0609292].

[58] S. Heinemeyer, W. Hollik, A. M. Weber and G. Weiglein, "Z Pole Observables in the MSSM," JHEP **0804**, 039 (2008). [arXiv:0710.2972 [hep-ph]]. A. Weber, private communication.

[59] U. Ellwanger, J. F. Gunion and C. Hugonie, "NMHDECAY: A Fortran code for the Higgs masses, couplings and decay widths in the NMSSM," JHEP **0502**, 066 (2005) [hep-ph/0406215].

[60] U. Ellwanger and C. Hugonie, "NMHDECAY 2.0: An Updated program for sparticle masses, Higgs masses, couplings and decay widths in the NMSSM," Comput. Phys. Commun. **175**, 290 (2006) [hep-ph/0508022].

[61] G. Belanger, F. Boudjema, C. Hugonie, A. Pukhov and A. Semenov, "Relic density of dark matter in the NMSSM," JCAP **0509**, 001 (2005) [hep-ph/0505142].

[62] U. Ellwanger and C. Hugonie, "NMSPEC: A Fortran code for the sparticle and Higgs masses in the NMSSM with GUT scale boundary conditions," Comput. Phys. Commun. **177**, 399 (2007) [hep-ph/0612134].

[63] G. Belanger, F. Boudjema, P. Brun, A. Pukhov, S. Rosier-Lees, P. Salati and A. Semenov, "Indirect search for dark matter with micrOMEGAs2.4," Comput. Phys. Commun. **182**, 842 (2011) [arXiv:1004.1092 [hep-ph]].

[64] R. Brun and F. Rademakers, "ROOT: An object oriented data analysis framework," Nucl. Instrum. Meth. A **389**, 81 (1997).

[65] F. Zwicky, "Die Rotverschiebung von extragalaktischen Nebeln," Helv. Phys. Acta **6**, 110 (1933) [Gen. Rel. Grav. **41**, 207 (2009)].

[66] M. Bradac, S. W. Allen, T. Treu, H. Ebeling, R. Massey, R. G. Morris, A. von der Linden and D. Applegate, "Revealing the properties of dark matter in the merging cluster MACSJ0025.4-1222," Astrophys. J. **687**, 959 (2008) [arXiv:0806.2320 [astro-ph]].

[67] C. L. Bennett *et al.*, "Cosmic temperature fluctuations from two years of COBE differential microwave radiometers observations," Astrophys. J. **436**, 423 (1994) [astro-ph/9401012].

[68] D. N. Spergel *et al.* [WMAP Collaboration], "First year Wilkinson Microwave Anisotropy Probe (WMAP) observations: Determination of cosmological parameters," Astrophys. J. Suppl. **148**, 175 (2003) [astro-ph/0302209].

[69] V. Springel, "The Cosmological simulation code GADGET-2," Mon. Not. Roy. Astron. Soc. **364**, 1105 (2005) [astro-ph/0505010].

[70] M. Milgrom, "A Modification of the Newtonian dynamics as a possible alternative to the hidden mass hypothesis," Astrophys. J. **270**, 365 (1983).

[71] H. Goldberg, "Constraint On The Photino Mass From Cosmology," Phys. Rev. Lett. **50**, 1419 (1983); Erratum: [Phys. Rev. Lett. **103**, 099905 (2009)].

[72] M. Drees and M. M. Nojiri, "The Neutralino relic density in minimal $N = 1$ supergravity," Phys. Rev. D **47**, 376 (1993) [arXiv:hep-ph/9207234];

[73] J. R. Ellis, J. S. Hagelin, D. V. Nanopoulos, K. A. Olive and M. Srednicki, "Supersymmetric Relics From The Big Bang," Nucl. Phys. B **238**, 453 (1984);

[74] G. Jungman, M. Kamionkowski and K. Griest, "Supersymmetric dark matter," Phys. Rept. **267**, 195 (1996) [arXiv:hep-ph/9506380];

[75] G. Bertone, D. Hooper and J. Silk, "Particle dark matter: Evidence, candidates and constraints," Phys. Rept. **405**, 279 (2005) [arXiv:hep-ph/0404175];

[76] S. Dodelson and L. M. Widrow, "Sterile-neutrinos as dark matter," Phys. Rev. Lett. **72**, 17 (1994) [arXiv:hep-ph/9303287].

[77] S. Weinberg, "A New Light Boson?," Phys. Rev. Lett. **40**, 223 (1978).

[78] F. Wilczek, "Problem of Strong p and t Invariance in the Presence of Instantons," Phys. Rev. Lett. **40**, 279 (1978).

[79] H. P. Nilles, "Supersymmetry, Supergravity and Particle Physics," Phys. Rept. **110**, 1 (1984).

[80] E. W. Kolb, D. J. H. Chung and A. Riotto, "WIMPzillas!," In *Heidelberg 1998, Dark matter in astrophysics and particle physics 1998* 592-614 [hep-ph/9810361].

[81] S. R. Coleman, "Q Balls," Nucl. Phys. B **262**, 263 (1985) Erratum: [Nucl. Phys. B **269**, 744 (1986)].

[82] A. Kusenko and M. E. Shaposhnikov, "Supersymmetric Q balls as dark matter," Phys. Lett. B **418**, 46 (1998) [hep-ph/9709492].

[83] G. D. Starkman, A. Gould, R. Esmailzadeh and S. Dimopoulos, "Opening the Window on Strongly Interacting Dark Matter," Phys. Rev. D **41**, 3594 (1990).

[84] Y. Hochberg, E. Kuflik, T. Volansky and J. G. Wacker, "Mechanism for Thermal Relic Dark Matter of Strongly Interacting Massive Particles," Phys. Rev. Lett. **113**, 171301 (2014) [arXiv:1402.5143 [hep-ph]].

[85] E. W. Kolb and M. S. Turner, "The Early Universe," Front. Phys. **69**, 1 (1990).

[86] L. Goodenough and D. Hooper, "Possible Evidence For Dark Matter Annihilation In The Inner Milky Way From The Fermi Gamma Ray Space Telescope," arXiv:0910.2998 [hep-ph];

[87] D. Hooper and L. Goodenough, "Dark Matter Annihilation in The Galactic Center As Seen by the Fermi Gamma Ray Space Telescope," Phys. Lett. B **697** (2011) 412 [arXiv:1010.2752 [hep-ph]].

[88] D. Hooper and T. Linden, "On The Origin Of The Gamma Rays From The Galactic Center," Phys. Rev. D **84**, 123005 (2011) [arXiv:1110.0006 [astro-ph.HE]];

[89] K. N. Abazajian and M. Kaplinghat, "Detection of a Gamma-Ray Source in the Galactic Center Consistent with Extended Emission from Dark Matter Annihilation and Concentrated Astrophysical Emission," Phys. Rev. D **86**, 083511 (2012) Erratum: [Phys. Rev. D **87**, 129902 (2013)]; [arXiv:1207.6047 [astro-ph.HE]];

[90] D. Hooper and T. R. Slatyer, "Two Emission Mechanisms in the Fermi Bubbles: A Possible Signal of Annihilating Dark Matter," Phys. Dark Univ. **2**, 118 (2013) [arXiv:1302.6589 [astro-ph.HE]];

[91] C. Gordon and O. Macias, "Dark Matter and Pulsar Model Constraints from Galactic Center Fermi-LAT Gamma Ray Observations," Phys. Rev. D **88**, no. 8, 083521 (2013) Erratum: [Phys. Rev. D **89**, no. 4, 049901 (2014)]; [arXiv:1306.5725 [astro-ph.HE]];

[92] W. C. Huang, A. Urbano and W. Xue, "Fermi Bubbles under Dark Matter Scrutiny. Part I: Astrophysical Analysis," arXiv:1307.6862 [hep-ph];

[93] T. Daylan, D. P. Finkbeiner, D. Hooper, T. Linden, S. K. N. Portillo, N. L. Rodd and T. R. Slatyer, "The characterization of the gamma-ray signal from the central Milky Way: A case for annihilating dark matter," Phys. Dark Univ. **12**, 1 (2016) [arXiv:1402.6703 [astro-ph.HE]];

[94] K. N. Abazajian, N. Canac, S. Horiuchi and M. Kaplinghat, "Astrophysical and Dark Matter Interpretations of Extended Gamma-Ray Emission from the Galactic Center," Phys. Rev. D **90**, no. 2, 023526 (2014) [arXiv:1402.4090 [astro-ph.HE]];

[95] A. Alves, S. Profumo, F. S. Queiroz and W. Shepherd, "Effective field theory approach to the Galactic Center gamma-ray excess," Phys. Rev. D **90**, no. 11, 115003 (2014) [arXiv:1403.5027 [hep-ph]].

[96] B. Zhou, Y. F. Liang, X. Huang, X. Li, Y. Z. Fan, L. Feng and J. Chang, "GeV excess in the Milky Way: The role of diffuse galactic gamma-ray emission templates," Phys. Rev. D **91**, no. 12, 123010 (2015) [arXiv:1406.6948 [astro-ph.HE]];

[97] F. Calore, I. Cholis and C. Weniger, "Background Model Systematics for the Fermi GeV Excess," JCAP **1503**, 038 (2015) [arXiv:1409.0042 [astro-ph.CO]];

[98] K. N. Abazajian, N. Canac, S. Horiuchi, M. Kaplinghat and A. Kwa, "Discovery of a New Galactic Center Excess Consistent with Upscattered Starlight," JCAP **1507**, no. 07, 013 (2015) [arXiv:1410.6168 [astro-ph.HE]];

[99] E. Carlson, T. Linden and S. Profumo, "Improved Cosmic-Ray Injection Models and the Galactic Center Gamma-Ray Excess," Phys. Rev. D **94**, no. 6, 063504 (2016) [arXiv:1603.06584 [astro-ph.HE]].

[100] F. Calore, I. Cholis, C. McCabe and C. Weniger, "A Tale of Tails: Dark Matter Interpretations of the Fermi GeV Excess in Light of Background Model Systematics," Phys. Rev. D **91**, no. 6, 063003 (2015) [arXiv:1411.4647 [hep-ph]].

[101] I. Cholis, C. Evoli, F. Calore, T. Linden, C. Weniger and D. Hooper, "The Galactic Center GeV Excess from a Series of Leptonic Cosmic-Ray Outbursts," JCAP **1512**, no. 12, 005 (2015) [arXiv:1506.05119 [astro-ph.HE]].

[102] D. Hooper, I. Cholis, T. Linden, J. Siegal-Gaskins and T. Slatyer, "Pulsars Cannot Account for the Inner Galaxy's GeV Excess," Phys. Rev. D **88**, 083009 (2013) [arXiv:1305.0830 [astro-ph.HE]];

[103] E. Carlson and S. Profumo, "Cosmic Ray Protons in the Inner Galaxy and the Galactic Center Gamma-Ray Excess," Phys. Rev. D **90**, no. 2, 023015 (2014) [arXiv:1405.7685 [astro-ph.HE]];

[104] J. Petrovic, P. D. Serpico and G. Zaharijas, "Galactic Center gamma-ray "excess" from an active past of the Galactic Centre?," JCAP **1410**, no. 10, 052 (2014) [arXiv:1405.7928 [astro-ph.HE]];

[105] I. Cholis, D. Hooper and T. Linden, "Challenges in Explaining the Galactic Center Gamma-Ray Excess with Millisecond Pulsars," JCAP **1506**, no. 06, 043 (2015) [arXiv:1407.5625 [astro-ph.HE]];

[106] O. Macias, C. Gordon, R. M. Crocker, B. Coleman, D. Paterson, S. Horiuchi and M. Pohl, "Discovery of Gamma-Ray Emission from the X-shaped Bulge of the Milky Way," arXiv:1611.06644 [astro-ph.HE].

[107] S. K. Lee, M. Lisanti and B. R. Safdi, "Distinguishing Dark Matter from Unresolved Point Sources in the Inner Galaxy with Photon Statistics," JCAP **1505** (2015) no.05, 056 [arXiv:1412.6099 [astro-ph.CO]];

[108] R. Bartels, S. Krishnamurthy and C. Weniger, "Strong support for the millisecond pulsar origin of the Galactic center GeV excess," Phys. Rev. Lett. **116**, no. 5, 051102 (2016) [arXiv:1506.05104 [astro-ph.HE]];

[109] S. K. Lee, M. Lisanti, B. R. Safdi, T. R. Slatyer and W. Xue, "Evidence for Unresolved γ-Ray Point Sources in the Inner Galaxy," Phys. Rev. Lett. **116**, no. 5, 051103 (2016) [arXiv:1506.05124 [astro-ph.HE]];

[110] S. D. McDermott, P. J. Fox, I. Cholis and S. K. Lee, "Wavelet-Based Techniques for the Gamma-Ray Sky," JCAP **1607**, no. 07, 045 (2016) [arXiv:1512.00012 [astro-ph.HE]].

[111] S. Horiuchi, M. Kaplinghat and A. Kwa, "Investigating the Uniformity of the Excess Gamma rays towards the Galactic Center Region," JCAP **1611**, no. 11, 053 (2016) [arXiv:1604.01402 [astro-ph.HE]].

[112] A. Achterberg, S. Amoroso, S. Caron, L. Hendriks, R. Ruiz de Austri and C. Weniger, "A description of the Galactic Center excess in the Minimal Supersymmetric Standard Model," JCAP **1508**, no. 08, 006 (2015) [arXiv:1502.05703 [hep-ph]].

[113] G. Bertone, F. Calore, S. Caron, R. Ruiz, J. S. Kim, R. Trotta and C. Weniger, "Global analysis of the pMSSM in light of the Fermi GeV excess: prospects for the LHC Run-II and astroparticle experiments," JCAP **1604**, no. 04, 037 (2016) [arXiv:1507.07008 [hep-ph]].

[114] M. Ackermann *et al.* [Fermi-LAT Collaboration], "The Fermi Large Area Telescope On Orbit: Event Classification, Instrument Response Functions, and Calibration," Astrophys. J. Suppl. **203** (2012) 4 [arXiv:1206.1896 [astro-ph.IM]].

[115] J. F. Navarro, C. S. Frenk and S. D. M. White, "The Structure of cold dark matter halos," Astrophys. J. **462**, 563 (1996) [astro-ph/9508025].

[116] K. N. Abazajian and R. E. Keeley, "Bright gamma-ray Galactic Center excess and dark dwarfs: Strong tension for dark matter annihilation despite Milky Way halo profile and diffuse emission uncertainties," Phys. Rev. D **93**, no. 8, 083514 (2016) [arXiv:1510.06424 [hep-ph]].

[117] U. Ellwanger, C. Hugonie and A. M. Teixeira, "The Next-to-Minimal Supersymmetric Standard Model," Phys. Rept. **496**, 1 (2010) [arXiv:0910.1785 [hep-ph]].

[118] S. R. Coleman and J. Mandula, "All Possible Symmetries of the S Matrix," Phys. Rev. **159**, 1251 (1967).

[119] D. Tucker-Smith and N. Weiner, "The Status of inelastic dark matter," Phys. Rev. D **72**, 063509 (2005) [hep-ph/0402065].

[120] A. Heister *et al.* [ALEPH Collaboration], "Search for scalar leptons in e+ e- collisions at center-of-mass energies up to 209-GeV," Phys. Lett. B **526**, 206 (2002) [arXiv:hep-ex/0112011].

[121] A. Heister *et al.* [ALEPH Collaboration], "Absolute mass lower limit for the lightest neutralino of the MSSM from e+ e- data at s**(1/2) up to 209-GeV," Phys. Lett. B **583**, 247 (2004).

[122] J. Abdallah *et al.* [DELPHI Collaboration], "Searches for supersymmetric particles in e+ e- collisions up to 208-GeV and interpretation of the results within the MSSM," Eur. Phys. J. C **31**, 421 (2003) [arXiv:hep-ex/0311019].

[123] P. Achard *et al.* [L3 Collaboration], "Search for scalar leptons and scalar quarks at LEP," Phys. Lett. B **580**, 37 (2004) [arXiv:hep-ex/0310007].

[124] G. Abbiendi *et al.* [OPAL Collaboration], "Search for anomalous production of dilepton events with missing transverse momentum in e+ e- collisions at s**(1/2) = 183-Gev to 209-GeV," Eur. Phys. J. C **32**, 453 (2004) [arXiv:hep-ex/0309014].

[125] A. Heister *et al.* [ALEPH Collaboration], "Search for scalar quarks in e^+e^- collisions at $\sqrt{s}$ up to 209-GeV," Phys. Lett. B **537**, 5 (2002) [arXiv:hep-ex/0204036].

[126] G. Abbiendi *et al.* [OPAL Collaboration], "Search for scalar top and scalar bottom quarks at LEP," Phys. Lett. B **545**, 272 (2002) Erratum: [Phys. Lett. B **548**, 258 (2002)] [arXiv:hep-ex/0209026].

[127] A. Heister *et al.* [ALEPH Collaboration], "Search for charginos nearly mass degenerate with the lightest neutralino in e+ e- collisions at center-of-mass energies up to 209-GeV," Phys. Lett. B **533**, 223 (2002) [arXiv:hep-ex/0203020].

[128] M. Acciarri *et al.* [L3 Collaboration], "Searches for scalar quarks in e^+e^- interactions at $\sqrt{S}$ = 189-GeV," Phys. Lett. B **471**, 308 (1999) [arXiv:hep-ex/9910020].

[129] M. Maniatis, "The Next-to-Minimal Supersymmetric extension of the Standard Model reviewed," Int. J. Mod. Phys. A **25**, 3505 (2010) [arXiv::0906.0777 [hep-ph]].

[130] J. R. Ellis, J. F. Gunion, H. E. Haber, L. Roszkowski and F. Zwirner, "Higgs Bosons in a Nonminimal Supersymmetric Model," Phys. Rev. D **39**, 844 (1989).

[131] M. Drees, "Supersymmetric Models with Extended Higgs Sector," Int. J. Mod. Phys. A **4**, 3635 (1989).

[132] J. R. Espinosa and M. Quiros, "On Higgs boson masses in nonminimal supersymmetric standard models," Phys. Lett. B **279**, 92 (1992).

[133] U. Ellwanger, M. Rausch de Traubenberg and C. A. Savoy, "Particle spectrum in supersymmetric models with a gauge singlet," Phys. Lett. B **315**, 331 (1993) [hep-ph/9307322].

[134] for general aspects of the singlet/singlino in the NMSSM see e. g. U. Ellwanger and C. Hugonie, "Neutralino cascades in the (M+1)SSM," Eur. Phys. J. C **5**, 723 (1998) [hep-ph/9712300].

[135] A. Dedes, C. Hugonie, S. Moretti and K. Tamvakis, "Phenomenology of a new minimal supersymmetric extension of the standard model," Phys. Rev. D **63**, 055009 (2001) [hep-ph/0009125].

[136] S. Y. Choi, D. J. Miller and P. M. Zerwas, "The Neutralino sector of the next-to-minimal supersymmetric standard model," Nucl. Phys. B **711**, 83 (2005) [hep-ph/0407209].

[137] V. Barger, P. Langacker and G. Shaughnessy, "Neutralino signatures of the singlet extended MSSM," Phys. Lett. B **644**, 361 (2007) [hep-ph/0609068].

[138] K. Cheung and T. J. Hou, "Light Pseudoscalar Higgs boson in Neutralino Decays in the Next-to-Minimal Supersymmetric Standard Model," Phys. Lett. B **674**, 54 (2009) [arXiv:0809.1122 [hep-ph]].

[139] O. Stal and G. Weiglein, "Light NMSSM Higgs bosons in SUSY cascade decays at the LHC," JHEP **1201**, 071 (2012) [arXiv:1108.0595 [hep-ph]].

[140] D. G. Cerdeño, P. Ghosh, C. B. Park and M. Peiró, "Collider signatures of a light NMSSM pseudoscalar in neutralino decays in the light of LHC results," JHEP **1402**, 048 (2014) [arXiv:1307.7601 [hep-ph]].

[141] U. Ellwanger and A. M. Teixeira, "NMSSM with a singlino LSP: possible challenges for searches for supersymmetry at the LHC," JHEP **1410**, 113 (2014) [arXiv:1406.7221 [hep-ph]].

[142] F. Franke and H. Fraas, "Neutralinos and Higgs bosons in the next-to-minimal supersymmetric standard model," Int. J. Mod. Phys. A **12**, 479 (1997) [hep-ph/9512366].

[143] D. J. Miller, R. Nevzorov and P. M. Zerwas, "The Higgs sector of the next-to-minimal supersymmetric standard model," Nucl. Phys. B **681**, 3 (2004) [hep-ph/0304049].

[144] U. Ellwanger and C. Hugonie, "Yukawa induced radiative corrections to the lightest Higgs boson mass in the NMSSM," Phys. Lett. B **623**, 93 (2005) [hep-ph/0504269].

[145] G. Degrassi and P. Slavich, "On the radiative corrections to the neutral Higgs boson masses in the NMSSM," Nucl. Phys. B **825**, 119 (2010) [arXiv:0907.4682 [hep-ph]].

[146] M. Masip, R. Munoz-Tapia and A. Pomarol, "Limits on the mass of the lightest Higgs in supersymmetric models," Phys. Rev. D **57**, R5340 (1998) [hep-ph/9801437].

[147] M. A. Diaz, T. A. ter Veldhuis and T. J. Weiler, "Updated: Higgs mass bounds separate models of electroweak symmetry breaking," Phys. Rev. D **54**, 5855 (1996) [hep-ph/9407357].

[148] U. Ellwanger and C. Hugonie, "Masses and couplings of the lightest Higgs bosons in the (M+1) SSM," Eur. Phys. J. C **25**, 297 (2002) [hep-ph/9909260].

[149] M. D. Goodsell, K. Nickel and F. Staub, "Two-loop corrections to the Higgs masses in the NMSSM," Phys. Rev. D **91**, 035021 (2015) [arXiv:1411.4665 [hep-ph]].

[150] L. E. Ibanez, "Locally Supersymmetric SU(5) Grand Unification," Phys. Lett. **118B**, 73 (1982).

[151] J. R. Ellis, D. V. Nanopoulos and K. Tamvakis, "Grand Unification in Simple Supergravity," Phys. Lett. **121B**, 123 (1983).

[152] L. Alvarez-Gaume, J. Polchinski and M. B. Wise, "Minimal Low-Energy Supergravity," Nucl. Phys. B **221**, 495 (1983).

[153] K. Inoue, A. Kakuto, H. Komatsu and S. Takeshita, "Aspects of Grand Unified Models with Softly Broken Supersymmetry," Prog. Theor. Phys. **68**, 927 (1982) Erratum: [Prog. Theor. Phys. **70**, 330 (1983)].

[154] A. H. Chamseddine, R. L. Arnowitt and P. Nath, "Locally Supersymmetric Grand Unification," Phys. Rev. Lett. **49**, 970 (1982).

[155] A. Djouadi, U. Ellwanger and A. M. Teixeira, "The Constrained next-to-minimal supersymmetric standard model," Phys. Rev. Lett. **101**, 101802 (2008) [arXiv:0803.0253 [hep-ph]].

[156] T. Cohen and J. G. Wacker, "Here be Dragons: The Unexplored Continents of the CMSSM," JHEP **1309**, 061 (2013) [arXiv:1305.2914 [hep-ph]].

[157] A. Fowlie, K. Kowalska, L. Roszkowski, E. M. Sessolo and Y. -L. S. Tsai, "Dark matter and collider signatures of the MSSM," Phys. Rev. D **88**, 055012 (2013) [arXiv:1306.1567 [hep-ph]];

[158] C. Strege, G. Bertone, F. Feroz, M. Fornasa, R. Ruiz de Austri and R. Trotta, "Global Fits of the cMSSM and NUHM including the LHC Higgs discovery and new XENON100 constraints," JCAP **1304**, 013 (2013) [arXiv:1212.2636 [hep-ph]];

[159] B. Bhattacherjee, M. Chakraborti, A. Chakraborty, U. Chattopadhyay, D. Das and D. K. Ghosh, "Implications of 98 GeV and 125 GeV Higgs scenario in non-decoupling SUSY with updated ATLAS, CMS and PLANCK data," Phys. Rev. D **88**, no. 3, 035011 (2013) [arXiv:1305.4020 [hep-ph]];

[160] M. Cahill-Rowley, J. Hewett, A. Ismail and T. Rizzo, "Constraints on Higgs Properties and SUSY Partners in the pMSSM," arXiv:1308.0297 [hep-ph];

[161] O. Buchmüller, R. Cavanaugh, M. Citron, A. De Roeck, M. J. Dolan, J. R. Ellis, H. Flacher and S. Heinemeyer *et al.*, "The CMSSM and NUHM1 in Light of 7 TeV LHC, B_s to mu+mu- and XENON100 Data," Eur. Phys. J. C **72**, 2243 (2012) [arXiv:1207.7315 [hep-ph]].

[162] C. Cheung, M. Papucci, D. Sanford, N. R. Shah and K. M. Zurek, "NMSSM Interpretation of the Galactic Center Excess," Phys. Rev. D **90**, no. 7, 075011 (2014) [arXiv:1406.6372 [hep-ph]];

[163] A. Berlin, D. Hooper and S. D. McDermott, "Simplified Dark Matter Models for the Galactic Center Gamma-Ray Excess," Phys. Rev. D **89**, no. 11, 115022 (2014) [arXiv:1404.0022 [hep-ph]];
Griest:1990kh,Ellis:1998kh,

[164] K. Griest and D. Seckel, "Three exceptions in the calculation of relic abundances," Phys. Rev. D **43**, 3191 (1991);

[165] J. R. Ellis, T. Falk and K. A. Olive, "Neutralino - Stau coannihilation and the cosmological upper limit on the mass of the lightest supersymmetric particle," Phys. Lett. B **444**, 367 (1998) [arXiv:hep-ph/9810360].

[166] C. Boehm, A. Djouadi and M. Drees, "Light scalar top quarks and supersymmetric dark matter," Phys. Rev. D **62**, 035012 (2000) [arXiv:hep-ph/9911496].

[167] P. Binetruy, G. Girardi and P. Salati, "Constraints on a System of Two Neutral Fermions From Cosmology," Nucl. Phys. B **237**, 285 (1984);

[168] S. Mizuta and M. Yamaguchi, "Coannihilation effects and relic abundance of Higgsino dominant LSP(s)," Phys. Lett. B **298**, 120 (1993) [arXiv:hep-ph/9208251].

[169] J. Bramante, N. Desai, P. Fox, A. Martin, B. Ostdiek and T. Plehn, "Towards the Final Word on Neutralino Dark Matter," Phys. Rev. D **93**, no. 6, 063525 (2016) [arXiv:1510.03460 [hep-ph]].

[170] for a recent update see A. Freitas, "Higher-order electroweak corrections to the partial widths and branching ratioJHEP **1404**, 070 (2014) [arXiv:1401.2447 [hep-ph]].

[171] for the updated LHC see e. g. C. Bernaciak, T. Plehn, P. Schichtel and J. Tattersall, "Spying an invisible Higgs boson," Phys. Rev. D **91**, 035024 (2015) [arXiv:1411.7699 [hep-ph]].

[172] for an exceptionally beautiful set of plots on relic neutralinos see J. Bramante, P. J. Fox, A. Martin, B. Ostdiek, T. Plehn, T. Schell and M. Takeuchi, "Relic neutralino surface at a 100 TeV collider," Phys. Rev. D **91**, no. 5, 054015 (2015) [arXiv:1412.4789 [hep-ph]].

[173] M. Cahill-Rowley, J. Gainer, J. Hewett and T. Rizzo, "Towards a Supersymmetric Description of the Fermi Galactic Center Excess," JHEP **1502**, 057 (2015) [arXiv:1409.1573 [hep-ph]];

[174] T. Gherghetta, B. von Harling, A. D. Medina, M. A. Schmidt and T. Trott, "SUSY implications from WIMP annihilation into scalars at the Galactic Center," Phys. Rev. D **91**, 105004 (2015) [arXiv:1502.07173 [hep-ph]];

[175] R. Enberg, S. Munir, C. P. d. l. Heros and D. Werder, "Prospects for higgsino-singlino dark matter detection at IceCube and PINGU," arXiv:1506.05714 [hep-ph];

[176] J. Cao, L. Shang, P. Wu, J. M. Yang and Y. Zhang, "Interpreting the galactic center gamma-ray excess in the NMSSM," JHEP **1510**, 030 (2015) [arXiv:1506.06471 [hep-ph]].

[177] K. Freese, A. Lopez, N. R. Shah and B. Shakya, "MSSM A-funnel and the Galactic Center Excess: Prospects for the LHC and Direct Detection Experiments," JHEP **1604** (2016) 059 [arXiv:1509.05076 [hep-ph]];

[178] M. van Beekveld, W. Beenakker, S. Caron, R. Peeters and R. Ruiz de Austri, "This year's holiday present: Supersymmetry with Dark Matter is still natural," arXiv:1612.06333 [hep-ph].

[179] K. Hagiwara, S. Mukhopadhyay and J. Nakamura, "10 GeV neutralino dark matter and light stau in the MSSM," Phys. Rev. D **89**, no. 1, 015023 (2014) [arXiv:1308.6738 [hep-ph]].

[180] M. Abdullah, A. DiFranzo, A. Rajaraman, T. M. P. Tait, P. Tanedo and A. M. Wijangco, "Hidden on-shell mediators for the Galactic Center γ-ray excess," Phys. Rev. D **90**, no. 3, 035004 (2014) [arXiv:1404.6528 [hep-ph]];

[181] C. Balazs, T. Li, C. Savage and M. White, "Interpreting the Fermi-LAT gamma ray excess in the simplified framework," Phys. Rev. D **92**, no. 12, 123520 (2015) [arXiv:1505.06758 [hep-ph]];

[182] M. Escudero, D. Hooper and S. J. Witte, "Updated Collider and Direct Detection Constraints on Dark Matter Models for the Galactic Center Gamma-Ray Excess," JCAP **1702**, no. 02, 038 (2017) [arXiv:1612.06462 [hep-ph]].

[183] D. K. Ghosh, S. Mondal and I. Saha, "Confronting the Galactic Center Gamma Ray Excess With a Light Scalar Dark Matter," JCAP **1502**, no. 02, 035 (2015) [arXiv:1405.0206 [hep-ph]];

[184] A. Berlin, S. Gori, T. Lin and L. T. Wang, "Pseudoscalar Portal Dark Matter," Phys. Rev. D **92**, 015005 (2015) [arXiv:1502.06000 [hep-ph]].

[185] J. Huang, T. Liu, L. T. Wang and F. Yu, "Supersymmetric subelectroweak scale dark matter, the Galactic Center gamma-ray excess, and exotic decays of the 125 GeV Higgs boson," Phys. Rev. D **90**, no. 11, 115006 (2014) [arXiv:1407.0038 [hep-ph]];

[186] J. Guo, J. Li, T. Li and A. G. Williams, "NMSSM explanations of the Galactic center gamma ray excess and promising LHC searches," Phys. Rev. D **91**, no. 9, 095003 (2015) [arXiv:1409.7864 [hep-ph]];

[187] J. Cao, L. Shang, P. Wu, J. M. Yang and Y. Zhang, "Supersymmetry explanation of the Fermi Galactic Center excess and its test at LHC run II," Phys. Rev. D **91**, no. 5, 055005 (2015) [arXiv:1410.3239 [hep-ph]];

[188] X. J. Bi, L. Bian, W. Huang, J. Shu and P. F. Yin, "The interpretation for Galactic Center Excess and Electroweak Phase Transition in the NMSSM," Phys. Rev. D **92**, 023507 (2015) [arXiv:1503.03749 [hep-ph]].

[189] for an analysis based on preliminary Fermi–LAT results see e. g. P. Agrawal, B. Batell, P. J. Fox and R. Harnik, "WIMPs at the Galactic Center," JCAP **1505**, no. 05, 011 (2015) [arXiv:1411.2592 [hep-ph]].

[190] S. Liem, G. Bertone, F. Calore, R. Ruiz de Austri, T. M. P. Tait, R. Trotta and C. Weniger, "Effective Field Theory of Dark Matter: a Global Analysis," JHEP **1609**, 077 (2016) [arXiv:1603.05994 [hep-ph]];

[191] C. Karwin, S. Murgia, T. M. P. Tait, T. A. Porter and P. Tanedo, "Dark Matter Interpretation of the Fermi-LAT Observation Toward the Galactic Center," Phys. Rev. D **95**, no. 10, 103005 (2017) [arXiv:1612.05687 [hep-ph]].

[192] P. Bechtle, K. Desch and P. Wienemann, "Fittino, a program for determining MSSM parameters from collider observables using an iterative method," Comput. Phys. Commun. **174**, 47 (2006) [arXiv:hep-ph/0412012];

[193] P. Bechtle, T. Bringmann, K. Desch, H. Dreiner, M. Hamer, C. Hensel, M. Krämer and N. Nguyen *et al.*, "Constrained Supersymmetry after two years of LHC data: a global view with Fittino," JHEP **1206** (2012) 098 [arXiv:1204.4199 [hep-ph]].

[194] M. Ackermann *et al.* [Fermi-LAT Collaboration], "Searching for Dark Matter Annihilation from Milky Way Dwarf Spheroidal Galaxies with Six Years of Fermi Large Area Telescope Data," Phys. Rev. Lett. **115**, no. 23, 231301 (2015) [arXiv:1503.02641 [astro-ph.HE]].

[195] D. M. Pierce, J. A. Bagger, K. T. Matchev and R. j. Zhang, "Precision corrections in the minimal supersymmetric standard model," Nucl. Phys. B **491**, 3 (1997) [arXiv:hep-ph/9606211];

[196] T. Fritzsche and W. Hollik, "Complete one loop corrections to the mass spectrum of charginos and neutralinos in the MSSM," Eur. Phys. J. C **24**, 619 (2002) [arXiv:hep-ph/0203159];

[197] W. Oller, H. Eberl, W. Majerotto and C. Weber, "Analysis of the chargino and neutralino mass parameters at one loop level," Eur. Phys. J. C **29**, 563 (2003) [arXiv:hep-ph/0304006].

[198] U. Baur, T. Plehn and D. L. Rainwater, "Probing the Higgs selfcoupling at hadron colliders using rare decays," Phys. Rev. D **69**, 053004 (2004) [arXiv:hep-ph/0310056].

[199] A. Cuoco, B. Eiteneuer, J. Heisig and M. Krämer, "A global fit of the γ-ray galactic center excess within the scalar singlet Higgs portal model," JCAP **1606**, no. 06, 050 (2016) [arXiv:1603.08228 [hep-ph]].

[200] ATLAS and CMS Collaborations, "Combined Measurement of the Higgs Boson Mass in pp Collisions at $\sqrt{s} = 7$ and 8 TeV with the ATLAS and CMS Experiments," Phys. Rev. Lett. **114**, 191803 (2015) [arXiv:1503.07589 [hep-ex]].

[201] for a short history of MSSM studies see e. g. M. S. Carena, J. R. Espinosa, M. Quiros and C. E. M. Wagner, "Analytical expressions for radiatively corrected Higgs masses and couplings in the MSSM," Phys. Lett. B **355**, 209 (1995) [arXiv:hep-ph/9504316];

[202] H. E. Haber, R. Hempfling and A. H. Hoang, "Approximating the radiatively corrected Higgs mass in the minimal supersymmetric model," Z. Phys. C **75**, 539 (1997) [arXiv:hep-ph/9609331];

[203] S. Heinemeyer, W. Hollik and G. Weiglein, "The Masses of the neutral CP - even Higgs bosons in the MSSM: Accurate analysis at the two loop level," Eur. Phys. J. C **9**, 343 (1999) [arXiv:hep-ph/9812472];

[204] G. Degrassi, S. Heinemeyer, W. Hollik, P. Slavich and G. Weiglein, "Towards high-precision predictions for the MSSM Higgs sector," Eur. Phys. J. C **28**, 133 (2003) [arXiv:hep-ph/0212020];

[205] P. Kant, R. V. Harlander, L. Mihaila and M. Steinhauser, "Light MSSM Higgs boson mass to three-loop accuracy," JHEP **1008**, 104 (2010) [arXiv:1005.5709 [hep-ph]];

[206] T. Hahn, S. Heinemeyer, W. Hollik, H. Rzehak and G. Weiglein, "High-Precision Predictions for the Light CP -Even Higgs Boson Mass of the Minimal Supersymmetric Standard Model," Phys. Rev. Lett. **112**, no. 14, 141801 (2014) [arXiv:1312.4937 [hep-ph]];

[207] E. Bagnaschi, R. V. Harlander, S. Liebler, H. Mantler, P. Slavich and A. Vicini, "Towards precise predictions for Higgs-boson production in the MSSM," JHEP **1406**, 167 (2014) [arXiv:1404.0327 [hep-ph]];

[208] G. Degrassi, S. Di Vita and P. Slavich, "Two-loop QCD corrections to the MSSM Higgs masses beyond the effective-potential approximation," Eur. Phys. J. C **75**, no. 2, 61 (2015) [arXiv:1410.3432 [hep-ph]].

[209] G. W. Bennett *et al.* [Muon g-2 Collaboration], "Measurement of the positive muon anomalous magnetic moment to 0.7 ppm," Phys. Rev. Lett. **89**, 101804 (2002) Erratum: [Phys. Rev. Lett. **89**, 129903 (2002)] [hep-ex/0208001].

[210] G. W. Bennett *et al.* [Muon g-2 Collaboration], "Measurement of the negative muon anomalous magnetic moment to 0.7 ppm," Phys. Rev. Lett. **92**, 161802 (2004) [hep-ex/0401008].

[211] G. W. Bennett *et al.* [Muon g-2 Collaboration], "Final Report of the Muon E821 Anomalous Magnetic Moment Measurement at BNL," Phys. Rev. D **73**, 072003 (2006) [hep-ex/0602035]. http://pdg.lbl.gov/2014/reviews/rpp2014-rev-g-2-muon-anom-mag-moment.pdf

[212] S. Chen *et al.* [CLEO Collaboration], "Branching fraction and photon energy spectrum for $b \to s\gamma$," Phys. Rev. Lett. **87**, 251807 (2001) [hep-ex/0108032].

[213] J. P. Lees *et al.* [BaBar Collaboration], "Measurement of B($B \to X_s\gamma$), the $B \to X_s\gamma$ photon energy spectrum, and the direct CP asymmetry in $B \to X_{s+d}\gamma$ decays," Phys. Rev. D **86**, 112008 (2012) [arXiv:1207.5772 [hep-ex]].

[214] A. Limosani *et al.* [Belle Collaboration], "Measurement of Inclusive Radiative B-meson Decays with a Photon Energy Threshold of 1.7-GeV," Phys. Rev. Lett. **103**, 241801 (2009) [arXiv:0907.1384 [hep-ex]]. http://pdg.lbl.gov/2014/reviews/rpp2014-rev-b-meson-prod-decay.pdf

[215] LHCb Collaboration, "First Evidence for the Decay $B_s^0 \to \mu^+\mu^-$," Phys. Rev. Lett. **110**, 021801 (2013) [arXiv:1211.2674 [hep-ex]];

[216] CMS Collaboration, Phys. Rev. Lett. **111**, 101804 (2013); CMS and LHCb Collaborations, Nature **522**, 68 (2015) [arXiv:1411.4413 [hep-ex]].

[217] E. Aprile *et al.* [XENON100 Collaboration], "Dark Matter Results from 100 Live Days of XENON100 Data," Phys. Rev. Lett. **107**, 131302 (2011) [arXiv:1104.2549 [astro-ph.CO]];

[218] E. Aprile *et al.* [XENON100 Collaboration], "Dark Matter Results from 225 Live Days of XENON100 Data," Phys. Rev. Lett. **109**, 181301 (2012) [arXiv:1207.5988 [astro-ph.CO]].

[219] A. Tan *et al.* [PandaX-II Collaboration], "Dark Matter Results from First 98.7 Days of Data from the PandaX-II Experiment," Phys. Rev. Lett. **117**, no. 12, 121303 (2016) [arXiv:1607.07400 [hep-ex]]

[220] O. J. P. Eboli and D. Zeppenfeld, "Observing an invisible Higgs boson," Phys. Lett. B **495**, 147 (2000) [hep-ph/0009158].

[221] R. M. Godbole, M. Guchait, K. Mazumdar, S. Moretti and D. P. Roy, "Search for 'invisible' Higgs signals at LHC via associated production with gauge bosons," Phys. Lett. B **571**, 184 (2003) [hep-ph/0304137].

[222] G.-C. Cho, K. Hagiwara, J. Kanzaki, T. Plehn, D. Rainwater and T. Stelzer, "Weak boson fusion production of supersymmetric particles at the CERN LHC," Phys. Rev. D **73**, 054002 (2006) [hep-ph/0601063].

[223] M. Ackermann *et al.* [Fermi-LAT Collaboration], "Dark matter constraints from observations of 25 Milky Way satellite galaxies with the Fermi Large Area Telescope," Phys. Rev. D **89**, 042001 (2014) [arXiv:1310.0828 [astro-ph.HE]].

[224] [ATLAS Collaboration], "Search for invisible decays of a Higgs boson produced in association with a Z boson in ATLAS," ATLAS-CONF-2013-011.

[225] G. Aad *et al.* [ATLAS Collaboration], "Search for Invisible Decays of a Higgs Boson Produced in Association with a Z Boson in ATLAS," Phys. Rev. Lett. **112**, 201802 (2014) [arXiv:1402.3244 [hep-ex]].

[226] G. Aad *et al.* [ATLAS Collaboration], "Search for invisible decays of the Higgs boson produced in association with a hadronically decaying vector boson in pp collisions at $\sqrt{s}$ = 8 TeV with the ATLAS detector," Eur. Phys. J. C **75**, no. 7, 337 (2015) [arXiv:1504.04324 [hep-ex]].

[227] CMS Collaboration [CMS Collaboration], "Search for an Invisible Higgs Boson," CMS-PAS-HIG-13-013.

[228] CMS Collaboration [CMS Collaboration], "Search for invisible Higgs produced in association with a Z boson," CMS-PAS-HIG-13-018.

[229] [CMS Collaboration], "Search for the Higgs boson decaying to invisible particles produced in association with Z bosons decaying to bottom quarks," CMS-PAS-HIG-13-028.

[230] M. E. Chasco [CMS Collaboration], "Search for invisible Higgs boson production with the CMS detector at the LHC," arXiv:1310.1002 [hep-ex].

[231] CMS Collaboration [CMS Collaboration], "Search for invisible decays of Higgs bosons in the vector boson fusion production mode," CMS-PAS-HIG-14-038.

[232] S. Chatrchyan *et al.* [CMS Collaboration], "Search for invisible decays of Higgs bosons in the vector boson fusion and associated ZH production modes," Eur. Phys. J. C **74**, 2980 (2014) [arXiv:1404.1344 [hep-ex]].

[233] V. Khachatryan *et al.* [CMS Collaboration], "Search for exotic decays of a Higgs boson into undetectable particles and one or more photons," Phys. Lett. B **753**, 363 (2016) [arXiv:1507.00359 [hep-ex]].

[234] J. Kozaczuk and T. A. W. Martin, "Extending LHC Coverage to Light Pseudoscalar Mediators and Coy Dark Sectors," JHEP **1504**, 046 (2015) [arXiv:1501.07275 [hep-ph]].

[235] for a Higgs portal linked to invisible decays see e. g. V. Silveira and A. Zee, "Scalar Phantoms," Phys. Lett. **161B**, 136 (1985).

[236] J. McDonald, "Gauge singlet scalars as cold dark matter," Phys. Rev. D **50**, 3637 (1994) [hep-ph/0702143 [HEP-PH]].

[237] C. P. Burgess, M. Pospelov and T. ter Veldhuis, "The Minimal model of nonbaryonic dark matter: A Singlet scalar," Nucl. Phys. B **619**, 709 (2001) [hep-ph/0011335].

[238] R. M. Schabinger and J. D. Wells, "A Minimal spontaneously broken hidden sector and its impact on Higgs boson physics at the large hadron collider," Phys. Rev. D **72**, 093007 (2005) [hep-ph/0509209].

[239] B. Patt and F. Wilczek, "Higgs-field portal into hidden sectors," hep-ph/0605188.

[240] R. Barbieri, T. Gregoire and L. J. Hall, "Mirror world at the large hadron collider," hep-ph/0509242.

[241] M. H. G. Tytgat, "A light scalar WIMP through the Higgs portal?," PoS IDM **2010**, 126 (2011) [arXiv:1012.0576 [hep-ph]].

[242] C. Englert, T. Plehn, D. Zerwas and P. M. Zerwas, "Exploring the Higgs portal," Phys. Lett. B **703**, 298 (2011) [arXiv:1106.3097 [hep-ph]].

[243] M. Pospelov and A. Ritz, "Higgs decays to dark matter: beyond the minimal model," Phys. Rev. D **84**, 113001 (2011) [arXiv:1109.4872 [hep-ph]].

[244] X. G. He and J. Tandean, "Hidden Higgs Boson at the LHC and Light Dark Matter Searches," Phys. Rev. D **84**, 075018 (2011) [arXiv:1109.1277 [hep-ph]].

[245] P. J. Fox, R. Harnik, J. Kopp and Y. Tsai, "Missing Energy Signatures of Dark Matter at the LHC," Phys. Rev. D **85**, 056011 (2012) [arXiv:1109.4398 [hep-ph]].

[246] I. Low, P. Schwaller, G. Shaughnessy and C. E. M. Wagner, "The dark side of the Higgs boson," Phys. Rev. D **85**, 015009 (2012) [arXiv:1110.4405 [hep-ph]].

[247] C. Englert, T. Plehn, M. Rauch, D. Zerwas and P. M. Zerwas, "LHC: Standard Higgs and Hidden Higgs," Phys. Lett. B **707**, 512 (2012) [arXiv:1112.3007 [hep-ph]].

[248] A. Djouadi, O. Lebedev, Y. Mambrini and J. Quevillon, "Implications of LHC searches for Higgs–portal dark matter," Phys. Lett. B **709**, 65 (2012) [arXiv:1112.3299 [hep-ph]].

[249] B. Batell, S. Gori and L. T. Wang, "Exploring the Higgs Portal with 10/fb at the LHC," JHEP **1206**, 172 (2012) [arXiv:1112.5180 [hep-ph]].

[250] S. Baek, P. Ko and W. I. Park, "Invisible Higgs Decay Width vs. Dark Matter Direct Detection Cross Section in Higgs Portal Dark Matter Models," Phys. Rev. D **90**, no. 5, 055014 (2014) [arXiv:1405.3530 [hep-ph]].

[251] ALEPH Collaboration, EPJ C14 1; Delphi Collaboration, EPJ C16 371; L3 Collaboration, EPJ C16 1; OPAL Collaboration, EPJ C19 587; Particle Data Group: http://pdg.lbl.gov/2014/listings/rpp2014-list-z-boson.pdf

[252] D. Asner *et al.* [Heavy Flavor Averaging Group Collaboration], "Averages of b-hadron, c-hadron, and τ-lepton properties," arXiv:1010.1589 [hep-ex].

[253] Tevatron Electroweak Working Group [CDF and D0 Collaborations], "Combination of CDF and D0 results on the mass of the top quark using up to 9.7 fb^{-1} at the Tevatron," arXiv:1407.2682 [hep-ex].

[254] [ATLAS and CDF and CMS and D0 Collaborations], "First combination of Tevatron and LHC measurements of the top-quark mass," arXiv:1403.4427 [hep-ex].

[255] K. Kröninger, A. B. Meyer and P. Uwer, "Top-Quark Physics at the LHC," arXiv:1506.02800 [hep-ex].
Particle Data Group: http://pdg.lbl.gov/2014/reviews/rpp2014-rev-top-quark.pdf

[256] G. Aad *et al.* [ATLAS Collaboration], "Search for direct production of charginos, neutralinos and sleptons in final states with two leptons and missing transverse momentum in pp collisions at $\sqrt{s}$ = 8 TeV with the ATLAS detector," JHEP **1405**, 071 (2014) [arXiv:1403.5294 [hep-ex]].

[257] G. Aad *et al.* [ATLAS Collaboration], "Search for direct production of charginos and neutralinos in events with three leptons and missing transverse momentum in $\sqrt{s}$ = 8TeV pp collisions with the ATLAS detector," JHEP **1404**, 169 (2014) [arXiv:1402.7029 [hep-ex]].

[258] V. Khachatryan *et al.* [CMS Collaboration], "Searches for electroweak production of charginos, neutralinos, and sleptons decaying to leptons and W, Z, and Higgs bosons in pp collisions at 8 TeV," Eur. Phys. J. C **74**, no. 9, 3036 (2014) [arXiv:1405.7570 [hep-ex]].

[259] G. Aad *et al.* [ATLAS Collaboration], "Constraints on new phenomena via Higgs boson couplings and invisible decays with the ATLAS detector," JHEP **1**511, 206 (2015) [arXiv:1509.00672 [hep-ex]].

[260] V. Khachatryan *et al.* [CMS Collaboration], "Searches for invisible decays of the Higgs boson in pp collisions at sqrt(s) = 7, 8, and 13 TeV," JHEP **1**702, 135 (2017) [arXiv:1610.09218 [hep-ex]].

[261] G. Aad *et al.* [ATLAS Collaboration], "Search for squarks and gluinos with the ATLAS detector in final states with jets and missing transverse momentum using $\sqrt{s}$ = 8 TeV proton–proton collision data," JHEP **1409**, 176 (2014) [arXiv:1405.7875 [hep-ex]].

[262] T. Corbett, O. J. P. Eboli, D. Goncalves, J. Gonzalez-Fraile, T. Plehn and M. Rauch, "The Non-Linear Higgs Legacy of the LHC Run I," arXiv:1511.08188 [hep-ph].

[263] G. Aad *et al.* [ATLAS Collaboration], "Measurements of Higgs boson production and couplings in diboson final states with the ATLAS detector at the LHC," Phys. Lett. B **726**, 88 (2013) Erratum: [Phys. Lett. B **734**, 406 (2014)] [arXiv:1307.1427 [hep-ex]].

[264] S. Chatrchyan *et al.* [CMS Collaboration], "Observation of a new boson with mass near 125 GeV in pp collisions at $\sqrt{s}$ = 7 and 8 TeV," JHEP **1306**, 081 (2013) [arXiv:1303.4571 [hep-ex]].

[265] G. Belanger, B. Dumont, U. Ellwanger, J. F. Gunion and S. Kraml, "Global fit to Higgs signal strengths and couplings and implications for extended Higgs sectors," Phys. Rev. D **88**, 075008 (2013); [arXiv:1306.2941 [hep-ph]].

[266] P. P. Giardino, K. Kannike, I. Masina, M. Raidal and A. Strumia, "The universal Higgs fit," JHEP **1405**, 046 (2014); [arXiv:1303.3570 [hep-ph]].

[267] P. Bechtle, S. Heinemeyer, O. Stal, T. Stefaniak and G. Weiglein, "Probing the Standard Model with Higgs signal rates from the Tevatron, the LHC and a future ILC," JHEP **1411**, 039 (2014); [arXiv:1403.1582 [hep-ph]].

[268] K. Cheung, J. S. Lee and P. Y. Tseng, "Higgs precision analysis updates 2014," Phys. Rev. D **90**, 095009 (2014); [arXiv:1407.8236 [hep-ph]].

[269] J. B. Flament, "Higgs couplings and BSM physics: Run I Legacy constraints," [arXiv:1504.07919 [hep-ph]].

[270] B. Dumont, S. Fichet and G. von Gersdorff, "A Bayesian view of the Higgs sector with higher dimensional operators," JHEP **1307**, 065 (2013) [arXiv:1304.3369 [hep-ph]].

[271] S. Fichet and G. Moreau, "Anatomy of the Higgs fits: a first guide to statistical treatments of the theoretical uncertainties," Nucl. Phys. B **905**, 391 (2016); [arXiv:1509.00472 [hep-ph]].

[272] G. Buchalla, O. Cata, A. Celis and C. Krause, "Fitting Higgs Data with Nonlinear Effective Theory," Eur. Phys. J. C **76**, no. 5, 233 (2016) [arXiv:1511.00988 [hep-ph]].

[273] C. Englert, R. Kogler, H. Schulz and M. Spannowsky, "Higgs coupling measurements at the LHC," Eur. Phys. J. C **76**, no. 7, 393 (2016) [arXiv:1511.05170 [hep-ph]].

[274] L. Reina, J. de Blas, M. Ciuchini, E. Franco, D. Ghosh, S. Mishima, M. Pierini and L. Silvestrini, "Precision constraints on non-standard Higgs-boson couplings with HEPfit," PoS EPS-**HEP2015**, 187 (2015);

[275] S. Banerjee, S. Mukhopadhyay and B. Mukhopadhyaya, "Higher dimensional operators and the LHC Higgs data: The role of modified kinematics," Phys. Rev. D **89**, no. 5, 053010 (2014); [arXiv:1308.4860 [hep-ph]].

[276] L. Bian, J. Shu and Y. Zhang, "Prospects for Triple Gauge Coupling Measurements at Future Lepton Colliders and the 14 TeV LHC," JHEP **1509**, 206 (2015). [arXiv:1507.02238 [hep-ph]].

[277] J. Ellis, V. Sanz and T. You, "Complete Higgs Sector Constraints on Dimension-6 Operators," JHEP **1407**, 036 (2014) [arXiv:1404.3667 [hep-ph]].

[278] J. Ellis, V. Sanz and T. You, "The Effective Standard Model after LHC Run I," JHEP **1503**, 157 (2015) [arXiv:1410.7703 [hep-ph]].

[279] C. Englert, A. Freitas, M. M. Mühlleitner, T. Plehn, M. Rauch, M. Spira and K. Walz, "Precision Measurements of Higgs Couplings: Implications for New Physics Scales," J. Phys. G **41**, 113001 (2014) [arXiv:1403.7191 [hep-ph]].

[280] S. Weinberg, "Phenomenological Lagrangians," Physica A **96**, 327 (1979).

[281] H. Georgi, "Weak Interactions and Modern Particle Theory," Menlo Park, Usa: Benjamin/cummings (1984) 165p

[282] J. F. Donoghue, E. Golowich and B. R. Holstein, "Dynamics of the standard model," Camb. Monogr. Part. Phys. Nucl. Phys. Cosmol. **2**, 1 (1992) [Camb. Monogr. Part. Phys. Nucl. Phys. Cosmol. **35** (2014)].

[283] R. D. Peccei and H. R. Quinn, "CP Conservation in the Presence of Instantons," Phys. Rev. Lett. **38**, 1440 (1977).

[284] C. N. Leung, S. T. Love and S. Rao, "Low-Energy Manifestations of a New Interaction Scale: Operator Analysis," Z. Phys. C **31**, 433 (1986).

[285] W. Buchmuller and D. Wyler, "Effective Lagrangian Analysis of New Interactions and Flavor Conservation," Nucl. Phys. B **268**, 621 (1986).

[286] A. De Rujula, M. B. Gavela, P. Hernandez and E. Masso, "The Selfcouplings of vector bosons: Does LEP-1 obviate LEP-2?," Nucl. Phys. B **384**, 3 (1992).

[287] K. Hagiwara, R. Szalapski and D. Zeppenfeld, "Anomalous Higgs boson production and decay," Phys. Lett. B **318**, 155 (1993) [hep-ph/9308347].

[288] K. Hagiwara, S. Matsumoto and R. Szalapski, "Constraints on new physics in the electroweak bosonic sector from current data and future experiments," Phys. Lett. B **357**, 411 (1995) [hep-ph/9505322].

[289] M. C. Gonzalez-Garcia, "Anomalous Higgs couplings," Int. J. Mod. Phys. A **14**, 3121 (1999) [hep-ph/9902321].

[290] G. Passarino, "NLO Inspired Effective Lagrangians for Higgs Physics," Nucl. Phys. B **868**, 416 (2013). [arXiv:1209.5538 [hep-ph]].

[291] For a pedagogical introduction see e. g. W. Kilian, "Electroweak symmetry breaking: The bottom-up approach," Springer Tracts Mod. Phys. **198**, 1 (2003).

[292] F. Bonnet, M. B. Gavela, T. Ota and W. Winter, "Anomalous Higgs couplings at the LHC, and their theoretical interpretation," Phys. Rev. D **85**, 035016 (2012) [arXiv:1105.5140 [hep-ph]].

[293] F. Bonnet, T. Ota, M. Rauch and W. Winter, "Interpretation of precision tests in the Higgs sector in terms of physics beyond the Standard Model," Phys. Rev. D **86**, 093014 (2012) [arXiv:1207.4599 [hep-ph]].

[294] K. Hagiwara, S. Ishihara, R. Szalapski and D. Zeppenfeld, "Low-energy effects of new interactions in the electroweak boson sector," Phys. Rev. D **48**, 2182 (1993).

[295] K. Hagiwara, T. Hatsukano, S. Ishihara and R. Szalapski, "Probing nonstandard bosonic interactions via W boson pair production at lepton colliders," Nucl. Phys. B **496**, 66 (1997) [hep-ph/9612268].

[296] B. Grzadkowski, M. Iskrzynski, M. Misiak, and J. Rosiek, "Dimension-Six Terms in the Standard Model Lagrangian," JHEP **1010**, 085 (2010). [arXiv:1008.4884 [hep-ph]].

[297] T. Corbett, O. J. P. Éboli, J. Gonzalez-Fraile and M. C. Gonzalez-Garcia, "Determining Triple Gauge Boson Couplings from Higgs Data," Phys. Rev. Lett. **111**, 011801 (2013) [arXiv:1304.1151 [hep-ph]].

[298] T. Corbett, O. J. P. Eboli, J. Gonzalez-Fraile and M. C. Gonzalez-Garcia, "Constraining anomalous Higgs interactions," Phys. Rev. D **86**, 075013 (2012) [arXiv:1207.1344 [hep-ph]].

[299] T. Corbett, O. J. P. Eboli, J. Gonzalez-Fraile and M. C. Gonzalez-Garcia, "Robust Determination of the Higgs Couplings: Power to the Data," Phys. Rev. D **87**, 015022 (2013) [arXiv:1211.4580 [hep-ph]].

[300] I. Brivio, T. Corbett, O. J. P. Eboli, M. B. Gavela, J. Gonzalez-Fraile, M. C. Gonzalez-Garcia, L. Merlo and S. Rigolin, "Disentangling a dynamical Higgs," JHEP **1403**, 024 (2014). [arXiv:1311.1823 [hep-ph]]

[301] E. Massó and V. Sanz, "Limits on anomalous couplings of the Higgs boson to electroweak gauge bosons from LEP and the LHC," Phys. Rev. D **87**, no. 3, 033001 (2013) [arXiv:1211.1320 [hep-ph]].

[302] A. Falkowski, M. Gonzalez-Alonso, A. Greljo and D. Marzocca, "Global constraints on anomalous triple gauge couplings in effective field theory approach," Phys. Rev. Lett. **116**, no. 1, 011801 (2016) [arXiv:1508.00581 [hep-ph]].

[303] G. Brooijmans *et al.*, "Les Houches 2013: Physics at TeV Colliders: New Physics Working Group Report," arXiv:1405.1617 [hep-ph].

[304] M. Trott, "On the consistent use of Constructed Observables," JHEP **1502**, 046 (2015); [arXiv:1409.7605 [hep-ph]].

[305] A. Falkowski and F. Riva, "Model-independent precision constraints on dimension-6 operators," JHEP **1502**, 039 (2015). [arXiv:1411.0669 [hep-ph]].

[306] K. Hagiwara, R. D. Peccei, D. Zeppenfeld and K. Hikasa, "Probing the Weak Boson Sector in e+ e- —¿ W+ W-," Nucl. Phys. B **282**, 253 (1987).

[307] R. Alonso, M. B. Gavela, L. Merlo, S. Rigolin and J. Yepes, "The Effective Chiral Lagrangian for a Light Dynamical "Higgs Particle"," Phys. Lett. B **722**, 330 (2013) Erratum: [Phys. Lett. B **726**, 926 (2013)]; [arXiv:1212.3305 [hep-ph]].

[308] G. Buchalla, O. Catà and C. Krause, "Complete Electroweak Chiral Lagrangian with a Light Higgs at NLO," Nucl. Phys. B **880**, 552 (2014); [arXiv:1307.5017 [hep-ph]].

[309] M. B. Gavela, J. Gonzalez-Fraile, M. C. Gonzalez-Garcia, L. Merlo, S. Rigolin and J. Yepes, "CP violation with a dynamical Higgs," JHEP **1410**, 44 (2014); [arXiv:1406.6367 [hep-ph]].

[310] I. Brivio, J. Gonzalez-Fraile, M. C. Gonzalez-Garcia and L. Merlo, "The complete HEFT Lagrangian after the LHC Run I," Eur. Phys. J. C **76**, no. 7, 416 (2016) [arXiv:1604.06801 [hep-ph]].

[311] S. Chatrchyan *et al.* [CMS Collaboration], "Measurement of the $W\gamma$ and $Z\gamma$ inclusive cross sections in pp collisions at $\sqrt{s} = 7$ TeV and limits on anomalous triple gauge boson couplings," Phys. Rev. D **89**, no. 9, 092005 (2014) [arXiv:1308.6832 [hep-ex]].

[312] G. Aad *et al.* [ATLAS Collaboration], "Measurement of total and differential W^+W^- production cross sections in proton-proton collisions at $\sqrt{s} = 8$ TeV with the ATLAS detector and limits on anomalous triple-gauge-boson couplings," JHEP **1609**, 029 (2016) [arXiv:1603.01702 [hep-ex]].

[313] V. Khachatryan *et al.* [CMS Collaboration], "Measurement of the W^+W^- cross section in pp collisions at $\sqrt{s} = 8$ TeV and limits on anomalous gauge couplings," Eur. Phys. J. C **76**, no. 7, 401 (2016) [arXiv:1507.03268 [hep-ex]].

[314] G. Aad *et al.* [ATLAS Collaboration], "Measurements of $W^{\pm}Z$ production cross sections in pp collisions at $\sqrt{s} = 8$ TeV with the ATLAS detector and limits on anomalous gauge boson self-couplings," Phys. Rev. D **93**, no. 9, 092004 (2016) [arXiv:1603.02151 [hep-ex]].

[315] CMS Collaboration [CMS Collaboration], "Measurement of WZ production rate," CMS-PAS-SMP-12-006, http://cms-results.web.cern.ch/cms-results/public-results/preliminary-results/SMP-12-006

[316] G. Aad *et al.* [ATLAS Collaboration], "Measurement of the $WW + WZ$ cross section and limits on anomalous triple gauge couplings using final states with one lepton, missing transverse momentum, and two jets with the ATLAS detector at $\sqrt{s} = 7$ TeV," JHEP **1501**, 049 (2015) [arXiv:1410.7238 [hep-ex]].

[317] S. Chatrchyan *et al.* [CMS Collaboration], "Measurement of the sum of WW and WZ production with W+dijet events in pp collisions at $\sqrt{s} = 7$ TeV," Eur. Phys. J. C **73**, no. 2, 2283 (2013). [arXiv:1210.7544 [hep-ex]].

[318] G. Aad *et al.* [ATLAS Collaboration], "Measurement of WZ production in proton-proton collisions at $\sqrt{s} = 7$ TeV with the ATLAS detector," Eur. Phys. J. C **72**, 2173 (2012). [arXiv:1208.1390 [hep-ex]].

[319] J. Alwall *et al.*, "The automated computation of tree-level and next-to-leading order differential cross sections, and their matching to parton shower simulations," JHEP **1407**, 079 (2014). [arXiv:1405.0301 [hep-ph]].

[320] T. Sjostrand, S. Mrenna and P. Z. Skands, "PYTHIA 6.4 Physics and Manual," JHEP **0605**, 026 (2006). [hep-ph/0603175].

[321] J. de Favereau *et al.* [DELPHES 3 Collaboration], JHEP **1402**, 057 (2014) [arXiv:1307.6346 [hep-ex]].

[322] T. Gehrmann, M. Grazzini, S. Kallweit, P. Maierhöfer, A. von Manteuffel, S. Pozzorini, D. Rathlev and L. Tancredi, "W^+W^- Production at Hadron Colliders in Next to Next to Leading Order QCD," Phys. Rev. Lett. **113**, no. 21, 212001 (2014); [arXiv:1408.5243 [hep-ph]];

[323] P. Meade, H. Ramani and M. Zeng, "Transverse momentum resummation effects in W^+W^- measurements," Phys. Rev. D **90**, no. 11, 114006 (2014); [arXiv:1407.4481 [hep-ph]];

[324] T. Binoth, M. Ciccolini, N. Kauer and M. Kramer, "Gluon-induced W-boson pair production at the LHC," JHEP **0612**, 046 (2006); [hep-ph/0611170];

[325] A. Bierweiler, T. Kasprzik, J. H. Kühn and S. Uccirati, "Electroweak corrections to W-boson pair production at the LHC," JHEP **1211**, 093 (2012); [arXiv:1208.3147 [hep-ph]];

[326] J. M. Campbell, R. K. Ellis and C. Williams, "Vector boson pair production at the LHC," JHEP **1107**, 018 (2011); [arXiv:1105.0020 [hep-ph]];

[327] M. Billoni, S. Dittmaier, B. Jäger and C. Speckner, "Next-to-leading order electroweak corrections to pp → W+W- → 4 leptons at the LHC in double-pole approximation," JHEP **1312**, 043 (2013). [arXiv:1310.1564 [hep-ph]].

[328] N. D. Christensen and C. Duhr, "FeynRules - Feynman rules made easy," Comput. Phys. Commun. **180**, 1614 (2009) [arXiv:0806.4194 [hep-ph]].

[329] T. Plehn and M. Rauch, "Higgs Couplings after the Discovery," Europhys. Lett. **100**, 11002 (2012) [arXiv:1207.6108 [hep-ph]].

[330] LEPEWWG/TGC/2002-02 http://lepewwg.web.cern.ch/LEPEWWG/lepww/tgc

[331] For related discussions in Higgs physics see e. g. J. Brehmer, A. Freitas, D. Lopez-Val and T. Plehn, "Pushing Higgs Effective Theory to its Limits," Phys. Rev. D **93**, no. 7, 075014 (2016) [arXiv:1510.03443 [hep-ph]].

[332] A. Biekötter, A. Knochel, M. Krämer, D. Liu and F. Riva, "Vices and virtues of Higgs effective field theories at large energy," Phys. Rev. D **91**, 055029 (2015); [arXiv:1406.7320 [hep-ph]].

[333] S. Dawson, I. M. Lewis and M. Zeng, "Usefulness of effective field theory for boosted Higgs production," Phys. Rev. D **91**, 074012 (2015); [arXiv:1501.04103 [hep-ph]].

[334] M. Gorbahn, J. M. No and V. Sanz, "Benchmarks for Higgs Effective Theory: Extended Higgs Sectors," JHEP **1510**, 036 (2015); [arXiv:1502.07352 [hep-ph]].

[335] A. Drozd, J. Ellis, J. Quevillon and T. You, "Comparing EFT and Exact One-Loop Analyses of Non-Degenerate Stops," JHEP **1506**, 028 (2015). [arXiv:1504.02409 [hep-ph]].

[336] For a comprehensive discussion on the validity of truncated effective Lagrangians see D. de Florian *et al.* [LHC Higgs Cross Section Working Group], "Handbook of LHC Higgs Cross Sections: 4. Deciphering the Nature of the Higgs Sector," arXiv:1610.07922 [hep-ph].

[337] A. Biekötter, J. Brehmer and T. Plehn, "Extending the limits of Higgs effective theory," Phys. Rev. D **94**, no. 5, 055032 (2016) [arXiv:1602.05202 [hep-ph]].

[338] R. Contino, A. Falkowski, F. Goertz, C. Grojean and F. Riva, "On the Validity of the Effective Field Theory Approach to SM Precision Tests," JHEP **1607**, 144 (2016) [arXiv:1604.06444 [hep-ph]].

[339] O. J. P. Eboli, J. Gonzalez-Fraile and M. C. Gonzalez-Garcia, "Scrutinizing the ZW+W- vertex at the Large Hadron Collider at 7 TeV," Phys. Lett. B **692**, 20 (2010). [arXiv:1006.3562 [hep-ph]].

[340] C. Bilchak, M. Kuroda and D. Schildknecht, "On $W^{\pm}$, Z_0, γ Selfinteractions: High-energy Behavior and Tree Unitarity Bounds," Nucl. Phys. B **299**, 7 (1988).

[341] G. J. Gounaris, J. Layssac, J. E. Paschalis and F. M. Renard, "Unitarity constraints for new physics induced by dim-6 operators," Z. Phys. C **66**, 619 (1995) [hep-ph/9409260].

[342] T. Corbett, O. J. P. Éboli and M. C. Gonzalez-Garcia, "Unitarity Constraints on Dimension-Six Operators," Phys. Rev. D **91**, no. 3, 035014 (2015) [arXiv:1411.5026 [hep-ph]].